Two-photon interference

Spatial aspects of two-photon entanglement, diffraction, and scattering

Wouter H. Peeters

Publisher: Casimir Research School, Lorentzweg 1, 2628 CJ Delft, The Netherlands.

ISBN: 97890 8593 089-1

Print: Gildeprint Drukkerijen - The Netherlands

Cover Design: Martijn van Leipsig

Cover: The background is an artist impression of two photons having both wave-like and particle-like properties. The figures are experimental two-photon interference patterns recorded in the far field of a double slit. The color scale corresponds to the rate of simultaneous photon detections by two single-photon detectors (black is zero). The horizontal and vertical axes correspond to the positions of the detectors measured along a transverse line perpendicular to the orientation of the slits.

Two-photon interference

Spatial aspects of two-photon entanglement, diffraction, and scattering

PROEFSCHRIFT

ter verkrijging van
de graad van doctor aan de Universiteit Leiden,
op gezag van rector magnificus prof. mr. P. F. van der Heijden,
volgens besluit van het College voor Promoties
te verdedigen op dinsdag 21 december 2010
klokke 13:45 uur

door

Wouter Herman Peeters

geboren te Berg en Terblijt, Nederland
op 27 februari 1980

Promotiecommissie:

Promotor:	Prof. dr. J. P. Woerdman	Universiteit Leiden
Copromotor	Dr. M. P. van Exter	Universiteit Leiden
Leden:	Prof. dr. C. W. J. Beenakker	Universiteit Leiden
	Dr. M. J. A. de Dood	Universiteit Leiden
	Prof. dr. A. Lagendijk	Universiteit van Amsterdam (UvA) en Universiteit Twente
	Prof. dr. G. Nienhuis	Universiteit Leiden
	Prof. dr. J. M. van Ruitenbeek	Universiteit Leiden
	Prof. dr. J. P. Torres	Universitat Politècnica de Catalunya (UPC)
	Dr. V. Zwiller	Technische Universiteit Delft

Paranimfen: ir. R. van Melle en drs. O. A. Tuinenburg

The research described in this thesis is part of the research programme of the Foundation for Fundamental Research on Matter (FOM), which is part of the Netherlands Organisation for Scientific Research (NWO).

The research has been carried out at the Quantum Optics and Quantum Information group, which is part of the Leiden Institute of Physics (LION) of the Faculty of Science of Leiden University.

Additionally, the academic environment has been supported by the Casimir Research School, which is supported by LION at Leiden University and the Kavli Institute of Nanoscience at Delft University of Technology.

An electronic version of this dissertation is available at the Leiden University Repository (https://openaccess.leidenuniv.nl).

Casimir PhD series, Delft-Leiden, 2010-29

Voor Ton, Wilma
en Janneke

Contents

1
Introduction

1.1 Interference in optics

1.1.1 Young's experiment: interference of waves

Around 1801, the British scientist Thomas Young demonstrated that light propagates like a wave. Light waves, in contrast to light rays, can form interference patterns. Young illuminated a mask with two parallel slits with monochromatic spatially coherent light and projected the transmitted light onto a screen. He observed a periodic intensity pattern of bright and dark lines, which he explained as an interference pattern. Figure 1.1 illustrates a simulation of a wave passing through a mask with two slits. The two waves that emerge from the slits expand in a circular manner such that they cross each others path. In the low-intensity regions, the phases of the two waves are opposite, and the waves interfere destructively at any instant of time. In the high-intensity regions, both waves interfere constructively yielding a larger detected intensity.

Later, in 1865, James Clerk Maxwell theoretically showed that the electric field and the magnetic field, together, can form a wave that propagates at exactly the speed of light [1]. Ever since, light is understood as a wave of the electromagnetic field. Classically, the state of the electromagnetic field is determined by the electric field $\mathbf{E}(\mathbf{r}, t)$ and the magnetic field $\mathbf{B}(\mathbf{r}, t)$. The time evolution of these fields is described by Maxwell's equations. [2].

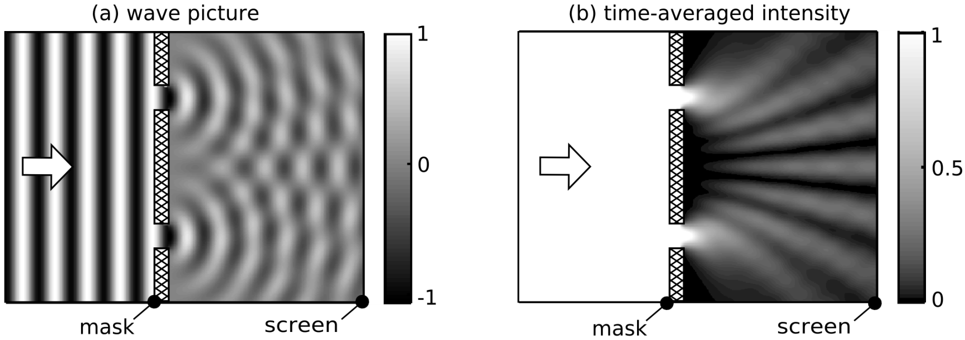

Figure 1.1: (a) Simulation of a wave propagating through a mask with two slits. The grey scale represents the wave displacement at some instant of time. (b) An interference pattern is formed in the time-averaged intensity profile behind the mask. Around 1801, Thomas Young demonstrated that light produces such intensity pattern. He visualized this interference pattern by projecting the transmitted light onto a screen.

1.1.2 One-photon and two-photon interference

The quantum theory of light describes the quantum state $|\Psi\rangle$ of the electromagnetic field [3,4]. Formally, this theory is obtained by applying a procedure called canonical quantization to the classical theory of the electromagnetic field. The foundation of multiphoton interference within quantum optics was laid by Glauber in 1963 in his influential work on quantum optical coherence [5]. The quantum theory replicates the occurrence of the classical interference patterns of the intensity similar to the one shown in Fig. 1.1(b). Additionally, Glauber's analysis makes clear that quantum interference can occur in n-fold intensity correlations between n separate detectors. This type of optical interference is now referred to as n-photon interference.

Young's classical interference pattern in Fig. 1.1 is a one-photon interference phenomenon. One-photon interference refers to a structure in the photon detection rate in a single detector. The photon detection rate is [5]

$$R^{(1)}(\mathbf{r}, t) \propto \langle \Psi | \hat{E}^{-}(\mathbf{r}, t) \hat{E}^{+}(\mathbf{r}, t) | \Psi \rangle, \tag{1.1}$$

where $\hat{E}^{\pm}(\mathbf{r}, t)$ are the positive and negative frequency electric-field operators at position $\mathbf{r}$ and time t. A one-photon interference pattern can in principle be formed by a single photon only. So if one would perform Young's experiment with a single photon, the probability of where the photon can be absorbed corresponds to the intensity pattern obtained from the classical wave theory [see Fig.1.1(b)].

Two-photon interference refers to a structure in the coincidence rate between two detectors. Glauber argued that this coincidence rate is [5]

$$R^{(2)}(\mathbf{r}_1, t_1; \mathbf{r}_2, t_2) \propto \langle\Psi|\hat{E}^-(\mathbf{r}_1, t_1)\hat{E}^-(\mathbf{r}_2, t_2)\hat{E}^+(\mathbf{r}_2, t_2)\hat{E}^+(\mathbf{r}_1, t_1)|\Psi\rangle, \tag{1.2}$$

where $\mathbf{r}_{1,2}$ and $t_{1,2}$ are space and time coordinates of the two detectors. It may not be obvious from Eq. (1.2) how two-photon interference can occur. Let us therefore construct the two-photon state*

$$|\Psi\rangle = \frac{1}{\sqrt{2}}\int d\mathbf{k}_1 d\mathbf{k}_2\ \phi^{(2)}(\mathbf{k}_1, \mathbf{k}_2)\hat{a}^\dagger(\mathbf{k}_1)\hat{a}^\dagger(\mathbf{k}_2)|\text{vac}\rangle, \tag{1.3}$$

where $\phi^{(2)}(\mathbf{k}_1, \mathbf{k}_2) = \phi^{(2)}(\mathbf{k}_2, \mathbf{k}_1)$ without loss of generality, $|\text{vac}\rangle$ is the continuous-mode vacuum, and $\hat{a}^\dagger(\mathbf{k})$ is the continuous-mode photon creation operator with momentum $\mathbf{k}$. For our interest in simplicity, we have restricted ourselves to one polarization only. Let us also specialize to paraxial light where $\phi^{(2)}(\mathbf{k}_1, \mathbf{k}_2)$ is nonzero only for $\mathbf{k}$ vectors that are oriented paraxially. By combining Eqs. (1.2) and (1.3), we find the two-photon interference pattern†

$$\begin{aligned} R^{(2)}(\mathbf{r}_1, t_1; \mathbf{r}_2, t_2) \quad \propto \quad & \Bigg| \int d\mathbf{k}_1 d\mathbf{k}_2\ \phi^{(2)}(\mathbf{k}_1, \mathbf{k}_2) \exp\left(i\mathbf{k}_1 \cdot \mathbf{r}_1 - i|\mathbf{k}_1|ct_1\right) \\ & \times \exp\left(i\mathbf{k}_2 \cdot \mathbf{r}_2 - i|\mathbf{k}_2|ct_2\right) \Bigg|^2, \end{aligned} \tag{1.4}$$

where c is the speed of light. The absolute square operation directly reveals the interference mechanism behind two-photon interference. The expression between $|..|^2$ is the two-photon wave packet, which is a complex (rotating) amplitude as a function of two coordinates. Each coordinate is propagated according to the scalar wave equation of light.

Two-photon interference is especially interesting if the two photons in Eq. (1.3) are entangled. In the entangled case, the two-photon amplitude does not factorize in two functions‡, i.e.,

$$\phi^{(2)}(\mathbf{k}_1, \mathbf{k}_2) \neq f(\mathbf{k}_1)f(\mathbf{k}_2).$$

* We use the continuous-mode formalism with usual commutation relations and field operators given by Eqs. (10.10-1)-(10.10-4) in Ref. [3]. Normalization then corresponds to $\int d\mathbf{k}_1 d\mathbf{k}_2 |\phi^{(2)}(\mathbf{k}_1, \mathbf{k}_2)|^2 = 1$, where we have imposed $\phi^{(2)}(\mathbf{k}_1, \mathbf{k}_2) = \phi^{(2)}(\mathbf{k}_2, \mathbf{k}_1)$ without loss of generality since any asymmetry drops out of Eq. (1.3).

† We adjusted the electric-field operator in Eq. (1.2) to a similar operator related to the square root of the photon density (the continuous-mode version of equation (12.3-1) in Ref. [3]). The expression for this adjusted field operator (in single-polarization form) is $\hat{V}^+(\mathbf{r}, t) = \sqrt{(2\pi)^{-3}} \int d\mathbf{k}\ \hat{a}(\mathbf{k}) \exp[i\mathbf{k} \cdot \mathbf{r} - i|\mathbf{k}|ct]$.

‡ It is debatable whether inseparability also implies entanglement. For example: is it correct to call $\phi^{(2)}(\mathbf{k}_1, \mathbf{k}_2) = f(\mathbf{k}_1)g(\mathbf{k}_2) + f(\mathbf{k}_2)g(\mathbf{k}_1)$ entangled? We will refer to this two-mode form of inseparability as entanglement between indistinguishable photons (see chapter 4).

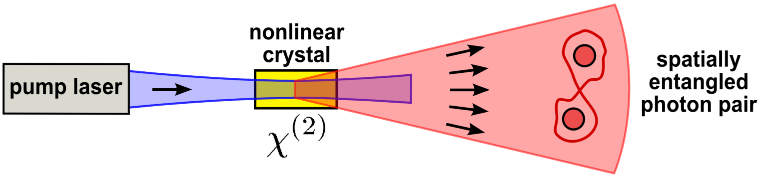

Figure 1.2: Experimental geometry for the operation of spontaneous parametric down-conversion. The down-converted light is spatially multimode (indicated by the arrows). Each down-converted photon pair is spatially entangled due to conservation of transverse momentum in the down-conversion process.

If this function would factorize, the two-photon interference pattern would become a trivial multiplication of the one-photon interference patterns, i.e.,

$$R^{(2)}(\mathbf{r}_1, t_1; \mathbf{r}_2, t_2) \propto R^{(1)}(\mathbf{r}_1, t_1)R^{(1)}(\mathbf{r}_2, t_2) \qquad [\text{if } \phi^{(2)}(\mathbf{k}_1, \mathbf{k}_2) \text{ factorizes}].$$

If the two-photon amplitude does not factorize, the one-photon interference pattern generally gets washed out, but, at the same time, the two-photon interference pattern retains its high visibility. Two-photon interference occurs most prominently in a two-photon state. The presence of a three-photon component (or more photons) will lower the visibility of the two-photon interference pattern if $\phi^{(2)}(\mathbf{k}_1, \mathbf{k}_2)$ is not factorizable. Therefore, one requires two-photon states to study interesting two-photon interference phenomena with high visibility.

1.1.3 Spontaneous parametric down-conversion: a source of pairs of entangled photons

Nowadays, two-photon interference experiments are commonly performed with photon pairs produced by the nonlinear $\chi^{(2)}$ process of spontaneous parametric down-conversion (SPDC). The process is operated by directing a coherent pump laser through a nonlinear crystal (see Fig. 1.2). SPDC refers to the occasional spontaneous splitting of a pump photon into two photons of lower energy (see Sec. 1.3 for details). These photon pairs can be observed as simultaneous clicks by two single photon detectors, as was first observed in 1970 [6]. Most interestingly, the photons within a pair are spatially entangled resulting from the conservation of transverse momentum in the down-conversion process. Loosely speaking, each photon is incoherently emitted in many spatial modes, but, at the same time, the pair as a whole is pure and has the well defined transverse momentum distribution of the pump beam. Section 1.3 describes how the down-converted stream of photon pairs can be identified with a two-photon wave packet similar to Eq. (1.3). The photon pairs produced by SPDC are thus excellent candidates for the research on two-photon

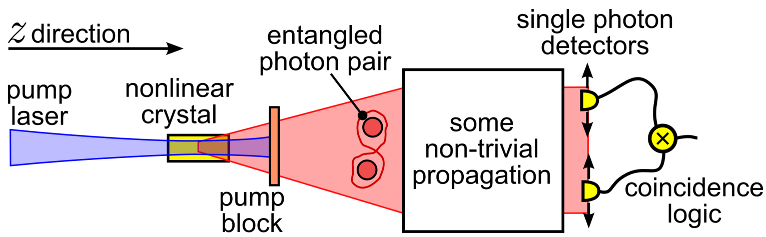

Figure 1.3: Generic scheme of the two-photon interference experiments discussed in this thesis. Two-photon interference phenomena are experimentally observed via the coincidence count rate in the plane of the detectors.

interference. Two-photon interference was first observed in 1987 by Ghosh, Hong, Ou, and Mandel [7, 8].

1.2 Research topics in this theses

1.2.1 Two-photon interference: three themes

The research in this thesis addresses spatial aspects of two-photon interference. The work is mainly experimental although our experiments are supported by theoretical models. The research can be divided into three research themes: We address (1) orbital angular momentum entanglement, (2) two-photon diffraction from a double slit, and (3) two-photon scattering of a random medium.

Despite their diversity, all themes are strongly related to one another. This is because two-photon interference and spatial entanglement play dominant roles in all themes. A generic scheme of all interference experiments is displayed in Fig. 1.3. Pairs of spatially entangled photons are emitted by the SPDC source and propagate through the experimental setup before being detected by two single-photon detectors. The propagation part is different for each experiment depending on the addressed research theme. Figure 1.4 illustrates the three setups that correspond to the three research themes. These research themes are discussed below in Secs. 1.2.2-1.2.4.

1.2.2 Theme 1: Orbital angular momentum entanglement

The spatial entanglement in the down-converted photon pair is of a high-dimensional form [9, 10]. This aspect is attracting a lot of attention because of its potential applicability in the field of quantum information processing [11–14]. The best studied basis of the spatial entanglement involves the orbital angular momentum (OAM) eigenstates [15–19]. If one photon is detected with OAM $+\hbar l$ then the other photon must collapse into a spatial profile with $-\hbar l$. This is because the pump beam is just a Gaussian $l = 0$ beam, and OAM is conserved in the down-conversion process. The quantum state of the photon pair can thus be tentatively written as*

$$|\Psi\rangle \sim \sum_{l=-\infty}^{\infty} \sqrt{P_l}\big| + l\hbar\big\rangle_1 \otimes \big| - l\hbar\big\rangle_2 \qquad \text{[omitting radial properties]},$$

where the probabilities $P_l = P_{-l}$ correspond to the distribution over the orbital angular momentum spectrum.

The distribution of the P_l coefficients can, in principle, be determined from the incoherent OAM distribution of just one of the photons [20, 21]. Such a measurement does, however, not depend on whether the photons are really entangled or not. The photons could equally well be a pair of independent incoherent photons with some OAM spectrum. In the literature, it was argued that the OAM distribution could also be determined via two-photon interference involving *both* entangled photons [22]. The experimental technique for this experiment is illustrated in Fig. 1.4 (theme 1). The orbital-angular momentum spectrum is contained in the visibility of the multimode Hong-Ou-Mandel dip as a function of the rotation angle of the image rotator [22]. In this thesis, we have used this challenging technique to determine the OAM distribution of the entangled photons. We also consider several special cases and provide a more detailed theoretical analysis supporting the experiment.

1.2.3 Theme 2: Two-photon diffraction from a double slit

Starting from 1994, a lot of experiments have addressed two-photon diffraction from a double-slit [23–35]. So why would one still want to study this topic? The reason is that the diversity of possible two-photon interference patterns behind a double slit has, we believe, not been widely appreciated. In fact, most of the possible forms of spatial entanglement behind the double slit have remained unexplored so far.

The most general two-photon state behind the double-slit (under symmetric two-photon illumination) can be written as

$$|\Psi\rangle = \cos(\alpha/2)\left(\frac{|\uparrow\downarrow\rangle + |\downarrow\uparrow\rangle}{\sqrt{2}}\right) + e^{i\varphi}\sin(\alpha/2)\left(\frac{|\uparrow\uparrow\rangle + |\downarrow\downarrow\rangle}{\sqrt{2}}\right), \qquad (1.5)$$

where $|\uparrow\rangle$ and $|\downarrow\rangle$ represent transmissions through the top and bottom slit, and parameters α and φ determine the quantum state. This state can be recognized as a superposition of two maximally entangled Bell states. The first Bell state corresponds to photons going through opposite slits; the second term corresponds to

* The full Schmidt decomposition also involves the radial properties of the mode profiles (see Ref. [9] and chapter 2): $|\Psi\rangle = \sum\limits_{l=-\infty}^{\infty}\sum\limits_{p=0}^{\infty} \sqrt{P_{l,p}}\; |l\hbar, p\rangle_1 \otimes |-l\hbar, p\rangle_2$.

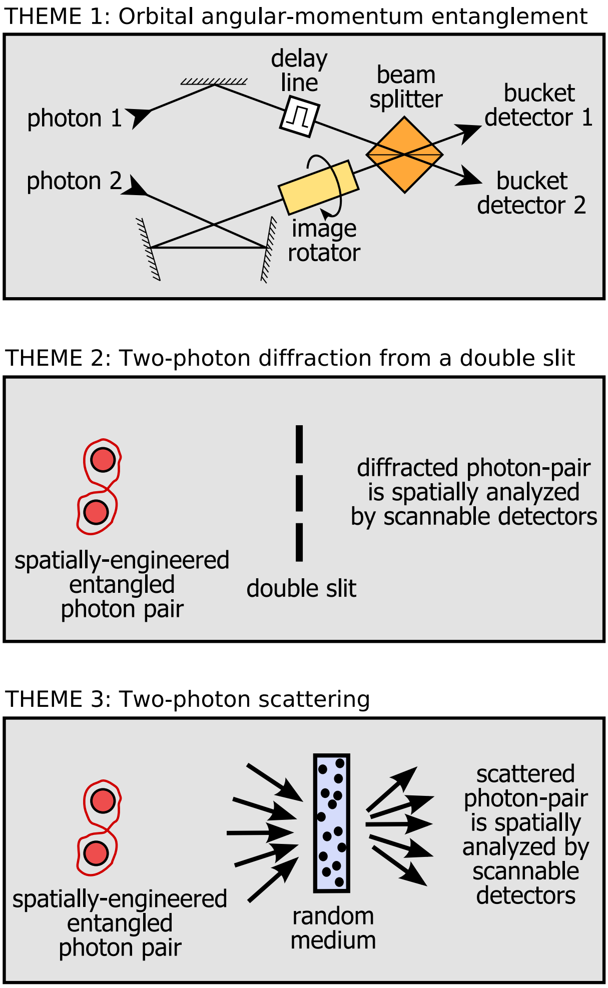

Figure 1.4: Three themes addressing two-photon interference in this thesis. The illustrations represent the propagation-boxes that can be inserted into Fig. 1.3.

photons choosing the same slit. So far, no attention has been paid to the experimental tuning of the phase φ. However, this phase is extremely important for the degree and type of entanglement. One could, for example, consider the maximally entangled state at $\alpha = \varphi = \frac{1}{2}\pi$. In this form of entanglement, the path of photon 1 is quantum correlated with the state $|\uparrow\rangle \pm i|\downarrow\rangle$ of photon 2, while path-path correlation is absent.

In comparison to other experiments on the two-photon double slit, our research is novel in three different ways. First, we demonstrate how to engineer the spatial entanglement with full control over state parameters α and φ. Secondly, our analysis provides a deeper understanding of the spatial structure in the entanglement between down-converted photons. We address, for the first time, phase-sensitive aspects of the two-photon field in the near-field of the generating crystal. Finally, we measure entire two-photon diffraction patterns in the far-field of the double slit with unprecedented quality. Our experiments reveal, in a very pure manner (namely: double-slit diffraction), the large diversity of two-photon interference patterns.

1.2.4 Theme 3: Two-photon scattering

This theme is the most advanced. Until now, the propagation of entangled photon pairs through a random medium has never been investigated experimentally. Only recently, a few theoretical papers have appeared [36–38]. Why would one want to study such a topic? The reason is simple. One-photon interference effects in random media are widely studied and have proven to be extremely interesting and diverse [39, 40]. Interesting phenomena within one-photon scattering are speckle [41], enhanced backscattering [42, 43], universal conductance fluctuations [44], and Anderson localization of light [43, 45–47]. Can we discover similar phenomena for two-photon interference in the case of two-photon scattering?

There are thus enough interesting questions to ask about two-photon scattering. How does two-photon speckle look like? How does scattering affect the entanglement between the photons? In which way does the scattered two-photon state contain information about the scattering medium? Do there exist two-photon interference phenomena that survive averaging over different realizations of disorder? In this thesis, all the above questions are, to a large extent, answered and experimentally demonstrated.

1.3 Quantum description of SPDC light

1.3.1 Motivation

In the previous section, we presented an overview of the topics that are investigated in this thesis. Despite the diversity, all experiments address the same observable: the time-averaged coincidence count rate in continuous-wave (cw) pumped, low-gain* SPDC light. For each experiment, we have made a theoretical model providing a solid understanding of the experimental results. All models are based on a quantum description of SPDC light. More specifically, the models are based on a single concept called the two-photon field. As the two-photon field plays a central role in this thesis, we have devoted Secs. 1.3.2-1.3.5 to a discussion of the theoretical foundation of this concept.

1.3.2 Two approaches to describe SPDC light

The description of SPDC light requires a quantum-mechanical treatment of the SPDC process†. There is a substantial amount of literature on the theory of SPDC [3,4,49,51–65]. The treatments can be divided into two categories depending on the approach.

The first approach uses the quantized version of the input-output relations of a parametric amplifier [3, 4, 49, 60–62, 64]. The light in the output channels is described as a noisy signals exhibiting quantum Gaussian noise [49,58]. This approach is suitable for both the low-gain and high-gain regime of SPDC and has gained popularity in the last decade [50, 60, 62, 64, 66]. Most papers just analyse a two-channel parametric amplifier (signal and idler), although spatially multimode SPDC has also been treated in this way [60, 61, 67].

The second approach is based on a first-order perturbative analysis of the time-evolution operator [3, 51, 53–55, 57, 59, 63, 65, 68]. This approach only works in the low-gain regime since a first-order perturbation analysis yields at most a single photon pair. All spatial and temporal correlations between the photons are contained in the resulting quantum state. As all experiments in this thesis are performed in

* Parametric gain corresponds to the strength at which the signal and idler fields are amplified due to parametric interaction with the strong pump beam. Low gain means that a generated photon pair has low probability ($\ll 1$) to stimulate the generation of another pair (thus creating four photons) during transmission through the crystal.

† Other $\chi^{(2)}$ processes like second harmonic generation and sum/difference frequency generation can be understood classically. These processes can be described as radiation emitted by a classically oscillating polarization of the nonlinear medium. This is not possible for the SPDC process. Besides, high-visibility two-photon interference phenomena can not be understood classically either. One can, in theory at least, construct classical signals that exhibit some form of two-photon interference with a strongly reduced visibility. The maximum visibility that can be constructed classically is a rather complicated issue [48–50].

the low-gain regime, we use a description of the SPDC light that is based on the perturbative approach (see Sec. 1.3.3).

1.3.3 Two-photon field

Based on the perturbative approach, the concept of the two-photon field was put forward in Refs. [54, 56] by Rubin, Klyshko, Shih, and Sergienko. In the first-order perturbation method, the quantum state of the generated SPDC light is calculated as [3, 53–55, 59, 65, 68]

$$|\Psi(\tau)\rangle \approx |\text{vac}\rangle - \frac{i}{\hbar}\int\limits_0^\tau dt\ \hat{H}_I(t)|\text{vac},\rangle \tag{1.6}$$

where τ is the interaction time, and $\hat{H}_I(t)$ is the interaction Hamiltonian of the $\chi^{(2)}$ nonlinear process driven by a classical, paraxial, and monochromatic pump beam $E(\mathbf{r}, t)$ [3, 53, 59]. The interaction Hamiltonian contains two photon creation operators and depends linearly on the driving field of the pump beam, the interaction volume, and the second-order nonlinear susceptibility $\chi^{(2)}$ of the crystal.

The second term in Eq. (1.6) is a two-photon component. The norm of this component grows linearly with the interaction time*. Intuitively, state $|\Psi(\tau)\rangle$ is only experimentally meaningful if the norm of the two-photon component stays way below unity even for interaction times τ much greater than the transmission time through the crystal (which implies the low-gain regime). Then, the interaction time for which this norm equals unity corresponds to the average time between successive down-conversions†. The quantum state $|\Psi(\tau)\rangle$ contains all spatial and temporal correlations between the down-converted photons and is thus effective in describing multimode two-photon interference experiments [51, 68, 69].

The normalization of $|\Psi(\tau)\rangle$ breaks down dramatically for large interaction times [3]. Nonetheless, this normalization issue is often ignored in the literature; in many papers, the interaction time is simply taken to infinite yielding [54,57,59,63,68]

$$|\Psi_\infty\rangle \equiv |\text{vac}\rangle - \frac{i}{\hbar}\int\limits_{-\infty}^{\infty} dt\ \hat{H}_I(t)|\text{vac}\rangle. \tag{1.7}$$

The normalizability of $|\Psi_\infty\rangle$ breaks down on account of the first-order perturbation method, the infinite interaction time, and the infinite duration of the driving cw pump beam (thus $\langle\Psi_\infty|\Psi_\infty\rangle = \infty$). Quite remarkably, this normalization issue is hardly ever discussed; it is, to the best of our knowledge, only addressed by

* See equations (22.4-23) to (22.4-25) in Ref. [3].
† Compare equations (22.4-25) and (22.4-31) in Ref. [3].

Shapiro *et al.* in Refs. [50, 62]. Mathematically, the state $|\Psi_\infty\rangle$ contains only two photons. In the laboratory, however, a typical SPDC source produces millions of photon pairs per second.

The two-photon field is defined as [54, 56]

$$A(\mathbf{x}_1, t_1, \mathbf{x}_2, t_2; z) \equiv \langle \mathrm{vac}|\hat{E}^+(\mathbf{x}_2, t_2; z)\hat{E}^+(\mathbf{x}_1, t_1; z)|\Psi_\infty\rangle, \tag{1.8}$$

where $\hat{E}^+(\mathbf{x}, t; z)$ is the positive frequency electric-field operator at transverse position $\mathbf{x}$, time t, and longitudinal position z. In the paraxial and narrow-band regime ($\Delta\omega \ll \omega$), the electric field operators can be expressed* in units of $\sqrt{\mathrm{photons/m^2s}}$. The two-photon field then acquires units $(\mathrm{m^2s})^{-1}$. The divergence of $|\Psi_\infty\rangle$ is also present in the two-photon field in a sense that it is not square integrable over all positions $\mathbf{x}_{1,2}$ and times $t_{1,2}$. The reason is that the two-photon field stretches out over an infinite amount of time. Nevertheless, its square amplitude in the time domain is finite and relates to the photon flux [54, 55, 62]. The two-photon field should thus be regarded as an unnormalizable two-photon wave packet† for which its amplitude in the time domain is related to the photon flux.

Based on Refs. [54, 56], the time-averaged coincidence count rate between two detectors at transverse positions $\mathbf{x}_1$ and $\mathbf{x}_2$ becomes

$$R_{\mathrm{cc}}(\mathbf{x}_1, \mathbf{x}_2; z) \propto$$
$$\left(\frac{1}{2}\times\right) \int\limits_{A_1} d^2\mathbf{x}_1' \int\limits_{A_2} d^2\mathbf{x}_2' \int\limits_{-\frac{1}{2}\tau_g}^{+\frac{1}{2}\tau_g} dt' \left| A(\mathbf{x}_1 + \mathbf{x}_1', t, \mathbf{x}_2 + \mathbf{x}_2', t + t'; z) \right|^2, \tag{1.9}$$

where $A_{1,2}$ are the transverse integration areas of the two detectors and τ_g is the gating time window of the coincidence logic. In typical experiments, the gate time τ_g is much larger than the spread in arrival times of the photons. Therefore, the integral over dt' can be taken over an infinite interval without changing the outcome of the integral. The factor $\frac{1}{2}$ between parentheses applies to type-I SPDC and is absent in type-II SPDC. This is because in type-I SPDC, the electric field operators in Eq. (1.8) have the same polarization and sense *both* photons in the two-photon state. In type-II SPDC, the electric field operators in Eq. (1.8) are assumed to have orthogonal polarizations and individually address only *one* of the photons, which are now distinguishable instead of indistinguishable. The square absolute value operation in Eq. (1.9) directly reveals the two-photon interference mechanism.

---

* The expression for the electric-field operator in units of square-root photon flux is $\hat{E}^+(\mathbf{r}, t) = \sqrt{c/(2\pi)^3} \int d\mathbf{k}\ \hat{a}(\mathbf{k}) \exp[i\mathbf{k}\cdot\mathbf{r} - i|\mathbf{k}|ct]$.

† For type-I SPDC, the identification with the symmetrized paraxial two-photon amplitude $\phi^{(2)}(\mathbf{k}_1, \mathbf{k}_2)$ in Eq. (1.3) becomes:
$A(\mathbf{r}_1, t_1, \mathbf{r}_2, t_2) = \frac{c\sqrt{2}}{(2\pi)^3} \int d\mathbf{k}_1 d\mathbf{k}_2\ \phi^{(2)}(\mathbf{k}_1, \mathbf{k}_2) \exp\left[i\mathbf{k}_1\cdot\mathbf{r}_1 + i\mathbf{k}_2\cdot\mathbf{r}_2 - i|\mathbf{k}_1|ct_1 - i|\mathbf{k}_2|ct_2\right]$.

Spatial propagation of the two-photon field from $z = 0$ to $z = z_d$ is described by applying the Maxwell electric-field propagators to each of the electric-field operators in Eq. (1.8). Naturally, spatial propagation is written down after a temporal Fourier transform, i.e,

$$\begin{aligned} A(\mathbf{x}_1, \omega_1, \mathbf{x}_2, \omega_2; z_d) \quad &= \quad \int d^2\mathbf{x}_1' d^2\mathbf{x}_2' \; h(\mathbf{x}_1, z_d, \mathbf{x}_1', 0; \omega_1) h(\mathbf{x}_2, z_d, \mathbf{x}_2', 0; \omega_2) \\ &\qquad \times A(\mathbf{x}_1', \omega_1, \mathbf{x}_2', \omega_2; 0), \end{aligned} \tag{1.10}$$

where $h(\mathbf{x}_f, z_f, \mathbf{x}_i, z_i; \omega)$ is the electric field propagator for any forward-propagating frequency-conserving optical system (see for example Ref. [70]). In principle, with the tools presented in this section, one can describe any low-gain two-photon interference experiment in the form of Fig. 1.3.

The absence of an equality sign in Eq. (1.9) is rather unfortunate. Although Rubin *et al.* [54,56] actually use an equality sign there, they state that their equation "defines" rather than calculates the coincidence count rate [54]. From our point of view, an analysis of the relationship between the photon flux and the unnormalizable two-photon state $|\Psi_\infty\rangle$ is not clearly present in the literature*. We conjecture, however, that the proportionality sign can be replaced by an equality sign (assuming high detection efficiency). Our argument is that if one would plug in a *normalized* paraxial two-photon state in Eq. (1.8), one would precisely get a single coincidence count when integrating $\left(\frac{1}{2}\times\right) |A(\mathbf{x}_1, t_1, \mathbf{x}_2, t_2; z)|^2$ over coordinates $\mathbf{x}_{1,2}$ and $t_{1,2}$. The norm of $|\Psi(\tau)\rangle$ in Eq. (1.6) can be interpreted as the expected number of photon down-conversions and grows linearly with interaction time τ. Therefore, it seems reasonable to assume that the proportionality sign in Eq. (1.9) can be replaced by an equality sign.

1.3.4 Expression for the two-photon field

Based on the treatments in Refs. [51, 69], and assuming the crystal to be infinitely wide in both transverse directions, the Fourier-transformed two-photon field of Eq. (1.8) is

$$\begin{aligned} A(\mathbf{q}_1, \omega_1, \mathbf{q}_2, \omega_2; 0) \quad &\propto \quad \delta[\omega_p - (\omega_1 + \omega_2)] E_p(\mathbf{q}_1 + \mathbf{q}_2; z = 0) \\ &\qquad \times \mathrm{sinc}\left[\frac{L}{2}\Delta k_z(\mathbf{q}_1, \omega_1, \mathbf{q}_2, \omega_2)\right], \end{aligned} \tag{1.11}$$

where $\delta(\omega)$ is the Dirac-delta function, $\mathrm{sinc}(x) \equiv \sin(x)/x$, $\mathbf{q}_{1,2}$ are transverse momenta of the two-photon field, ω_p is the angular frequency of the pump beam, L is the crystal length, and $E_p(\mathbf{q}; z = 0)$ is the complex amplitude of the cw pump

* Wong *et al.* [62] get rather close, although, eventually, a quantitative comparison between $|\Psi_\infty\rangle$ and their quantum Gaussian noise description is absent.

beam in momentum representation (in the crystal-center plane). The function

$$\Delta k_z(\mathbf{q}_1, \omega_1, \mathbf{q}_2, \omega_2) \equiv k_z(\mathbf{q}_1 + \mathbf{q}_2, \omega_p) - k_z(\mathbf{q}_1, \omega_1) - k_z(\mathbf{q}_2, \omega_2), \tag{1.12}$$

is the wave vector mismatch along the z direction of the crystal. Here, $k_z(\mathbf{q}, \omega)$ is the z component of the wave vector of a plane wave inside the crystal with transverse momentum $\mathbf{q}$ and angular frequency ω. The proportionality in Eq. (1.11) contains a linear dependence on the effective nonlinearity and the length of the crystal. The two-photon field in Eq. (1.11) contains all you need to know to describe spatial and temporal effects in two-photon interference experiments. It is also very general as it applies to all cw-pumped, low-gain SPDC processes in any kind of phase-matching geometry: type-I (same polarization), type-II (different polarizations), and quasi phase matching*.

Let us discuss some properties of the generated two-photon field in Eq. (1.11). First, the delta function $\delta[\omega_p - (\omega_1 + \omega_2)]$ ensures conservation of energy of the down-converted photons. The delta function also demonstrates that the two-photon field is unnormalizable since it spreads out infinitely long in the time domain. Secondly, the spread in the total transverse momentum of the down-converted photon pair is limited by the spread in momentum of the incident beam $E(\mathbf{q}_1 + \mathbf{q}_2)$. Third, the phase-matching condition in Eq. (1.12) limits the spread along the $(\mathbf{q}_1 - \mathbf{q}_2)$ and $(\omega_1 - \omega_2)$ coordinates. The spread in the arrival time difference between the two down-converted photons is inversely proportional to the phase-matching bandwidth, i.e., the spread in the $(\omega_1 - \omega_2)$ coordinate. For type-I phase matching, the symmetry of the two-photon field under sign reversal of $(\omega_1 - \omega_2)$ implies that the average arrival time difference between the photons is zero. Finally, and maybe most importantly, the two photons are entangled because Eq. (1.11) does not factorize into two functions of the individual coordinates.

1.3.5 Klyshko picture

The Klyshko picture provides a very intuitive interpretation of spatial correlations between down-converted photons [48, 52, 71]. This interpretation follows one detected photon at $\mathbf{x}_1$ backwards in time to the generating crystal where is is converted into the second forward propagating photon via a virtual reflection at the (possibly curved) pump beam profile. The spatial profile of the coincidence rate $R_{\mathrm{cc}}(\mathbf{x}_1, \mathbf{x}_2)$ is now given by how well the two detectors "see each other" via this

* We note that the phase matching condition in Eq. (1.12) needs to be adjusted somewhat to properly describe type-II SPDC and quasi phase-matched processes. For type-II SPDC one must impose different functions $k_z(\mathbf{q}, \omega)$ for photon 1 and photon 2. For quasi phase-matched processes one must compensate the wave-vector mismatch with the poling period (see for example chapters 3 and 4).

reflecting path. The Klyshko picture is very convenient in use and will often provide a good first guess of what can be expected in two-photon coincidence experiments.

Nevertheless, the Klyshko picture has severe limitations as it does not involve aspects of phase matching. The phase-matching condition generally confines the angular spread of down-converted light and causes spectral and spatial aspects of the two-photon field to be correlated. The two-photon field in Eq. (1.11) can be adapted to a Klyshko-picture form by simply removing the sinc-function part, i.e.,

$$A(\mathbf{q}_1, \omega_1, \mathbf{q}_2, \omega_2; 0) \sim \delta[\omega_p - (\omega_1 + \omega_2)] E_p(\mathbf{q}_1 + \mathbf{q}_2; z = 0) \qquad \text{[Klyshko picture]}.$$

The Klyshko picture works well in the thin-crystal limit where $L \to 0$ in Eq. (1.11).

Phase-matching aspects are very important in this thesis. Therefore, the Klyshko picture is generally insufficient to understand our experimental results. In chapter 4, we utilize near-field aspects of the two-photon field, which result from the phase-matching condition. In chapter 5, the phase-matching condition limits the dimensionality of the entanglement and the size of the two-photon speckle spots. In chapter 6, we use type-II down-conversion where the allowed optical detection bandwidth is drastically reduced by the phase-matching condition as compared to type-I phase matching. Chapter 3 is entirely devoted to a detailed investigation of the phase-matching condition in our crystals.

1.4 Thesis outline

This thesis contains four published papers (chapters 2-5) and one yet unpublished work (chapter 6) on two-photon interference. All works can be read independently. You might wish to read only a few of them. Below, we have provided a catchy description of each chapter to facilitate your choice.

- **Chapter 2:** It is well known that light can carry orbital angular momentum. The down-converted photons in SPDC light are entangled via their orbital angular momentum. If one of the photons is detected with orbital angular momentum $+l\hbar$ then the other collapses into $-l\hbar$ since the total amount of orbital angular momentum is conserved in the down-conversion process. **In chapter 2, we experimentally determine the Schmidt coefficients of the OAM eigenstates via two-photon interference**.

- **Chapter 3: This chapter contains a thorough characterization of SPDC and second harmonic generation (SHG) in periodically poled KTiOPO$_4$**. The investigated spatial aspects of the phase-matching condition are essential for the two-photon field used in chapters 4-6. As a bonus, we discovered how the observed phase-matching rings in SPDC light contain quantitative information on the quality of the poling structure in the nonlinear crystal.

- **Chapter 4:** Finally, more than 200 years after Young's double-slit experiment, **we present a complete and comprehensive description of the double-slit experiment for the two-photon case**. Two-photon interference allows for a wide variety of different fringe patterns. We are the first to measure them all and with unprecedented quality (see cover of printed thesis). Our results are backed-up by our simple comprehensive model for two-photon double-slit fringe patterns. Special attention is paid to the two-photon phase front, an important aspect that has often been overlooked. To generate these patterns, we utilize phase-sensitive properties of the two-photon field in both the near-field and far-field of the non-linear crystal.

- **Chapter 5:** Wave propagation in random media has intrigued and occupied many physicists in the last five decades. The most prominent feature of a multiply scattered wave is its random interference pattern called speckle. We wondered what two-photon speckle patters with spatial entanglement would look like. **In chapter 5 we present the first observation of two-photon speckle patterns**. We have found out how the spatial structure within two-photon speckle patterns is related to the structure of the scattering medium. Spatial entanglement gives two-photon speckle a much richer structure than ordinary one-photon speckle.

- **Chapter 6:** Only a few exotic one-photon interference phenomena are known to survive averaging over different realizations of disorder. Examples are enhanced backscattering and Anderson localization of light. Read chapter 6 for a sneak preview in yet unpublished work on **the first observation of a two-photon interference phenomenon that survives averaging over different realizations of disorder**.

2

Orbital angular momentum analysis of high-dimensional entanglement

We describe a simple experiment that is ideally suited to analyze the high-dimensional entanglement contained in the orbital angular momenta (OAM) of entangled photon pairs. For this purpose we use a two-photon interferometer with a built-in image rotator and measure the two-photon visibility versus rotation angle. Mode selection with apertures allows one to tune the dimensionality of the entanglement; mode selection with spiral phase plates and fibers allows detection of a single OAM mode. The experiment is analyzed in two different ways: either via the continuous two-photon amplitude function or via a discrete modal (Schmidt) decomposition of this function. The latter approach proves to be very fruitful, as it provides a complete characterization of the OAM entanglement.

W. H. Peeters, E. J. K. Verstegen, and M. P. van Exter, *Orbital angular momentum analysis of high-dimensional entanglement*, Physical Review A **76**, 042302 (2007)

(Selected for the Virtual Journal of Quantum Information, October 2007)

2.1 Introduction

Spontaneous parametric down-conversion (SPDC), in which a pump photon splits into two photons of lower energy, is a common technique to produce quantum-entangled photon pairs [8, 16, 72, 73]. The generated photon pairs can be entangled in three degrees of freedom. The best studied form of entanglement is that of the polarization [72], which spans a two-dimensional space and can thus be described in terms of qubits. The two other forms of entanglement involve either the time-frequency entanglement or the position-momentum entanglement within the photon pair. As these forms of entanglement involve continuous variables, the states are contained in a space of much higher dimension and described by qunits instead of qubits. One of the first experiments on time-frequency entanglement was the two-photon interference experiment of Hong, Ou, and Mandel [8], who demonstrated photon bunching at equal arrival times. Other forms of time-frequency entanglement have recently been studied by Gisin et al. [73].

In this chapter, we will discuss the nature of spatial entanglement, where a measurement on the position-momentum of one photon fixes the spatial profile of the other. This form of entanglement is rapidly attracting more attention [16, 18, 74–77]. We will separate the spatial profiles in radial and azimuthal components and concentrate on the azimuthal part, which can be described in terms of the photon's orbital angular momentum (OAM).

The questions that we will address both theoretically and experimentally deal with the nature of the spatial entanglement: "How many modes are involved in the spatial entanglement?," "What is the profile of these spatial eigenmodes?," "How can we separate the radial and azimuthal components?," and "What is the intensity distribution over the orbital angular momentum (OAM) modes and the related Schmidt number?" For our experimental analysis of the nature of the OAM entanglement, we will use a two-photon interferometer with an odd number of mirrors and an image rotator in one of its arms. A measurement of the two-photon interference as a function of the rotation angle proves to be sufficient for a full characterization of the OAM entanglement. This chapter addresses the theory and confirms and extends earlier experimental results from our group [22].

This chapter is organized as follows. In Secs. 2.2 and 2.3 we present two different theoretical descriptions of the interference in a two-photon Hong-Ou-Mandel (HOM) interferometer with a built-in rotator. The first analysis is based on a continuous representation of the two-photon amplitude function $A(\mathbf{x}_1, \mathbf{x}_2)$. The second analysis uses a modal decomposition of the detected two-photon amplitude into a discrete set of eigenmodes. This analysis yields an important and intuitively simple expression for the angle-dependent two-photon interference as a Fourier series over the OAM eigenmodes. In Sec. 2.4 we present our setup and the obtained experimental results. We demonstrate that our method allows for a full characterization of the entanglement in orbital angular momentum. We apply this method both to a spatially filtered beam and a single-mode beam with a fixed OAM. We end with a concluding discussion in Sec. 2.5.

2.2 Continuous two-photon amplitude

2.2.1 Generated two-photon amplitude

The two-photon amplitude that is generated in spontaneous parametric down-conversion (SPDC) is relatively simple in the quasi-monochromatic paraxial thin-crystal limit, which applies to our experiment. We use a cw monochromatic pump (at angular frequency ω_p) with perfect spatial coherence and consider almost frequency-degenerate SPDC, where both photons have approximately the same angular frequency $\omega_0 \equiv \omega_p/2$. We operate in the paraxial regime, with generated beams close to the direction of the pump beam. Finally, we take care to operate in the thin-crystal limit, where phase matching is well satisfied within the narrow spectral bandwidth and limited spatial extent of the detection system [56].

In the thin-crystal limit, the generated two-photon field amplitude is [78]

$$A_g(\mathbf{r}_s, \mathbf{r}_i) \propto \int h(\mathbf{r}_s, \mathbf{x}) h(\mathbf{r}_i, \mathbf{x}) E_p(\mathbf{x}) d\mathbf{x}, \tag{2.1}$$

where $E_p(\mathbf{x})$ is the field profile of the pump beam at the crystal ($z = 0$) with transverse coordinate $\mathbf{x}$. The three dimensional vectors $\mathbf{r}_s$ and $\mathbf{r}_i$ are the coordinates of the two-photon amplitude. The one-photon propagators $h(\mathbf{r}_{s,i}, \mathbf{x}) = k_{s,i}/(2\pi i L_{s,i}) \exp(ik_{s,i}L_{s,i})$ describe free space propagation of either signal or idler photon from the crystal to the detector, where $k_{s,i} \equiv \omega_{s,i}/c$ are their wave numbers (obeying $\omega_s + \omega_i = \omega_p$) and $L_{s,i} = |\mathbf{r}_{s,i} - (\mathbf{x}, 0)|$ their path lengths.

In the quasimonochromatic paraxial thin-crystal limit, one can express the generated two-photon amplitude in terms of the pump field behind the crystal. The precise form of this relation depends on the chosen coordinate system [69, 79]. For noncollinear SPDC, we will use “beam coordinates” in which the signal and idler coordinates of the generated two-photon amplitude are defined with respect to two fixed beam axes pointing in the $-\theta_0$ and $+\theta_0$ directions, respectively. We use $\delta\mathbf{x}_{s,i}$ for the transverse coordinates of the signal and idler photon and L_0 for the propagation length along each beam axis (see Fig. 2.1). In the paraxial limit ($\theta_0 \ll 1$ and $|\mathbf{x}|, |\delta\mathbf{x}_{s,i}| \ll L_0$) the photon propagation lengths $L_{s,i}$ become

$$L_{s,i} = L_0 \pm x_x\theta_0 + \frac{|\delta\mathbf{x}_{s,i} - \mathbf{x}|^2}{2L_0}, \tag{2.2}$$

where x_x is the x-component of $\mathbf{x}$, which is the component in the plane defined by

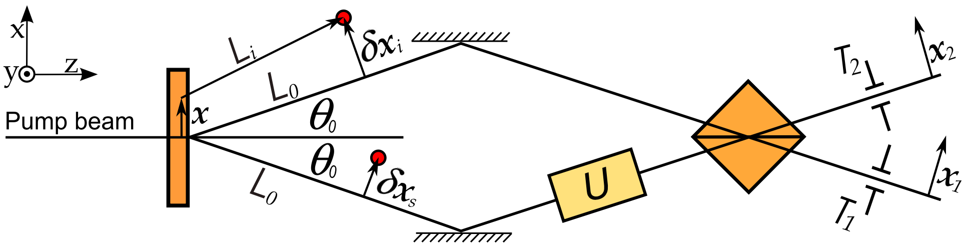

Figure 2.1: Sketch of a two-photon interferometer containing a built-in image transformation U and the definition of various beam coordinates. We use the following transverse coordinates: $\delta\mathbf{x}_s$ and $\delta\mathbf{x}_i$ for the relative positions within the signal and idler beams, and $\mathbf{x}_1$ and $\mathbf{x}_2$ for the positions at the detectors, again with respect to fixed beam lines. L_0 is the distance along a fixed beam line from the crystal to the detection planes. The photon propagation lengths $L_{i,s}$ and the transverse position on the crystal $\mathbf{x}$ are used in the integrand of Eq. (2.1) to calculate the two-photon amplitude.

the z axis and the two beam axes. Finally, also working in the quasimonochromatic limit ($|k_s - k_i| \ll k_p$), the generated two-photon amplitude of Eq. (2.1) becomes

$$A_g(\delta\mathbf{x}_s, \delta\mathbf{x}_i, L_0) \propto \frac{E_z\left[\frac{1}{2}(\delta\mathbf{x}_s + \delta\mathbf{x}_i)\right]}{L_0} \exp\left(\frac{ik_p}{8L_0}|\delta\mathbf{x}_s - \delta\mathbf{x}_i|^2\right), \tag{2.3}$$

where $E_z(\mathbf{x})$ is the pump profile in the transverse plane at a distance $z = L_0$ behind the crystal [79]. The advantage of beam coordinates in comparison with Cartesian coordinates is that the phase factor relating E_z and A_g is much smaller in beam coordinates. Equation (2.3) shows that the generated two-photon amplitude is not only invariant under permutation of the Cartesian coordinates $\mathbf{r}_s \leftrightarrow \mathbf{r}_i$, but even remains unchanged under permutation of the local beam coordinates $\delta\mathbf{x}_s \leftrightarrow \delta\mathbf{x}_i$.

2.2.2 Interference after image rotation

In this subsection we will first present a theoretical description of a two-photon interferometer with an image transformation U in one of its arms (see Fig. 2.1). An image transformation U acts as a coordinate transformation of the form $E_{\text{out}}(\mathbf{x}_{\text{out}}) = E_{\text{out}}(U\mathbf{x}_{\text{in}}) = E_{\text{in}}(\mathbf{x}_{\text{in}}) = E_{\text{in}}(U^{-1}\mathbf{x}_{\text{out}})$. We will then derive an expression for the two-photon bunching visibility, assuming U to be an orthogonal matrix (comprising image rotations and reflections) and the pump beam to be rotationally symmetric. In the final part we will focus on the important experimental case of an interferometer with an odd number of mirrors and an image rotator, as only this interferometer allows for a characterization of the OAM entanglement (see below).

In order to calculate the detected coincidence rate, we need to express the two-photon amplitude at the detectors $A_{12}(\mathbf{x}_1, \mathbf{x}_2)$ in terms of the generated field $A_g(\delta\mathbf{x}_s, \delta\mathbf{x}_i)$. We do so by accumulating all image operations for the two relevant propagation channels, being the "double transmission" and "double reflection" of the incident photon pair at the beam splitter. For the double transmission channel, these operations are $\mathbf{x}_2 = UM_y\mathbf{x}_s$ and $\mathbf{x}_1 = M_y\mathbf{x}_i$, whereas the double reflection channel corresponds to $\mathbf{x}_1 = M_yUM_y\mathbf{x}_s$ and $\mathbf{x}_2 = \mathbf{x}_i$. Here, the operations M_y arise from reflections on the mirrors and beam splitter in the interferometer. The two-photon amplitude at the detectors thus becomes

$$\begin{aligned} A_{12}(\mathbf{x}_1, \mathbf{x}_2; \Delta\omega) \quad = \quad & T_{\mathrm{bs}} e^{-i\frac{1}{2}\Delta\omega\tau} A_g(M_y U^{-1}\mathbf{x}_2, M_y\mathbf{x}_1) \\ & -R_{\mathrm{bs}} e^{i\frac{1}{2}\Delta\omega\tau} A_g(M_y U^{-1} M_y\mathbf{x}_1, \mathbf{x}_2), \end{aligned} \tag{2.4}$$

where $\Delta\omega \equiv \omega_1 - \omega_2$ is the angular frequency difference between photons 1 and 2 and $\tau \equiv (L_s - L_i)/c$ is the time delay difference in the interferometer. T_{bs} and R_{bs} are the intensity transmission and reflection coefficients of the beam splitter, which can also be written as $T_{\mathrm{bs}} = t^2$ and $-R_{\mathrm{bs}} = (ir)^2$, where t and r are the real-valued amplitude transmission and reflection coefficients of the beam splitter. We will assume the beam splitter to be balanced at $T_{\mathrm{bs}} = R_{\mathrm{bs}} = \frac{1}{2}$. The coincidence rate for simultaneous photon detection with large (bucket) detectors behind two apertures with transmission profiles $T_1(\mathbf{x}_1)$ and $T_2(\mathbf{x}_2)$ is obtained after spatial and spectral integration via

$$R_{\mathrm{cc}}(\tau) \propto \iiint |A_{12}(\mathbf{x}_1, \mathbf{x}_2; \Delta\omega)|^2 T_1(\mathbf{x}_1) T_2(\mathbf{x}_2) T_{\mathrm{tot}}(\Delta\omega) d\mathbf{x}_1 d\mathbf{x}_2 d\Delta\omega, \tag{2.5}$$

where $T_{\mathrm{tot}}(\Delta\omega) \equiv T_{f1}(\omega_0 + \frac{1}{2}\Delta\omega) T_{f2}(\omega_0 - \frac{1}{2}\Delta\omega)$ and $T_{f1}(\omega)$ and $T_{f2}(\omega)$ are the intensity transmission spectra of the bandpass filters situated in front of detectors 1 and 2.

Two-photon interference can best be observed by measuring the coincidence rate R_{cc} as a function of the time delay τ experienced in the interferometer. We distinguish two extreme cases for the time delay: $\tau = \infty$, where interference is absent, and $\tau = 0$, where the interference is strong and where one generally observes a so-called Hong-Ou-Mandel (HOM) dip [8] in the coincidence rate $R_{\mathrm{cc}}(\tau)$. We quantify the strength of the two-photon interference, i.e., the depth of HOM dip, by defining the two-photon bunching visibility as

$$V \equiv 1 - \frac{R_{\mathrm{cc}}(\tau = 0)}{R_{\mathrm{cc}}(\tau = \infty)}. \tag{2.6}$$

The two-photon bunching visibility of our interferometer with built-in image transformation U (see Fig. 2.1) can now be calculated by combining Eqs. (2.3)-(2.6). In order to simplify the final expression we will restrict our analysis in three ways.

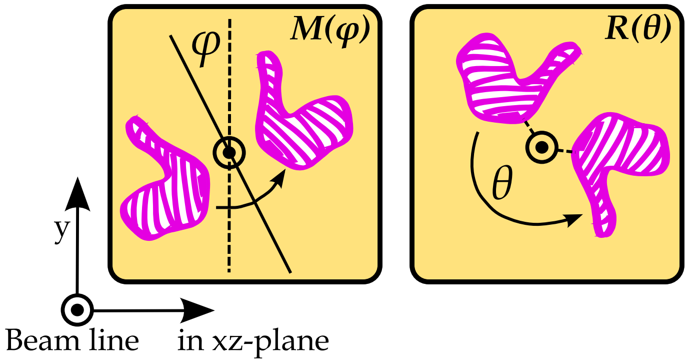

Figure 2.2: Graphical representation of the two generic orthogonal image transformations $M(\phi)$ and $R(\theta)$ in a plane orthogonal to a beam line. The beam line is pointing out of the paper. $M(\phi)$ is a reflection in a line making an angle ϕ with the y axis. $R(\theta)$ is a rotation of an angle θ around the beam line.

First, we assume the pump field to be rotationally-symmetric with zero orbital angular momentum. Second, we consider only orthogonal image transformations which comprise any combination of image reflections and image rotations (see Fig. 2.2). We define $M(\phi)$ as an image reflection in a line oriented at an angle ϕ with respect to the y axis, and $R(\theta)$ as an image rotation over an angle θ. Finally, we assume one aperture to be fully open, i.e., $T_1(\mathbf{x}_1) = 1$.

The first two restrictions allow us to combine all image operations into a single matrix $U_{\text{tot}} = UM_yUM_y$ and reduce the two-photon amplitudes in Eq. (2.4) to $A_g(\mathbf{x}_1, \mathbf{x}_2)$ and $A_g(\mathbf{x}_1, U_{\text{tot}}\mathbf{x}_2)$. The third restriction allows us to isolate the transverse correlation function of the pump field. The expression for the two-photon bunching visibility thus becomes

$$V(\theta) = \frac{\displaystyle\int \tilde{g}_z\left[\tfrac{1}{2}(U_{\text{tot}} - 1)\mathbf{x}_2\right] T_2(\mathbf{x}_2) d\mathbf{x}_2}{\displaystyle\int \tilde{g}_z(\mathbf{0}) T_2(\mathbf{x}_2) d\mathbf{x}_2}, \tag{2.7}$$

where the normalized correlation function of the pump field (in spherical coordinates) is defined as

$$\tilde{g}_z(\delta\mathbf{x}) = \frac{\displaystyle\int \tilde{E}_z^*\left(\mathbf{x} + \tfrac{1}{2}\delta\mathbf{x}\right) \tilde{E}_z\left(\mathbf{x} - \tfrac{1}{2}\delta\mathbf{x}\right) d\mathbf{x}}{\displaystyle\int \left|\tilde{E}_z(\mathbf{x})\right|^2 d\mathbf{x}}. \tag{2.8}$$

This function is always real-valued due to the symmetry of the pump. The pump field $\tilde{E}_z(\mathbf{x})$ in spherical coordinates is related to the pump field in Cartesian coordinates as

$$\tilde{E}_z(\mathbf{x}) \equiv E_z(\mathbf{x}) \exp\left(-\frac{ik_p}{2z}|\mathbf{x}|^2\right). \tag{2.9}$$

Note that we have incorporated all phase factors in $\tilde{E}_z(\mathbf{x})$, by choosing a convenient spherical coordinate system that has its origin at the center of the pump spot on the crystal. The pump profile $\tilde{E}_z(\mathbf{x})$ becomes real-valued in the far field, but is complex in the near field. As a result, only the far-field correlation function is directly related to the intensity profile of the pump in the detection plane. The near-field correlation function on the other hand is much narrower than the pump profile in the corresponding plane. For the experimentally important case of a Gaussian TEM$_{00}$ pump that is mildly focussed at the crystal as $E_0(\mathbf{x}) \propto \exp\left(-|\mathbf{x}|^2/w_0^2\right)$, this correlation function is

$$\tilde{g}_z(\mathbf{x}) \propto \exp\left[-\frac{|\mathbf{x}|^2}{2w_z^2}\left(1+\frac{z_0^2}{z^2}\right)\right], \tag{2.10}$$

where $w_z = w_0\sqrt{1+(z/z_0)^2}$ is width of the pump beam in the detection plane and $z_0 \equiv \frac{1}{2}k_p w_0^2$ is the Rayleigh range of the pump beam.

There are two distinct possibilities for the orthogonal matrix U_{tot}. If the built-in operation in Fig 2.1 is an image rotation $U = R(\theta)$, the combined matrix U_{tot} is equal to unity and hardly interesting. If the built-in operation is an image reflection $U = M(\phi) = R(2\phi)M_y$, the combined operation $U_{\text{tot}} = R(4\phi)$ is a rotation over an angle 4ϕ. If the interferometer contains more than two mirrors, it can still be reduced to one of these two generic cases by absorbing the extra reflections in the effective image transformation U in Fig 2.1.

We will study the case where the effective image transformation U is an image reflection in more detail. We call this system an "odd-R" interferometer, to indicate that it operates as an interferometer containing an odd number of mirrors in between crystal and beam splitter and an image rotator $R(\theta) = M(\theta/2)M_y$ in one of its arms. We will evaluate Eq. (2.7) for this odd-R geometry, where the relation $U_{\text{tot}} = R(2\theta)$ yields $\left|\frac{1}{2}(U_{\text{tot}}-1)\mathbf{x_2}\right| = \sin\theta|\mathbf{x_2}|$. We consider a geometry that comprises a Gaussian TEM$_{00}$ pump beam and a "hard-edged" circular aperture with a top-hat transmission profile $T_2(\mathbf{x_2}) = \Theta(1-|\mathbf{x_2}|/a)$ of radius a positioned in the far field of this beam ($L_0 \gg z_0$). For this geometry, the two-photon bunching visibility [Eq. (2.7)] becomes

$$V(\theta) = \frac{1-\exp(-\xi)}{\xi}, \tag{2.11}$$

where $\xi = \frac{1}{2}(a/w_z)^2\sin^2\theta$. Note that the predicted two-photon visibility $V(\theta)$ is symmetric under inversion of the rotation angle $[V(-\theta) = V(\theta)]$ and periodic in π instead of 2π radian $[V(\theta+\pi) = V(\theta)]$.

Our key result of Eq. (2.11) quantifies the effect of spatial labeling on the two-photon interference. If the aperture $T_2(\mathbf{x})$ is much smaller than the transverse correlation length w_z of the pump, we expect $V(\theta) \approx 1$ irrespective of the rotational angle θ, as the diffraction limit of the aperture frustrates the observation of any image rotation or reflection. If the aperture is much larger, diffraction will be less restrictive and $V(\theta)$ will decay rapidly away from $\theta = 0$. The two-photon interference should disappear if one can distinguish the signal from the idler path based on any conceivable photon position measurement at the detector side, even if that measurement is not actually performed but only possible in principle. Mathematically, the criterion for spatial labeling translates into $\sqrt{2\xi} = (a/w_z)\sin(\theta) \gg 1$.

2.3 Discrete modal analysis

2.3.1 Schmidt decomposition of the detected two-photon amplitude

In the previous section we have analyzed two-photon interference in a two-photon interferometer with an image transformation U in one of its arms (see Fig. 2.1). We considered the case of a rotationally symmetric pump profile and an orthogonal image transformation matrix U, comprising any combination of image reflections and rotations as visualized in Fig. 2.2. We found out that the two-photon bunching visibility is only affected by U if U is an image reflection $M(\theta/2)$, which is equivalent to an image rotation in combination with an extra mirror $R(\theta)M_y$. An expression for $V(\theta)$ is given by Eq. (2.11) for detection through a hard-edged circular aperture in front of one of the detectors. Our analysis that lead to this result was based on calculations of the continuous two-photon amplitude in the quasi-monochromatic paraxial thin-crystal limit.

In this subsection we will analyze the two-photon interference that leads to Eq. (2.11) from a different perspective, namely by decomposing the continuous two-photon amplitude into a countable set of discrete spatial modes. We will consider the *detected* two photon amplitude [80] in stead of the *generated* two-photon amplitude [9, 81]. As we will show, the rotational symmetry of the pump and the apertures allows for a decomposition of the detected two-photon amplitude in a Fourier series of orbital angular momenta. This azimuthal decomposition is a first step towards a full Schmidt decomposition [9, 82, 83] of the detected field. Our Schmidt decomposition of the *detected* field is mathematically equivalent to the Schmidt decomposition of the *generated* field as performed in ref. [9].

We have shown in the previous section that rotational symmetry of the pump field ($l = 0$ pumping) leads to invariancy of the two-photon amplitude under any orthogonal transformation U on both beam coordinates, i.e., that $A_g(U\delta\mathbf{x}_s, U\delta\mathbf{x}_i) = A_g(\delta\mathbf{x}_s, \delta\mathbf{x}_i)$. Based on this symmetry we can rewrite $A_g(\delta\mathbf{x}_s, \delta\mathbf{x}_i)$ as $A_g(r_s, r_i, \phi_{si})$, where $\phi_{si} \equiv \phi_s - \phi_i$. Here, we have introduced polar coordinates $\delta\mathbf{x}_{s,i} \leftrightarrow (r_{s,i}, \phi_{s,i})$,

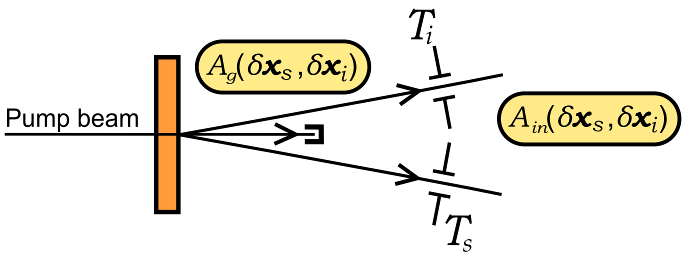

Figure 2.3: Graphical representation of what we call the detected two-photon amplitude $A_{\text{in}}(\delta\mathbf{x}_s, \delta\mathbf{x}_i)$ in relation to the generated two-photon amplitude $A_g(\delta\mathbf{x}_s, \delta\mathbf{x}_i)$.

where ϕ is the angle with the y axis and the sign of ϕ is defined in analogy with the definition of $R(\theta)$ in Fig. 2.2. The detected two-photon amplitude is obtained by including the spatial filtering of two rotationally symmetric apertures $T_{s,i}(r_{s,i})$ in the signal and idler beam (see Fig. 2.3). We analyze the angular dependence of this detected field by decomposing it in a Fourier series of orbital angular momenta l, via

$$\begin{aligned} A_{\text{in}}(r_s, r_i, \phi_{si}) &\equiv \sqrt{T_s(r_s)T_i(r_i)}A_g(r_s, r_i, \phi_{si}) \\ &= A \sum_{l=-\infty}^{\infty} F_l(r_s, r_i)\sqrt{P_l}\, e^{il\phi_{si}}/2\pi, \end{aligned} \tag{2.12}$$

where $A^2 \equiv \iint |A_{\text{in}}(\delta\mathbf{x}_s, \delta\mathbf{x}_i)|^2 d\delta\mathbf{x}_s d\delta\mathbf{x}_i$ is the average squared amplitude. Furthermore we have $F_l(r_s, r_i) = F_{-l}(r_s, r_i)$ and $P_{-l} = P_l$, because of mirror symmetry. The functions $F_l(r_s, r_i)$ are normalized via [9]

$$\int_0^\infty \int_0^\infty |F_l(r_s, r_i)|^2 r_s r_i dr_s dr_i = 1, \tag{2.13}$$

so that $\sum P_l = 1$.

Equation (2.12) is a first step towards a full Schmidt decomposition of the detected two-photon amplitude. This decomposition can be completed by expanding [9]

$$F_l(r_s, r_i)\sqrt{r_s r_i} = \sum_{p=0}^{\infty} \sqrt{\gamma_{l,p}} f_{l,p}(r_s) g_{l,p}(r_i), \tag{2.14}$$

where the radial mode number p quantifies the number of nodal lines in the radial profile of $f_{l,p}(r_s)$ and $g_{l,p}(r_i)$. The functions $f_{l,p}(r_s)$ and $g_{l,p}(r_i)$ are normalized via the standard inner product so that $\sum_p \gamma_{l,p} = 1$. The full Schmidt decomposition of the detected two-photon amplitude now reads

$$A_{\text{in}}(\delta\mathbf{x}_s, \delta\mathbf{x}_i) = A \sum_{l=-\infty}^{\infty} \sum_{p=0}^{\infty} \sqrt{\lambda_{l,p}} u_{l,p}(\delta\mathbf{x_s}) v_{-l,p}(\delta\mathbf{x_i})\,, \tag{2.15}$$

where $\lambda_{l,p} \equiv P_l \gamma_{l,p}$ and $u_{l,p}(\delta\mathbf{x_s}) \equiv e^{il\phi_s} f_{l,p}(r_s)/\sqrt{2\pi r_s}$ and $v_{l,p}(\delta\mathbf{x_i}) \equiv e^{il\phi_i} g_{l,p}(r_i)/\sqrt{2\pi r_i}$.

We now return to the HOM interference setup visualized in Fig. 2.1 with an image transformation $U = R(\theta)M_y$. We reposition the apertures $T_s(r_s)$ and $T_i(r_i)$ in front of the detectors 2 and 1, respectively. Because the generated field $A_g(\delta\mathbf{x}_s, \delta\mathbf{x}_i)$ is invariant under a coordinate swap $\delta\mathbf{x}_s \leftrightarrow \delta\mathbf{x}_i$, we can write the two-photon amplitude behind the apertures T_1 and T_2 in terms of the detected two-photon amplitude, i.e.,

$$\begin{aligned} A_{\text{HOM}}(\mathbf{x}_1, \mathbf{x}_2) \;=\; & T_{\text{bs}} e^{-i\frac{1}{2}\Delta\omega\tau} A_{\text{in}}(r_2, r_1, \phi_1 + \phi_2 - \theta) \\ & - R_{\text{bs}} e^{i\frac{1}{2}\Delta\omega\tau} A_{\text{in}}(r_2, r_1, \phi_1 + \phi_2 + \theta)\,, \end{aligned} \tag{2.16}$$

where $\Delta\omega \equiv \omega_1 - \omega_2$ is the angular frequency difference between photons 1 and 2 and $\tau \equiv (L_s - L_i)/c$ is the time delay difference in the interferometer. The only difference between Eq. (2.4) and Eq. (2.16) is that the latter incorporates the transmission profiles of the detection apertures whereas Eq. (2.4) does not.

The two-photon bunching visibility as defined in Section 2.2 is now easily calculated by using the azimuthal Schmidt decomposition of the detected two-photon amplitude as given in Eq. (2.12). By substituting Eq. (2.12) in Eq. (2.16), assuming a balanced beam splitter $R_{\text{bs}} = T_{\text{bs}} = \frac{1}{2}$, and using the prescriptions of Eqs. (2.5) and (2.6) one quickly finds

$$V(\theta) = \sum_{l=-\infty}^{\infty} P_l \cos(2l\theta). \tag{2.17}$$

In other words, a measurement of $V(\theta)$ with the HOM setup as visualized in Fig. 2.1 (with $U = R(\theta)M_y$) reveals the azimuthal Schmidt coefficients P_l of the detected two-photon amplitude. This key result will be discussed in more detail in Subsection 2.3.3.

The OAM weights P_l depend on the size and radial shape of the circular detection apertures $T_{1,2}$ in relation to the profile of the pump laser in the detection plane, as these determine the detected two-photon amplitude $A_{\text{in}}(r_s, r_i, \phi_{si})$ and its angular Fourier components $AF_l(r_s, r_i)\sqrt{P_l}/2\pi$. These OAM weights are often difficult to calculate. For our geometry with a Gaussian pump and a single hard-edged aperture, we didn't find analytic expressions for P_l, as we couldn't solve the Fourier decomposition of Eq. (2.11) or Eq. (2.12) analytically.

2.3.2 Modal decomposition and the Schmidt number

In this subsection we will introduce a convenient coordinate free bra-ket notation for the detected two-photon state (see Fig. 2.3) and use the Schmidt decomposition to quickly rederive the previous results of Eq. (2.16) and Eq. (2.17). We will also introduce two different Schmidt numbers.

A Schmidt decomposition of the detected two photon state $|\Psi\rangle_{\text{in}}$ in bra-ket form is

$$|\Psi\rangle_{\text{in}} = \sum_{\mu} \sqrt{\lambda_{\mu}}\ |u_{\mu}\rangle \otimes |v_{\mu}\rangle, \tag{2.18}$$

where $\{|u_{\mu}\rangle\}$ and $\{|v_{\mu}\rangle\}$ are two sets of orthogonal mode functions, which are identical only if the aperture profiles T_s and T_i are identical. The effective number of modes involved in this decomposition is defined by the so-called (2D) Schmidt number

$$K_{\text{2D}} \equiv \frac{\left(\sum_{\mu} \lambda_{\mu}\right)^2}{\sum_{\mu} \lambda_{\mu}^2}. \tag{2.19}$$

The rotation symmetry of the detected two-photon amplitude $A_{\text{in}}(U\delta\mathbf{x}_s, U\delta\mathbf{x}_i) = A_{\text{in}}(\delta\mathbf{x}_s, \delta\mathbf{x}_i)$ allows one to separate the mode index μ into an azimuthal mode number l and a radial mode number p. It also enforces the conservation of OAM in the paraxial SPDC process [84] and changes the modal decomposition of Eq. (2.18) to

$$|\Psi\rangle_{\text{in}} = \sum_{l=-\infty}^{\infty} \sum_{p=0}^{\infty} \sqrt{\lambda_{l,p}}\ |l,p\rangle' \otimes |-l,p\rangle'', \tag{2.20}$$

where $|l,p\rangle'$ and $|-l,p\rangle''$ are the LG-like Schmidt eigenmodes of the detected two-photon amplitude. This equation is the bra-ket notation of Eq. (2.15), where $|l,p\rangle'$ and $|-l,p\rangle''$ correspond to the functions $u_{l,p}(\delta\mathbf{x}_s)$ and $v_{-l,p}(\delta\mathbf{x}_i)$, respectively. As the amplitude coefficients $\sqrt{\lambda_{l,p}}$ already contain the effects of aperture filtering, they will decrease rapidly both for high p and high l values (high l states are quite extended even for $p = 0$). We define the OAM probability as $P_l \equiv \sum_p \lambda_{l,p}$ and the related azimuthal Schmidt number as

$$K_{\text{az}} \equiv \frac{1}{\sum_l P_l^2}, \tag{2.21}$$

for $\sum_l P_l = 1$ *. The relation between the azimuthal Schmidt number K_{az} and the full 2D Schmidt number K_{2D}, depends on the radial profile of the detection

* The OAM probability P_l and azimuthal Schmidt number K_{az} that we introduce are closely related to the spiral weight and spiral bandwidth introduced in refs. [81] and [85]; both single out the azimuthal behavior by summing over all radial mode numbers

aperture.

We now return to the HOM interference setup visualized in Fig. 2.1 with an image transformation U. Starting from the modal decomposition of Eq. (2.20), it is relatively easy to apply the rotation and mirror operations that are needed to evaluate the doubly reflected and doubly transmitted field and the visibility of their interference. For the even-R geometry [$U = R(\theta)$], the generated $(l, -l)$ pairs are also detected as $(l, -l)$ pairs behind the beam splitter and we expect good two-photon interference, i.e., $V(\theta = 1)$, at any rotation angle. For the odd-R geometry [$U = R(\theta)M_y$], the OAM inversion produced by the extra mirror leads to the detection of (l, l) and $(-l, -l)$ pairs instead. As the OAM at the rotator is now different for the doubly reflected and doubly transmitted path, so is the effect of rotation. For rotation over an angle θ the combined two-photon state after HOM interference can now be written as

$$
\begin{aligned}
|\Psi\rangle_{\mathrm{HOM}} \quad = \quad & \sum_{l,p} \Big[T_{\mathrm{bs}} \sqrt{\lambda_{l,p}}\, e^{-i(l\theta + \frac{1}{2}\Delta\omega\tau)} \\
& - R_{\mathrm{bs}} \sqrt{\lambda_{-l,p}}\, e^{i(l\theta + \frac{1}{2}\Delta\omega\tau)} \Big] |l,p\rangle' \otimes |l,p\rangle''. \qquad (2.22)
\end{aligned}
$$

This is the bra-ket notation of Eq. (2.16). Next, we assume a balanced beam splitter ($R_{\mathrm{bs}} = T_{\mathrm{bs}} = \frac{1}{2}$) and use the reflection symmetry $\lambda_{l,p} = \lambda_{-l,p}$ (and $P_l = P_{-l}$) to obtain

$$
V(\theta) = \sum_{l=-\infty}^{\infty} P_l \cos(2l\theta), \qquad (2.23)
$$

where we normalized to $\sum_l P_l = 1$ [equivalent to $V(0) = 1$]. With the convenient bra-ket notation, we thus recover the important Eq. (2.17) in only a few steps.

2.3.3 The physical significance of $V(\theta)$

Equation (2.23) shows how the observed visibility $V(\theta)$ is a weighted sum over contributions from groups of l modes, each contribution oscillating between $V_l = 1$ (HOM dip) and $V_l = -1$ (HOM peak) with its own angular dependence $\cos(2l\theta)$. It thereby shows how the visibility $V(\theta)$ and the modal distribution $\{P_l\}$ are related via a simple Fourier series. As a Fourier transformation of $V(\theta)$ directly yields the full OAM distribution $\{P_l\}$, it thus provides for a complete characterization of the angular structure of the two-photon amplitude.

The azimuthal Schmidt number K_{az} is a measure for the angular structure in the detected two-photon amplitude. More precisely, by averaging $V(\theta)^2$ over the full rotation range one finds

$$
K_{\mathrm{az}} = \frac{1}{\sum P_l^2} = \frac{1}{\langle V(\theta)^2 \rangle}. \qquad (2.24)
$$

When $V(\theta)$ remains close to $V(0) = 1$ over its full range, this relation gives $K_{\text{az}} \approx 1$. When $V(\theta) = \cos(2l\theta)$ this relation gives $K_{\text{az}} = 2$ as expected for $P_l = P_{-l} = \frac{1}{2}$. When $V(\theta) \approx 1$ only in a very limited range around $\theta = 0$ and zero for all other angles, $K_{\text{az}} \gg 1$ is inversely proportional to the angular width of $V(\theta)$.

In one of our experiments we use a single-mode detector that only selects photons with a specific OAM value l_d. We predict that the coincidence rate versus time delay $R_{\text{cc}}(\theta, \tau)$ now contains both a symmetric and (surprisingly) also an anti-symmetric part with respect to time delay τ. Using the detected two-photon state after HOM interference of Eq. (2.22) for a single $l = l_d$ number we find

$$R_{\text{cc}}(\theta, \tau) \propto \int [1 + \cos(\Delta\omega\tau + 2l_d\theta)]\, T_{\text{tot}}(\Delta\omega) d\Delta\omega, \tag{2.25}$$

where $T_{\text{tot}}(\Delta\omega)$ is defined below Eq. (2.5). This equation shows that $R_{\text{cc}}(\theta, \tau)$ will have an antisymmetric component with respect to τ only if $T_{\text{tot}}(\Delta\omega)$ is asymmetric and if $\sin(2l\theta) \neq 0$. Note that $T_{\text{tot}}(\Delta\omega)$ is only asymmetric if the filter transmission spectra $T_{f1}(\omega)$ and $T_{f2}(\omega)$ are different. For the two-photon bunching visibility at zero delay, which solely depends on the symmetric part, we find the earlier result of Eq. (2.23), which now reduces to $V(\theta) = \cos(2l_d\theta)$.

Finally, one might wonder what the observed visibility $V(\theta)$ tells us about the nature of the spatial entanglement, i.e., whether it proofs that the two-photon amplitude is indeed described by the pure state of Eq. (2.20) with its perfect OAM entanglement? This question is best answered by arguing backwards from hypothetical detected pairs (l_1, l_2). For an even-R interferometer, our experimental observation that $V(\theta) \approx 1$ irrespective of rotation angle indeed proofs the conservation of OAM; it shows that the two-photon field at the detectors contains only $(l, -l)$ pairs, as any other pairs (l_1, l_2) would introduce an angle dependence of the form $\cos(2(l_1 + l_2)\theta)$ in $V(\theta)$. However, as the same result $V(\theta) \approx 1$ would have been obtained for any classical mixture of $(l, -l)$ pairs, this observation doesn't proof the existence of quantum entanglement. For the odd-R interferometer, the observations on $V(\theta)$ discussed in this chapter does proof some form of quantum entanglement. It shows that the two-photon amplitude contains only coherent superpositions of the form $|\Psi\rangle = |l, -l\rangle + |-l, l\rangle$. Again, we cannot exclude any incoherent mixture of these superposition states.

2.4 Experimental results

2.4.1 Experimental setup

Our experimental setup, as shown in Fig. 2.4, is a two-photon (Hong-Ou-Mandel type) interferometer with an odd number of mirrors and an image rotator in one of the arms. A cw krypton-ion laser (Coherent Innova 300) emits 210 mW at 413.1 nm

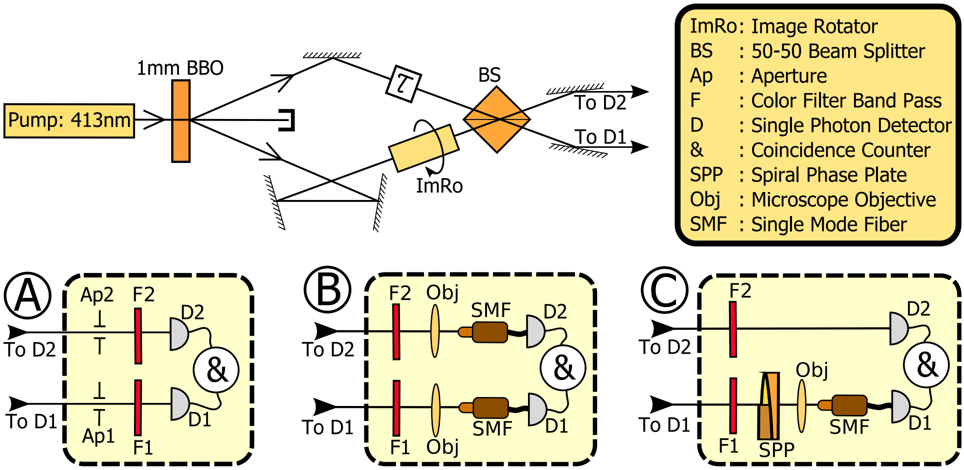

Figure 2.4: Experimental setup: A two-photon interferometer with an odd number of mirrors and a built-in image rotator. The τ-icon represents an adjustable delay line. Behind the beam splitter three different detection geometries can be chosen: A, B, or C.

in a vertically polarized pure TEM_{00} mode. The beam is mildly focussed ($w_p = 270\ \mu$m is the radius at e^{-2} of maximum irradiance) on a 1 mm thick β-BaB_2O_4 crystal (BBO) with a cutting angle of 29.2°. The crystal is tilted such that we obtain type I spontaneous parametric down conversion (SPDC) where the SPDC light is emitted in a cone extending over a full opening angle of $2\theta_0 = 3.2°$ around the pump beam. After multiple reflections and a single transit through the image rotator, two opposite parts of this cone are combined on a beam splitter. The crucial angular alignment of this beam splitter is performed with computer-controlled actuators. Behind the 50/50 beam splitter, three different detection geometries can be chosen (described in more detail in the next paragraph). Color filters are positioned in front of the detectors in all detection geometries. The filters are custom-made bandpass filters (Chroma Technology Corporation), filtering around 826 nm with a FWHM of 5 nm. The detectors in all three detection geometries are single photon sensitive avalanche photodiodes (Perkin Elmer SPCM-AQR-14).

Detection geometry A consists of a relatively large (bucket) detector behind an aperture (at 0.10 m from the beam splitter) in each detection arm. Each detector will collect all the light that passes through its aperture. In detection geometry B, each detector is connected to a single-mode fiber collecting only the fundamental Gaussian mode. In detection geometry C, one of the detectors is connected to a single-mode fiber in combination with a spiral phase plate (SPP) making it effectively a single-mode $l = 1$ detector, while the other detecting arm contains a bucket detector. A more detailed description of the $l = 1$ single-mode detector and the

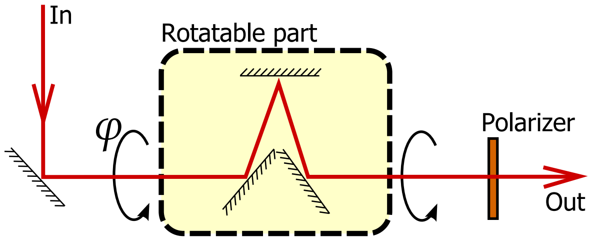

Figure 2.5: Scheme of the different components of our image rotator, drawn in the xz plane (see Fig 2.1). Light enters with an in-plane linear polarization. The rotatable part (drawn here in the $\phi = 0$ situation) can be rotated as a whole around the indicated axis, and it is responsible for an image reflection $M(\phi)$ as defined in Fig. 2.2. The polarizer selects the in-plane polarization.

fabrication of the SPP can be found in Subsection 2.4.2. The apertures (in geometry A) and the position of the objectives (in geometries B and C) define the signal and idler path. The beam splitter is positioned on the crossing of the signal and idler path and is angle tuned such that the detection apertures obey mirror symmetry with respect to the beam splitter plane. The signal and idler arm of the interferometer each have a length of 1.6 m. The direction of the pump beam is centered in between the directions of the signal and idler path. The idler arm contains a delay line with which the length of the arm, and hence the relative arrival times of the photons at the beam splitter, can be adjusted.

The microscope objectives in detection geometry B are Leica 10x/0.25 infinity-corrected objectives with an effective focal length of 20 mm. They are positioned at 0.6 m from the beam splitter and image the tip of the single-mode fiber (Thorlabs SM800-5.6-125) onto the BBO crystal. The radius (at e^{-2} of maximum irradiance) of this image of the detected mode on the BBO crystal is measured to be 280 μm. We use slightly different optics in detection geometry C, in order to obtain a narrower waist of the detected mode on the BBO crystal. The radius (at e^{-2} of maximum irradiance) of the detected $l = 0$ mode, i.e. whenever the SPP is temporally removed from the apparatus, on the BBO crystal is now 220 μm. The radius of the characteristic ring of the detected $l = 1$ mode, i.e. whenever the SPP is in the apparatus, is 180 μm. This value is somewhat larger than the value of $\frac{1}{2}\sqrt{2} \times 220\ \mu\text{m} = 156\ \mu\text{m}$ expected for the $(l = 1, p = 0)$ mode due to the presence of higher order p modes.

The image rotator includes five optical components as shown in Fig. 2.5. The rotatable part is responsible for an image reflection $M(\phi)$ in a line making an angle ϕ with the y axis (see Fig. 2.2). It consists of three discrete mirrors instead of a commercial available glass Dove prism, in order to avoid any detrimental effects of wavelength dispersion. We are able to align the rotatable part within ± 0.2 mrad in the far field and ± 0.5 mm in the near field, measured over a full rotation. The fixed mirror on the left causes an image reflection $M(0)$ so that the combined action of the unit is a rotation $R(\theta) = R(2\phi) = M(\phi)M(0)$.

Although an image rotation is generally accompanied by a polarization rotation [86], our rotator transfers at most only 8% of the power into the orthogonal polarization. This convenient property is obtained by using silver mirrors (protected by a thin SiO_2 cover layer) instead of dielectric mirrors. The measured phase difference between the (three-fold) reflected s- and p-polarized light is $\phi_{s-p} = 0.81\pi$, which is sufficiently close to the ideal value of $\phi_{s-p} = \pi$ needed for a polarization-insensitive rotator*. As both polarization components have the same spatial profile, we simply remove this small unwanted orthogonal component with a fixed polarizer (see Fig. 2.5).

2.4.2 Spiral phase plate

A spiral phase plate (SPP) is a transparent plate whose thickness increases proportional to the azimuthal angle [87]. It imposes an azimuth-dependent optical retardation on the optical field. Our SPP is custom made by Philips Research Laboratories with dimensions suited for our application; the imposed optical retardation over a full rotation equals one optical cycle of the 826.2 nm SPDC light. The SPP operates as a lowering operator on l-numbers of the incoming modes at this wavelength. In detection geometry C, a single-mode fiber is used to detect solely the fundamental Gaussian mode ($l = 0$) behind the SPP which implies that it solely detects an $l = 1$ mode in front of the SPP.

The SPP is manufactured using photo replication technology [88]. To this end a high accuracy brass mould, the negative of the SPP we wish to produce, is machined using a programmable computer driven diamond tool. A transparent copy of the mould is obtained by using a reactive monomer encapsulated between the mould and a cover glass plate. The final SPP is obtained after polymerization of the monomer by UV radiation. The demand for an optical retardation of 826 nm in one cycle requires proper definition of step height and refractive index. We use a step height of 1.66 μm and a refractive index of 1.50. Some technical details on the production process are as follows: We use an adhesion promoter γ-(methacryloyloxypropyl)trimethoxysilane to allow for a firm coupling between the resulting polymer and the cover. We use a mixture of poly(ethyleneglycol) dimethacrylate with a refractive index of 1.48 and Ebecryl 604 (75% epoxyacrylate in hexanedioldiacrylate, a product of UCB chemicals) with a refractive index of 1.54 in a ratio of 2 : 1 to obtain an effective index of 1.50. To enable the photopolymer-

* A precise quantitative check of this value based upon the optical constants of silver is hampered by the fact that we do not know the precise thickness and porosity of the protective SiO_2 coating.

ization reaction 2% of a mixture of photoinitiators (Irgacure 651 and Irgacure 184) was added.

2.4.3 Alignment

We will discuss the alignment procedure in more detail because we think it can be helpful for anyone who wants to reproduce the experiment. We consider the position of the beam splitter as well as the position of the pump spot on the BBO crystal as fixed. Leaving out the rotator from the discussion we need to deal with the following degrees of freedom: angle of the pump beam θ_p and the angle of the beam splitter $\theta_{\rm bs}$. In detection geometry A, we additionally need to consider the position of the apertures. In detection geometries B and C, we additionally need to consider the positions of the objectives as well as the positions of the fibers (determining the position and angle of the detected mode on the crystal), assuming that the SPP is positioned correctly in geometry C. The correct alignment of θ_p and $\theta_{\rm bs}$ are independent of the choice of detection geometry. Therefore, we are allowed to switch to another detection geometry halfway the alignment procedure.

We start the alignment procedure by aligning the angle of the beam splitter in detection geometry B. We do this by firstly moving the fiber in the transverse plane in order to maximize the single count rate of each fiber for the corresponding transmission channel only. Secondly, we tune $\theta_{\rm bs}$ to maximize the single count rates of the reflection channels. The accuracy of this alignment step is $\Delta\theta_{\rm bs} = \pm 70\ \mu$rad. The correct alignment of the angle of the beam splitter depends on the position of the pump spot on the BBO as well as the alignment of the optics in the interferometer arms. From now on we do not change either of these.

The next goal is to align the angle of the pump beam. We control θ_p with a mirror that is positioned very close to the BBO crystal. Changing the angle of the pump beam with this mirror has a negligible effect on the position of the pump beam on the BBO crystal. The angle of the pump beam must become centered in between the detected directions in the signal and idler arm. We do this by maximizing the coincidence count rate $R_{\rm cc,ref}$ far away from HOM interference. Note that one may only perform this operation if the apertures/objectives are positioned correctly, obeying mirror symmetry with respect to the beam splitter plane. This positioning of apertures (detection geometry A) or fiber-detectors detectors (detection geometry B and C) is done by eye, using a visible HeNe-laser.

To measure the correct visibility in detection geometry A with a large aperture diameter, an even higher precision of the alignment of the angle of the beam splitter is required ($\Delta\theta_{\rm bs} = \pm 40\ \mu$rad set by the diffraction limit). We improve the alignment by simply minimizing the coincidence count rate inside the HOM dip in detection geometry A. One may only apply this alignment technique if all the other components are aligned correctly, for minimizing the coincidence count rate can sometimes also be achieved by misaligning any other component in the setup.

The alignment of the fiber-detector in detection geometry C deserves some extra attention. The problem is that placing the spiral phase plate (SPP) in front of the single-mode fiber will slightly shift the central position of the detected mode on the BBO crystal (~ 1 mm) due to a small wedge in the SPP. As a consequence, one has to reposition the fiber with respect to the microscope objective in order to get the position of the detected mode centered at the pump beam again. From experimental experience we know that the shape of $R_{\rm cc}(\tau)$, and hence also the visibility, is extremely sensitive to the position of the projection of the detected $l = 1$ mode on the BBO crystal. A transverse shift of only 25 μm on the BBO can lead to a decrease of the HOM visibility of 9 percent points in the case of an image rotation of $\theta = 90°$. This means that an alignment precision below $\Delta\theta_{\rm det} < 10$ μrad is required. We achieve this accuracy by imaging the projection of the detected $l = 1$ mode on the BBO crystal onto a CCD camera.

We want to stress that fine tuning the position fiber in detection geometry C by optimizing two-photon interference effects (i.e. maximizing the absolute visibility) may result in an incorrectly aligned system. Figure 2.10 shows two results which are obtained with an incorrectly positioned projection of the detected $l = 1$ mode on the BBO crystal. The figure makes clear that an incorrectly aligned system may give an absolute visibility that is even higher than the visibility that would have been obtained with a correctly aligned system.

2.4.4 Experimental results for detection through circular apertures

We have measured the two-photon bunching visibility as a function of image rotation with the setup shown in Fig. 2.4. In this subsection we present the results obtained in detection geometry A (detection through circular apertures) and in detection geometry B (detection of solely the fundamental Gaussian mode). We compare these measurements with the theoretical predictions and we determine the azimuthal Schmidt number $K_{\rm az}$, which is the effective dimensionality of the entanglement in orbital angular momentum.

The effect of an image rotation on the two-photon bunching visibility is clearly illustrated in Fig. 2.6. The figure shows measurements of the coincidence count rate as a function time delay for two different rotation angles $\theta = 0°$ and $\theta = 20°$ in detection geometry A (aperture diameter of 10 mm). Both cases exhibit a drop of the coincidence count rate near $\tau = 0$ reaching almost ideal photon bunching ($V = 92\%$) in the non-rotated case. The dip in the case of $\theta = 20°$ on the other hand, has a strongly reduced visibility of only 36%.

The two visibilities extracted from Fig. 2.6 correspond to two points in Fig. 2.7. In this figure we have plotted the bunching visibility $V(\theta)$ as a function of the

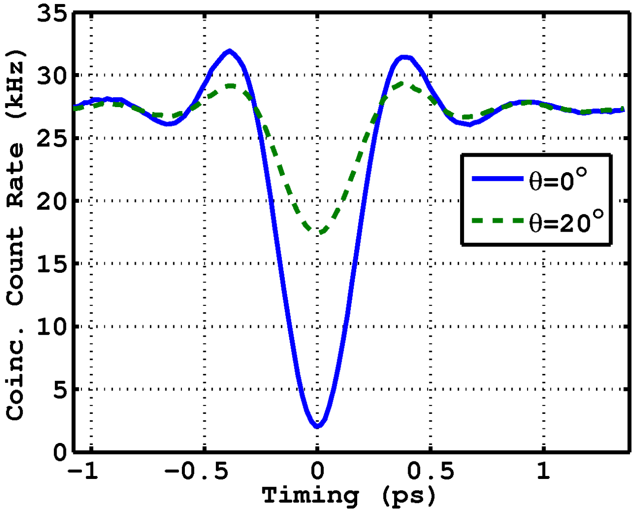

Figure 2.6: Two-photon coincidence count rate versus the time delay τ for two different rotation angles. The measurements are performed in detection geometry A (see Fig. 2.4) where one aperture has a diameter of 10 mm *and the other aperture is open. The two-photon bunching visibilities are* 92% *and* 36% *for* $\theta = 0^\circ$ *and* $\theta = 20^\circ$*, respectively.*

rotation angle for various aperture diameters (detection geometry A) and for two fiber-coupled detectors (detection geometry B). As expected, we observe almost ideal photon bunching for all detection geometries as long as we apply no image rotation. If we apply a certain image rotation, however, the two-photon bunching visibility becomes different for different detection geometries. The measurement with fiber-coupled detectors serves as a reference measurement, demonstrating that the bunching visibility of the rotational symmetric fundamental Gaussian mode is independent of the angle of rotation (remaining $V > 98.7\%$). Our measurements in detection geometry A show that a larger aperture corresponds to a narrower peak of $V(\theta)$ around $\theta = 0$. This is in agreement with our expectations based on the calculation of the continuous two-photon amplitude [Eq. (2.11)]. The figure shows theoretical curves of $V(\theta)$ for aperture diameters of 1 mm, 4 mm, and 10 mm. The latter two are in good agreement with the measurements, but the 1 mm case shows a slight deviation which we believe is the result of imperfect alignment.

Apart from the three cases mentioned above, where the second aperture is set completely open, we have also measured $V(\theta)$ in the case where *both* apertures are set to a diameter of 4 mm (see Fig. 2.7). Closing the second aperture to the size of the first one slightly broadens the $V(\theta)$ curve. The detection of one photon within an aperture minimizes the position uncertainty of the other (brother) photon to

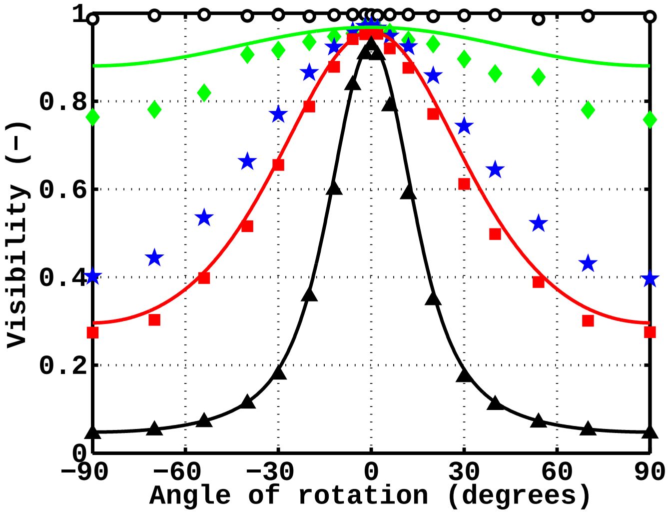

Figure 2.7: Measured two-photon bunching visibility versus angle of rotation for various detection geometries (see Fig. 2.4): two single-mode fibers (circles), 1 mm*-open apertures (diamonds),* 4 mm-4 mm *apertures (stars),* 4 mm*-open apertures (squares) and* 10 mm*-open apertures (triangles). The three solid curves are predicted by theory [Eq. (2.11)] and correspond from top till bottom to the measurements of the diamonds, the squares, and the triangles, respectively.*

twice the width of the pump beam in the detection plane [see Eq. (2.3)]. The fact that the position of the second photon is still not completely fixed after detection of the first one explains why it matters whether or not an identical aperture in front of the second detector is present. Closing the second aperture to the same size indeed also reduces the reference coincidence rate $R_{\rm cc}(\infty)$. We have not plotted the corresponding theoretical curve in Fig. 2.7 simply because we have no analytic expression for $V(\theta)$ in a detection geometry with two equally closed apertures.

Now what do the measurements in Fig. 2.7 tell us about the generated two-photon state? From symmetry arguments (Gaussian pump beam, paraxial angle of the SPDC cone, and circular detection apertures) we know that we can write the detected part of the generated two-photon state in the form of Eq. (2.20). By applying a cosine transform on the measured curve $V(\theta)$ we find *all* the orbital angular momentum (OAM) probability coefficients P_l conform Eq. (2.23). This means that a measurement of $V(\theta)$ provides a *complete* characterization of the high dimensional entanglement that exists between the orbital angular momenta of the two photons.

We have performed such modal decompositions on our measured curves $V(\theta)$.

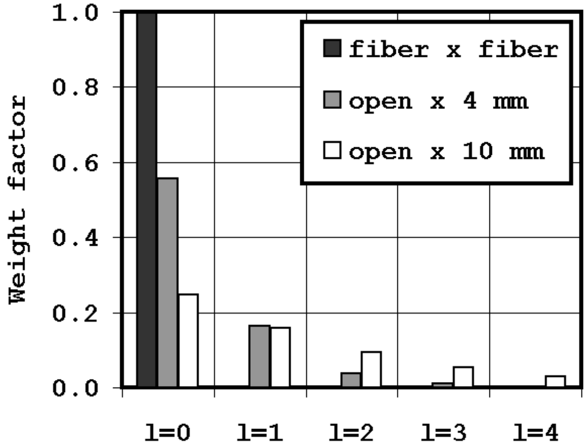

Figure 2.8: Measured weight factors P_l of the orbital angular momentum terms in the entangled two-photon state for the three specified detection geometries. Not shown are the weight factors for $l > 4$ and negative l, for which $P_{-l} = P_l$.

Detector 1	Detector 2	K_{az}
SM-fiber	SM-fiber	1.01 ± 0.01
1 mm	open	1.26 ± 0.06
4 mm	4 mm	2.08 ± 0.08
4 mm	open	2.7 ± 0.1
10 mm	open	7.3 ± 0.3

Table 2.1: Measured azimuthal Schmidt number (K_{az}) of the detected two-photon state for various detection geometries (see Fig 2.4). The first row is measured in detection geometry B; the other four rows are measured in detection geometry A, for which the aperture diameters are specified.

The resulting coefficients P_l for three (of five) detection geometries are shown in Fig. 2.8. It is clearly visible that the contributions of the smallest l numbers become more dominant if the detection apertures become narrower. The measurement with single mode fibers (detection geometry B) serves as a reference, and shows that the detected two-photon state contains only photons with zero orbital angular momentum, i.e., with $l = 0$. From the measured values of P_l we calculate the azimuthal Schmidt number [using Eq. (2.24)], which is the effective number of modes that participate in the entanglement. The values are listed in Table 2.1. For detection through single-mode fibers (detection geometry B) we find $K_{\mathrm{az}} = 1.01 \pm 0.01$ and in detection geometry A the azimuthal Schmidt number ranges between 1.26 ± 0.06 and 7.3 ± 0.3 depending on the aperture diameter.

2.4.5 Experimental results for $l = 1$ detection

In this subsection we present the measurements that we have performed in detection geometry C, where one of the detectors is coupled to a single-mode $l = 1$ selector (see Fig. 2.4). Again, we have measured the coincidence count rate $R_{\mathrm{cc}}(\tau)$ as a function of delay time. The results for various angles of rotation are presented in Fig. 2.9. As expected from Eq. (2.23) we observe photon bunching in the case of no image rotation and photon anti-bunching if a rotation of $\theta = 90°$ is applied.

For angles between $0 < \theta < 90°$ we observe an asymmetric curve for $R_{\mathrm{cc}}(\tau)$. This phenomenon can be fully explained from the spectral shape of the color filters. The theoretical shape of $R_{\mathrm{cc}}(\theta, \tau)$ is given by Eq. (2.25) from which we conclude that $R_{\mathrm{cc}}(\tau)$ will have an anti-symmetric component only if the filters are not exactly identical, making $T_{\mathrm{tot}}(\omega)$ asymmetric, and if $\sin(2\theta) \neq 0$. We had intended to use identical filters; however, due to the limited fabrication accuracy, the transmission spectra of the two filters were slightly different. One of the filters has a transmission spectrum that is centered around $\lambda = 824.7$ nm instead of $\lambda = 826.2$ nm, whereas the other filter is neatly centered around $\lambda = 826.2$ nm. This difference is responsible for the anti-symmetric component in $R_{\mathrm{cc}}(\tau)$ in Fig. 2.9.

The dotted curve shows the calculated coincidence count rate for $\theta = 45°$ as expected from Eq. (2.25) using measured spectral transmission functions of the filters. The strength of the contribution of the asymmetric component in $R_{\mathrm{cc}}(\tau)$ is in excellent agreement with our measurements of the spectra. Serving as an extra check of Eq. (2.25), we have also exchanged the two filters and observe, as expected, an asymmetry of $R_{\mathrm{cc}}(\tau)$ that is flipped around the vertical $\tau = 0$ axis.

From the measured curves of $R_{\mathrm{cc}}(\tau)$ for various angles of rotations, we have extracted the two-photon bunching visibility defined in Eq. (2.6). According to this definition, $V(\theta)$ depends only on the symmetric component of $R_{\mathrm{cc}}(\tau)$ and hence Eq. (2.23) is fully applicable to the outcome of our measurement of $V(\theta)$. The re-

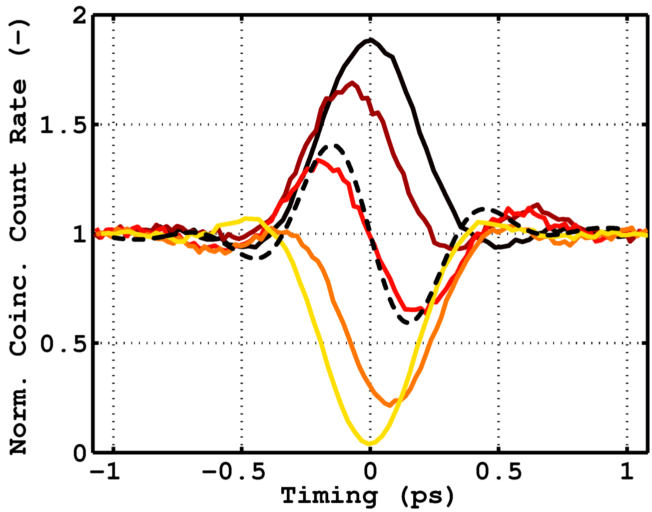

Figure 2.9: Coincidence count rate versus time delay τ, measured in a single-mode $l = 1$ detection geometry, for various angles of rotation θ. The five solid curves (from top till bottom) are measured at $\theta = 90^{\circ}$, 67.5°, 45°, 22.5°, and 0°, respectively. The dotted curve is calculated for $\theta = 45^{\circ}$, making use of Eq. (2.25) and the measured spectral transmissions of the bandpass filters.

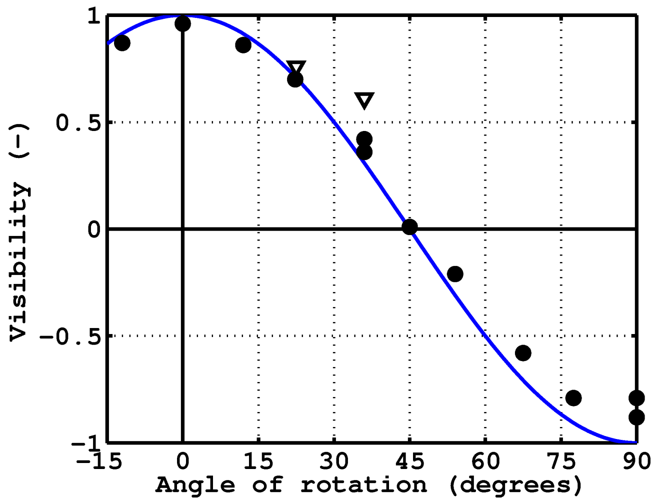

Figure 2.10: Two-photon bunching visibility versus angle of rotation (circles), where only a single mode with orbital angular momentum $l = 1$ is detected. The triangles are two results obtained with an experimental apparatus that is improperly aligned (see Subsection 2.4.3). The uncertainty of the measured visibility is ± 0.05. The solid curve is predicted by theory [Eq. (2.23) with $P_{-1} = P_1 = \frac{1}{2}$ and al other P_l coefficients zero].

sulting values are presented in Fig. 2.10 and are very well described by the predicted $V(\theta) = \cos(2\theta)$.

As shown in Fig. 2.10, we have performed several measurements of $V(\theta)$ twice and observed a small spread which, we believe, is caused by the limited achievable accuracy of the alignment. This limited accuracy of the alignment is the dominant contribution to the uncertainty of ± 0.05 in the measurements of $V(\theta)$. We furthermore observe that the two-photon bunching visibility at $\theta = 90°$ is only $-82 \pm 5\%$ in stead of the predicted -100%. This may be explained by the observation that our detected $l = 1$ mode (detection geometry C) is not perfectly rotational symmetric for yet unknown reasons.

2.5 Concluding discussion

In conclusion, we have presented and demonstrated a new method to obtain a complete characterization of the high-dimensional entanglement in orbital angular momentum (OAM) of down-converted photon pairs. The method is based on measurements of the interference in a two-photon interferometer (Hong-Ou-Mandel-type) with an odd number of mirrors and a built-in image rotator. We have theoretically analyzed this method for the case of a rotationally symmetric (Gaussian) pump profile and coincidence detection behind circular apertures, using two different approaches. In the first approach, we derive analytic expressions for the two-photon (bunching) visibility $V(\theta)$ as a function of the rotation angle θ, by spatial integration of the interference in the continuous two-photon amplitude. In the second approach, we use a modal (Schmidt) decomposition of the detected two-photon amplitude to derive a natural Fourier relation between $V(\theta)$ and the weight factors P_l of the OAM terms in the entangled two-photon state: high OAM states result in fast changes of $V(\theta)$ with angle, whereas low OAM states produce slower changes. These weight factors are then combined to an azimuthal Schmidt number K_{az}, which quantifies the effective dimensionality of the OAM entanglement. Both approaches can easily be generalized to pump profiles with an orbital angular momentum different from $l = 0$.

We have shown that the experimental results are in close agreement with the theoretical predictions. More specifically, an increase in the size of the detection aperture results in an increase in the effective dimensionality K_{az}, which is visible as a reduction in the angular width of $V(\theta)$ around $V(0) \approx 1$. We have tuned the effective dimensionality between $K_{\text{az}} = 1.01 \pm 0.01$ and $K_{\text{az}} = 7.3 \pm 0.3$. Using a single-mode OAM-selective ($l = 1$) detector, we have isolated one term in the Fourier expansion and demonstrated a controllable change from photon bunching to photon antibunching. At intermediate settings we have observed highly asymmetric HOM dips $V(\tau)$ versus time delay τ. We attribute this asymmetry to a difference between the two spectral filters in front of the detectors.

The Klyshko picture provides for a simple intuitive way to understand the working principle of our OAM analysis method. The Klyshko approach is based on a time-reversal of the path of one of the photons. The full path now runs (backwards in time) from one detector back to the generating crystal and after reflection (forward in time) to the second detector. In the Klyshko picture, the two-photon visibility results from the interference between the clockwise and counter-clockwise paths, which are associated with the doubly reflected and doubly transmitted paths at the beam splitter. Only if the total number of mirrors in the interferometer is odd, will these two paths acquire an opposite image rotation, which in turn leads to a reduction of the two-photon visibility. For an even number of mirror the image rotation is identical for both paths.

One might wonder why our experimental results are limited to $K_{\mathrm{az}} \leq 7.3 \pm 0.3$. The prime reason is the limited size of our pump spot. The simplest way to increase the Schmidt numbers K_{az} and K_{2D} would therefore be an increase of the pump spot from its present diameter of 270 μm to a larger value. A complication one might, however, run into is the combined spectral and spatial labeling discussed in Ref. [79]. This labeling can be diminished by either reducing the detection bandwidth or the angle between the signal and idler beam. An alternative method to increase the Schmidt numbers is via an increase of the opening angle of the detection system. However, with the current setup we are already close to the boundary set by the thin-crystal limit.

A logical question for future research is if and how our method can be extended to an analysis of the full spatial entanglement, comprising both the azimuthal and the radial components. Recent experiments have shown how the 1D Schmidt number can be determined by measuring the two-photon visibility as a function of the transverse displacement of one beam with respect to the other [79]. It would be interesting to investigate whether a combination of a 1D translation and an image rotation will be sufficient to obtain enough information for a characterization of the full 2D spatial entanglement.

2.6 Acknowledgements

This work has been supported by the Stichting voor Fundamenteel Onderzoek der Materie. We thank S. Verstoep and P. Ruijgrok for assistance with the experiment.

3

Optical characterization of periodically poled crystals

We demonstrate how the Maker fringes that are observable in spontaneous parametric down-conversion (SPDC) give a direct visualization of the poling quality of a periodically poled crystal. Identical Maker fringes are observed in the optical spectrum of collinear SPDC and the temperature dependence of second harmonic generation. We analyze these Maker fringes via a unified treatment of the tuning curve in crystals with small and slowly varying deformations of the poling structure. Our theoretical model, based on a Fourier analysis of the poling deformations, distinguishes between duty-cycle variations and variations of the poling phase. The analysis indicates that the poling phase is approximately fixed, while the duty-cycle typically varies between 36% and 64%.

W. H. Peeters and M. P. van Exter, *Optical characterization of periodically poled* $KTiPO_4$, Optics Express **16**, 7344 (2008)

3.1 Introduction

Phase matching is required for an efficient operation of second-order nonlinear optical processes such as second harmonic generation (SHG) and spontaneous parametric down-conversion (SPDC). In uniform crystals, phase matching is achieved by utilizing the modal dispersion resulting from the crystal's birefringence. Another method called quasi phase matching (QPM) relies on the fabrication of a ferroelectric domain structure with periodically inverting polarization. QPM allows for a larger choice of optical frequencies and allows access to more, and potentially larger, elements of the nonlinear $\chi^{(2)}$ tensor. An extensive discussion on the tuning and tolerances of QPM can be found in an article of Fejer *et al.* [89]. Different poling techniques are discussed in Refs. [90, 91].

The quality of the fabricated poling structure is generally characterized via imaging of the domain boundaries at the crystal surface. Important techniques comprise surface-charge selective etching [92], electrostatic force microscopy [93], secondary-electron microscopy [94], and piezoresponse-assisted atomic force microscopy [95]. Another way to characterize the poling quality is by studying the phase-matching conditions of a second-order nonlinear process like SHG or SPDC. Common techniques in this category use the wavelength dependence of the conversion efficiency of SHG [96,97]. A three-dimensional characterization of the poling duty-cycle has been demonstrated using ultrashort pulses and SGH [98]. A third technique characterizes the crystal structure by mapping the angle-frequency distribution of radiation that is generated via SPDC [99].

In this chapter we present high quality measurements and a detailed analysis of the ring-shaped angular SPDC pattern, generated in a periodically poled $KTiOPO_4$ crystal (PPKTP). Our analysis is very different from earlier results presented by Kitaeva *et al.* [99], as these authors analyze the large scale angle-frequency distribution of the SPDC pattern, whereas we concentrate on the fine structure close to phase matching. We also demonstrate that the same fringe pattern is present in the optical spectrum in collinear SPDC and the temperature dependence of SHG. We denote the observed patterns as Maker fringes, as the typical sinc-type intensity dependence was first discussed by Maker et al. [100]. We perform a meticulous comparison between the measurements and our theoretical predictions of the fringe shape, hereby using up to date knowledge of KTP's material properties. Finally, we analyze the observed fringe patterns in terms of small and slowly varying deformations of the periodic poling structure.

The paper is organized as follows. Section 3.2 gives a theoretical description of the temperature, angle, and wavelength dependence of the phase-matching condition in periodically poled crystals. Section 3.3 describes the three experimental setups that are used for (A) the measurement of the angular SPDC pattern, (B) the spectrum of SPDC light, and (C) the temperature dependent conversion efficiency in SHG. Sections 3.4.1, 3.4.2, and 3.4.3 discuss the Maker fringes that are experimentally obtained via the three above-mentioned methods. In Sec. 3.5, we analyze the observed deviations from the ideal sinc-shaped Maker fringes in terms of small and slowly varying deformations of the poling structure. We hereby use a theoretical treatment, given in Sec. 3.5.1, that is based on a Fourier analysis of small and slowly varying deformations of the poling structure.

3.2 Phase matching in a periodically poled crystal

We consider the nonlinear processes of second harmonic generation (SHG) and spontaneous parametric down-conversion (SPDC) in a periodically poled crystal. For both processes, we assume loosely focussed cw-pumping (Rayleigh range pump $\gg$ crystal length) in the low conversion efficiency limit. The crystal is periodically poled along its crystallographic z axis in domains perpendicular to the crystallographic x axis. The pump beam is z polarized and propagates along the x axis. We consider the crystal to be infinite in the transverse directions. In the SHG configuration, we pump the crystal at angular frequency ω so that the up-converted wave has angular frequency 2ω. In the SPDC configuration, we pump the crystal at 2ω so that the angular frequencies of the down-converted signal and idler waves can be written as $\omega_s = \omega + \Omega/2$ and $\omega_i = \omega - \Omega/2$.

The SPDC process can be seen as the inverse process of SHG, when considering the same spatial and spectral modes. The conversion efficiencies of both processes (per spatial and spectral mode) are thus described by the same tuning curve, which is the conversion efficiency as a function of wave vector mismatch Δk along the x direction of the crystal. The tuning curve depends on the precise position-dependent nonlinear coefficient $d(x)$. More specifically, the conversion efficiency as a function of Δk is proportional to the absolute value squared of the Fourier transform of $d(x)$ [89].

An ideal periodically poled crystal has a square-wave-shaped nonlinear coefficient $d(x)$ with amplitude $\pm d_{\text{eff}}$, where the effective nonlinearity d_{eff} is a fixed material property. The Fourier transform of a square-wave-shaped $d(x)$ contains odd-m harmonics of the form $k_m^{\pm} = \pm 2\pi m/\Lambda_0$, where Λ_0 is the poling period of the crystal. Hence, the conversion efficiency will become peaked around any wave vector mismatch $\Delta k = k_m^{\pm}$. The mismatch parameter ϕ_m, defined as the accumulated phase mismatch over half the crystal length with respect to quasi-phase-matching order m, is

$$\phi_m = \frac{L_0}{2}\left[\left|\Delta k\right| f(T) - \frac{2\pi m}{\Lambda_0}\right], \tag{3.1}$$

where the crystal length L_0 and the poling period Λ_0 are specified at a certain reference temperature T_0. The function $f(T)$ is the temperature-dependent material expansion factor which is defined to equal unity at the reference temperature. The conversion efficiency in the neighborhood of some m-order quasi phase match condition now becomes [89]

$$\eta_m(\phi_m) \propto \left(\frac{2}{\pi m}\right)^2 \operatorname{sinc}^2(\phi_m), \tag{3.2}$$

where the prefactor denotes the relative conversion efficiency, compared to the hypothetical case of a perfectly phase matched uniform crystal with an identical effective nonlinearity. The sinc function in Eq. (3.2) results from the Fourier transform of the hat-shaped crystal outline. In this chapter, we will restrict our analysis to quasi-phase-matching order $m = 1$, and we will drop the subscripts of ϕ_m and η_m. In accordance with Ref. [89] we normalize $\hat{\eta}(\phi)$ to its peak value via $\hat{\eta}(\phi) = \eta(\phi)/\eta(\phi = 0)$.

In order to calculate the mismatch parameter ϕ from Eq. (3.1), we must calculate the wave vector mismatch Δk along the x direction. The wave vector mismatch is defined as the wave vector of the 'blue' photon minus the wave vectors of the two 'red' photons. For the SHG configuration, this wave vector mismatch becomes

$$\Delta k_{\mathrm{SHG}} = k(2\omega, T) - 2k(\omega, T), \tag{3.3}$$

where $k(\omega, T)$ is the temperature-dependent dispersion relation of z polarized light in the crystal. Eq. (3.3) shows that the wave vector mismatch in SHG can be tuned in two different ways: via wavelength tuning and via temperature tuning. The wavelength and temperature dependence are often separated via

$$\begin{aligned} \Delta k_{\mathrm{SHG}} \quad = \quad & k(2\omega, T_0) - 2k(\omega, T_0) \\ & + \frac{2\omega}{c}\big[\Delta n_z(2\omega, T) - \Delta n_z(\omega, T)\big], \end{aligned} \tag{3.4}$$

where $\Delta n_z(\omega, T) \equiv n_z(\omega, T) - n_z(\omega, T_0)$ is a shorthand notation for the change in refractive index caused by a deviation from the reference temperature $T_0 = 25$ °C [101, 102].

The SPDC configuration differs from the SHG configuration in two ways. First of all, the signal and idler wave may have components in transverse directions. Secondly, any frequency difference $\Omega \equiv \omega_s - \omega_i$ between the signal and idler photon is allowed. Therefore, the wave vector mismatch in SPDC can be tuned in not just two, but four different ways: via wavelength tuning, via temperature tuning, via tuning of the detection angle, and via tuning of the detection wavelength. The wave vector mismatch in the SPDC configuration can be written as

$$\Delta k_{\mathrm{SPDC}} = k(2\omega, T) - [k_{s,x} + k_{i,x}], \tag{3.5}$$

where $k_{s,x}$ and $k_{i,x}$ are the x components of the wave vectors of the signal and idler waves in the crystal, respectively. Explicitly writing out the angle detuning and frequency detuning in the small angle and small frequency-detuning limit, yields

$$\begin{aligned} \Delta k_{\mathrm{SPDC}} &= k(2\omega, T) - 2k(\omega, T) \\ &\quad + k(\omega, T)\left[\theta_y^2 + \left(\frac{n_z}{n_x}\right)^2 \theta_z^2\right] \\ &\quad - \left.\frac{\partial^2 k}{\partial \omega^2}\right|_{\omega,T} \left(\frac{\Omega}{2}\right)^2, \end{aligned} \tag{3.6}$$

where $\boldsymbol{\theta} = (\theta_y, \theta_z)$ is the emission angle inside the crystal, and n_z and n_x are shorthand notations for the refractive index of z and x polarized light, respectively. The n_z/n_x factor in front of θ_z originates from the fact that down-converted light with a certain transverse k_z component carries a polarization with a small x component too. The angle dependence of the refractive index is found by using the index ellipsoid for our polarization. The latter term in Eq. (3.6) is obtained by performing a Taylor expansion around zero frequency detuning.

Throughout the article we will regularly use Eqs. (3.1)-(3.6) to compare our experimental results with existing literature on KTP's material properties. These properties involve Sellmeier dispersion equations [103–107], temperature dependence of the refractive index [101, 107, 108], and thermal expansion coefficients [101,102]. We will use the most recent and mutually most compatible literature values: the z component of the refractive index from Ref. [106], the x and y component of the refractive index from Ref. [107], the temperature dependence of the refractive index from Ref. [101], and the thermal expansion coefficients from Ref. [102].

3.3 Experimental apparatuses

Figure 3.1 shows the three experimental setups that we used for the characterization of the poling quality, either via SPDC [Figs. 3.1(a) and 3.1(b)] or SHG [Fig. 3.1(c)]. In this section we will give the experimental details of these three setups.

The pump part of the SPDC setups in Fig. 3.1(a) and Fig. 3.1(b) are identical. A cw krypton-ion laser (Coherent Innova 300) emits 220 mW at a vacuum wavelength of 413.1 nm in a TEM_{00} mode. This pump beam is mildly focussed ($w_0 = 190$ μm is the radius at e^{-2} of maximum irradiance) into a PPKTP crystal. The crystal is manufactured by Raicol Crystals Ltd. with low temperature periodic electrical poling, based on the application of a pulsed electric switching field to a patterned electrode [109]. The crystal has a length of 5.09 mm in the x direction, a thickness of 1 mm in the z direction and a width of 2 mm in the y direction. The pump beam propagates along the crystallographic x axis and is z polarized, allowing us to use

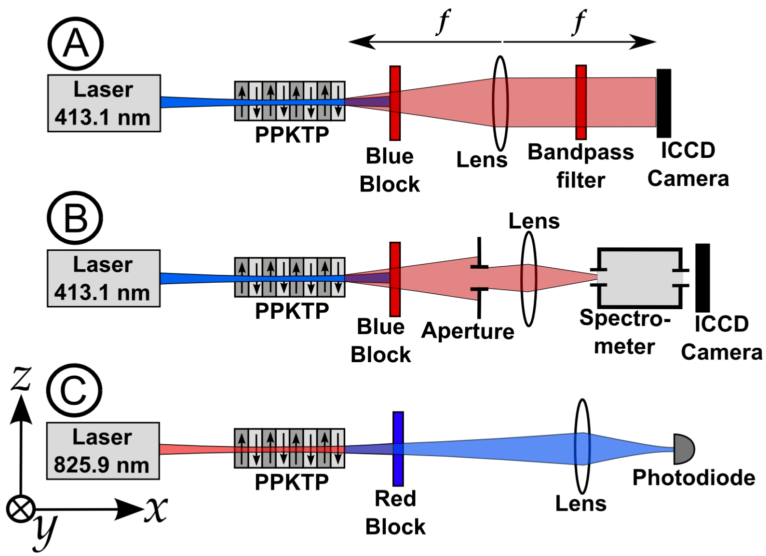

Figure 3.1: Three different experimental setups that are used to measure Maker fringes of a periodically poled $KTiOPO_4$ crystal (PPKTP). Setup A and B utilize the nonlinear processes of spontaneous parametric down-conversion, while setup C uses second harmonic generation. The indicated coordinate system corresponds to the crystallographic axes of the PPKTP crystal. Setup A: The far field of a narrow spectral band of the down-converted light is projected onto an intensified CCD camera (ICCD). Setup B: The spectral decomposition within a small angle (selected by the aperture) of the down-converted light is measured by placing an ICCD camera behind a spectrometer. Setup C: The power of the up-converted light is measured with a photodiode, while the crystal temperature is varied.

the large nonlinear d_{33} coefficient of KTP. The pump beam is centered on the crystal facets. The poling period of the crystal is specified to be $\Lambda_0 = 3.675$ μm which is designed for first-order quasi phase matching at 413.1 nm $\leftrightarrow$ 826.2 nm. The crystal is thermally contacted along the full crystal length to a bulky Aluminum mount via a 100 μm thick Indium layer. The temperature is stabilized to $\Delta T < 0.1$ °C using a Dale 1T1002-5 thermistor, an ILX-Lightwave LDT5910 controller and a Peltier element. The thermometer system is calibrated to an accuracy of $\pm(0.5\% + 0.2$ °C) by using a commercial ATAL RTD407907 thermometer. Phase matching in forward direction is achieved at a temperature of 60.7 °C.

The detection part of Fig. 3.1(a) contains a lens with focal length of 10 cm in an f-f geometry to project the far field onto an intensified CCD camera (ICCD) of Princeton Instruments (I-MAX-512-T,18). A narrow-band color filter selects a $\Delta\lambda = 5$ nm band around $\lambda = 826$ nm. This bandwidth is much smaller than the full width of the main Maker fringe in the spectral domain (see Fig. 3.5). The bandpass filter removes all angle-frequency correlations from the down-converted light.

The detection part of Fig. 3.1(b) contains an aperture that is positioned at large distance ($\simeq 0.5$ m) in the far field of the sample. The aperture selects a cone-shaped solid angle of 42 mrad^2 in the forward direction. The selected solid angle is much smaller than the solid angle of the main central Maker fringe (≈ 300 mrad^2), so that all angle-frequency correlations are removed. The light is then focussed onto the input slit of a spectrometer (Jobin Yvon 320) and the output is projected on an ICCD camera of Princeton Instruments (I-MAX-512-T,18). The dispersion of the spectrometer is 570 μm per nanometer. The width of the ICCD chip is 12.8 mm which corresponds to a full spectral width of a single image of $\Delta\lambda = 22$ nm. The center of the detected wavelength interval can be adjusted with a knob on the spectrum analyzer. The spectral response of the ICCD camera and spectrometer was calibrated by using a white light source and a non-intensified CCD with a well-specified spectral response. The spectrometer's offset was calibrated by using the 826.45 nm line of Argon.

The SHG setup in Fig. 3.1(c) is straightforward. A cw Ti:sapphire laser (Coherent 899 Ring Laser) emits 270 mW at a vacuum wavelength of 825.9 nm in a TEM_{00} mode. The beam is mildly focussed into the center of the same PPKTP crystal. The Rayleigh range of the beam is (14 ± 2) mm corresponding to a beam radius at e^{-2} of maximum irradiance of $w_0 = (61 \pm 4)$ μm. The pump propagates along the x direction of the crystal and is z polarized. The PPKTP crystal, the crystal mount and the temperature control part are the same as in the SPDC setup. The intensity of the SHG light is measured with a photodiode (HUV1100BQ), a homemade amplifier, and a voltmeter.

We have experimentally compared the peak conversion efficiencies of the 5-mm-long PPKTP crystal and a 1-mm-long β-BaB_2O_4 crystal (BBO). The conversion efficiency for both SPDC and SHG is expected to be much higher for PPKTP than for BBO. At a cutting angle $\theta_c = 29.2°$, the effective nonlinearity of BBO in type-I phase matching is expected to be $d_{\text{eff}} = -d_{22}\cos\theta_c = 2.0$ pm/V, based on data from Ref. [110]. For PPKTP, the effective nonlinearity corrected for first-order quasi phase matching is expected to be $(2/\pi)d_{33} = 9.8$ pm/V, based on data from Ref. [111]. When comparing crystals of equal length, it is thus expected that PPKTP yields $(9.8/2)^2 = 24$ times higher conversion efficiencies than BBO. In our case, the PPKTP crystal is 5 times longer than the BBO crystal, so we expect a conversion that is $5^2 \times 24 = 600$ times more efficient. We observe that the SHG process is approximately 575 times more efficient than the BBO crystal. In the inverse process of SPDC we observe an enhancement factor of approximately 700. Both observations are in reasonable agreement with the expected enhancement factor of 600. We conclude that the quality of the periodically poled crystal must be very good with a duty-cycle close to 50%.

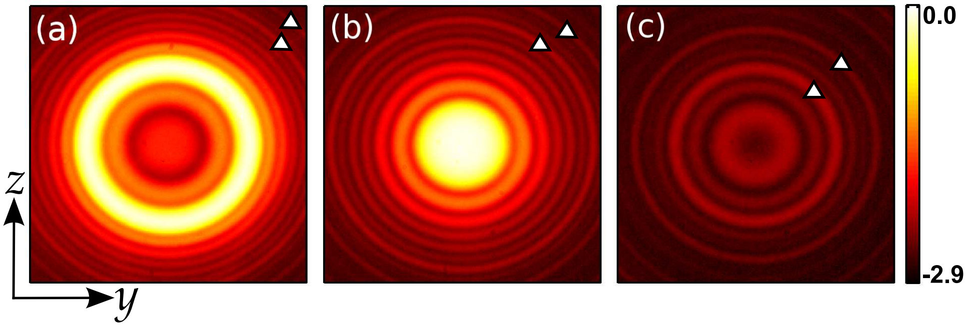

Figure 3.2: Measured angular intensity pattern of light generated via spontaneous parametric down-conversion in a 5-mm-*long periodically poled KTP crystal. The detection bandwidth is much smaller than the inverse angular dispersion of the Maker fringes. The color scale represents the logarithm (*$\log_{10}$*) of the intensity divided by the maximum intensity of the three images. The full width and full height of each image is* 96 mrad*. The three images are taken at different crystal temperatures: (a)* $53.5\ ^{\circ}\mathrm{C}$*, (b)* $60.7\ ^{\circ}\mathrm{C}$*, and (c)* $72.0\ ^{\circ}\mathrm{C}$*. Phase matching in forward direction is achieved in situation (b). The sixth and ninth fringe stand out and are marked with triangles in each image. The same PPKTP crystal is used in Figs. 3.4, 3.3, 3.5, and 3.6. The fringe patterns are slightly elliptical.*

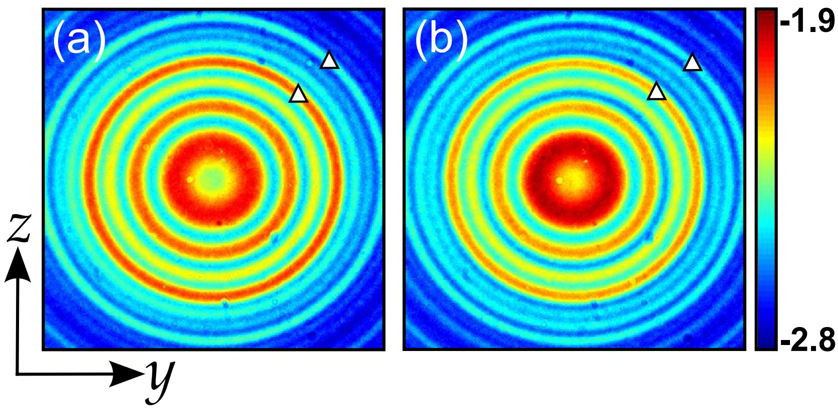

Figure 3.3: Measured SPDC ring pattern observed for pumping at two different positions on the crystal. The conditions are similar to those described in Fig. 3.2. The crystal temperature is now $69.7\ ^{\circ}\mathrm{C}$ *and the image size is* $90 \times 90\ \mathrm{mrad}^2$*. The pump positions on the crystal are separated by* 1.4 mm *in the* y *direction. The images are very much alike. For instance, the sixth and ninth fringe stand out and are marked with triangles in both images. Only minor differences are visible. The patterns do not change upon a pump displacement in the* z *direction. The same PPKTP crystal is used in Figs. 3.2, 3.4, 3.5, and 3.6.*

3.4 Experimental results

3.4.1 Maker fringes in angular intensity pattern of SPDC light

The angular intensity pattern of light generated via SPDC in a 5-mm-long periodically poled KTP crystal is measured with the setup in Fig. 3.1(a). The details of the experimental apparatus are given in Sec. 3.3. Three images, taken at three different temperatures are presented in Fig. 3.2. The images contain Maker fringes [100] caused by the angle dependence of the phase-matching condition [see Eq. (3.6)]. We observe continuous expansion of the fringe pattern upon reduction of temperature.

Several important aspects of the images will now be discussed. First of all, the spacing between the successive rings decreases at large angles in such a way that $I \propto \text{sinc}^2(A\Theta^2 + B)$, where Θ is the detection angle outside the crystal. The quadratic relation between detection angle and mismatch parameter is expected from Eqs. (3.6) and (3.1). Secondly, we observe that the ring pattern in Fig. 3.2 is slightly elliptical. This effect is due to a difference in the refractive index of z and x polarized light. Down-converted light with a certain k_z component has a polarization with a small x component, which causes the fringes to be elliptical [$n_z \neq n_x$ in Eq. (3.6)]. A third aspect concerns the peculiar deviations from the ideal sinc-like fringe structure. The sixth and ninth fringe, for example, are standing out with respect to neighboring fringes. These deviations are caused by small and slowly varying deformations of the poling structure. This experiment thus provides a simple and direct visualization of slowly varying deviations from perfect poling.

In order to quantify the ellipticity, we have performed some image processing. The image is first transformed from Cartesian coordinates to polar coordinates around the approximate center. Fourier analysis of this transformed image gives components of the form $f_l(r)\exp(il\varphi)$. The Fourier coefficients of this expansion depend strongly on the chosen position of the center. We have determined the optimal position of the center by minimizing the $l = 1$ coefficient. The ellipticity is now linked to the $l = 2$ coefficient of the Fourier expansion around this best center. We have accurately determined this ellipticity by stretching the image in the z direction until the $l = 2$ coefficient is minimized. This procedure is applied to 25 images taken at different temperatures between 45 °C and 72 °C. The resulting ellipticity is $n_z/n_x = 1.056 \pm 0.002$ where all the 25 different values are within the specified confidence region. Our measured value is in excellent agreement with existing literature giving $n_z/n_x = 1.0551$ [106, 107].

No ellipticity is left after the above-mentioned image stretching operation. This allows for rotational averaging which results in a single curve as a function of Θ_y^2 for each image. A composite curve, shown in Fig. 3.4, is generated by cutting, shifting, and pasting 25 rotationally averaged images taken at different temperatures. The main peak is shifted such that it coincides with the null of the Θ_y^2 axis. The result-

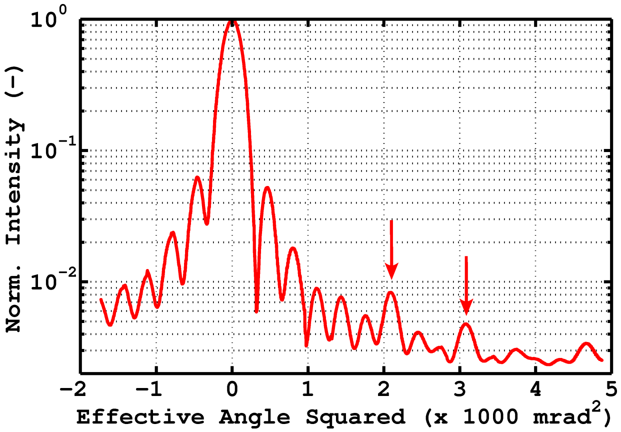

Figure 3.4: Composite plot of the measured angular intensity pattern of light generated via spontaneous parametric down-conversion in a 5-mm-*long periodically poled KTP crystal. The plot is obtained by combining 25 images of Maker fringes, like the ones shown in Fig. 3.2, photographed at different crystal temperatures ranging from* 45 °C *to* 89 °C*. The horizontal axis represents the square of the far field angle at a crystal temperature of* 60.7 °C*. The intensity values of the nodes have limited quantitative meaning (see text for details). The sixth and ninth fringe stand out and are marked with arrows. The same PPKTP crystal is used in Figs. 3.2, 3.3, 3.5, and 3.6.*

ing Θ_y^2 axis now relates without offset to the mismatch parameter ϕ in Eq. (3.2). Unfortunately, the node intensities in Fig. 3.4 have limited quantitative meaning as these intensities depend on the presence or absence of nearby bright fringes (see below).

The average distance between subsequent side lobes in Fig. 3.4 is measured to be $\Delta\Theta_y^2 = (325 \pm 8)$ mrad^2. The angular dependence of the phase-matching condition is theoretically described by Eq. (3.6). The measured external angle corresponds to the internal angle in Eq. (3.6) via $\Theta_y \approx n_z \theta_y$. The expected distance between subsequent side lobes thus becomes $\Delta\Theta_y^2 = 2\pi c n_z / L\omega = 299$ mrad^2 using the refractive index of Ref. [106]. We tentatively attribute the small discrepancy between the measured and the expected value for $\Delta\Theta_y^2$ to an unintended but possibly present 5% magnification in the imaging system.

Quite surprisingly, the minima in Fig. 3.2 do not go to zero, although all images have already been corrected for dark counts and stray light. The images in Fig. 3.2 and the curve in Fig. 3.4 have an offset of about $10^{-2.85} \approx 0.15\%$ of the peak intensity. The divergence of the pump laser of 0.7 mrad is too small to explain this observation. Additionally, we have observed that the intensity in a node is strongly reduced if we let a nearby bright fringe disappear from the image by increasing the temperature. For example, the intensity in the first minimum drops from 2.72% at

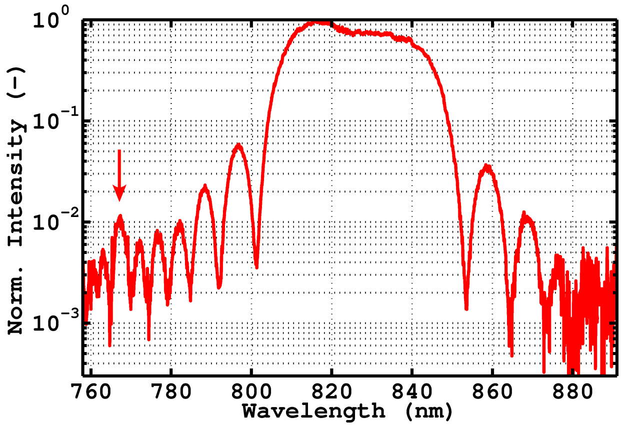

Figure 3.5: Spectrum of light generated via spontaneous parametric down-conversion in a 5-mm-*long periodically poled KTP crystal. The crystal is pumped by a mildly focussed beam at a wavelength of* 413.1 nm*. This spectrum is measured within a cone-shaped solid angle of* 42 mrad^2 *in forward direction. The crystal temperature is* 60.7 °C *at which phase matching is achieved in forward direction [see Fig. 3.2(b)]. The sixth fringe stands out and is marked with an arrow. The same PPKTP crystal is used in Figs. 3.2, 3.4, 3.3, and 3.6.*

$T = 60.7$ °C (collinear phase matching) to 0.56% at $T = 63.6$ °C, where the first minimum is in the forward direction. It thus seems that the intensity in a node is enhanced under the influence of nearby (bright) fringes. This effect can possibly be explained by a small degree of scattering from the crystal, predominantly in near-forward directions.

Characterization of the poling structure via the shape of the generated SPDC rings, is ideally suited for rapid inspection. We have applied this technique not only at the crystal center, but also over the full 1 mm x 2 mm cross-section of the crystal. This inspection reveals a large uniformity in both transverse directions. The observed ring patterns are almost identical at any position of the pump beam, including the prominent appearance of the sixth and ninth ring. The minor variation that we do observe occurs upon displacement in the 2 mm wide y direction and not in the 1 mm thick z direction. Two fringe patterns, corresponding to two pump positions that are 1.4 mm separated from each other along the y direction, are shown in Fig. 3.3. These images show the largest differences that we have observed, and even these are very small. The peak conversion efficiency (at phase-matching temperature) varies at most 2.5% over the y direction and only 1% over the z direction. We conclude that the observed deviations from perfect poling are present over the full cross-section, and show minor variations along the y direction.

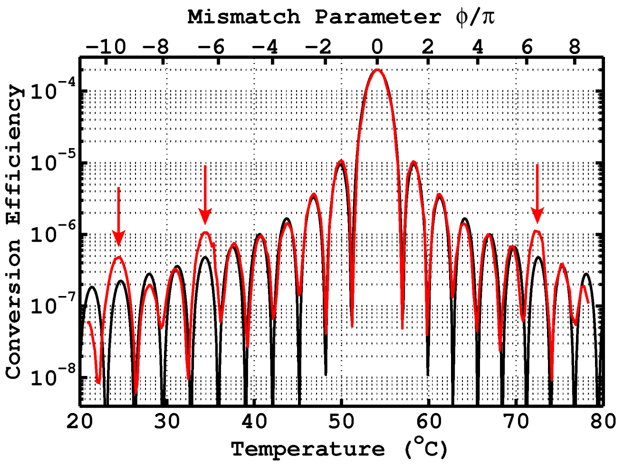

Figure 3.6: Red curve: measured temperature dependence of the conversion efficiency in SHG in a 5-mm-*long periodically poled KTP crystal that is pumped by a weakly focussed beam* ($w_0 = 61 \pm 4\ \mu\mathrm{m}$) *at a wavelength of* $825.9\ \mathrm{nm}$ *and a pump power of* $270\ \mathrm{mW}$. *The nonlinear temperature dependence of the mismatch parameter* ϕ *is indicated by the nonequidistant markers on the* ϕ *axis on top of the figure. The sixth and ninth fringe stand out and are marked with arrows. The same PPKTP crystal is used in Figs. 3.2, 3.4, 3.3, and 3.5. Black curve: plot of the ideal non-deformed tuning curve of Eq. (3.2).*

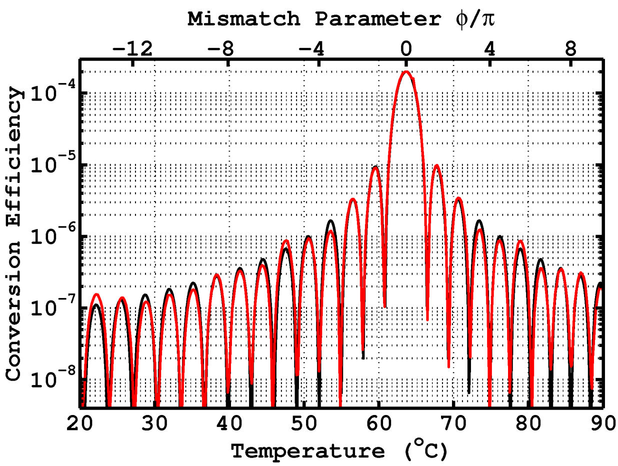

Figure 3.7: Red curve: measured temperature dependence of the conversion efficiency in SHG in a (different) 5-mm-*long periodically poled KTP crystal that is pumped by a weakly focussed beam* ($w_0 = 61 \pm 4\ \mu\mathrm{m}$) *at a wavelength of* $826.4\ \mathrm{nm}$ *and a pump power of* $270\ \mathrm{mW}$. *The nonlinear temperature dependence of the mismatch parameter* ϕ *is indicated by the non-equidistant markers on the* ϕ *axis on top of the figure. Black curve: plot of the ideal non-deformed tuning curve of Eq. (3.2).*

3.4.2 Maker fringes in spectrum of SPDC light

The spectrum of the down-converted light of the same PPKTP crystal is measured with the setup depicted in Fig. 3.1(b). We have tuned the temperature to 60.7 °C so that phase matching is achieved in forward direction. Nine different spectral images between 760 nm and 890 nm have been recorded, each having a spectral width of $\Delta\lambda = 22$ nm. We have combined these images into a singe curve in Fig. 3.5 which thus represents the spectrum of the down-converted light. The observed spectrum contains Maker Fringes [100] as the curve's shape is governed by the phase-matching condition in the crystal.

The wave vector mismatch, given by Eq. (3.6), scales as the square frequency detuning $(\Omega/2)^2$. If we convert the λ axis into a $(\Omega/2)^2$ axis we find, as expected, a sinc-shaped tuning curve. The central peak is neatly centered around zero detuning which corresponds to a wavelength of 826.2 nm, being twice the pump wavelength. The spacing between subsequent side lobes is $\Delta(\Omega/2)^2 = (4.7 \pm 0.1) \times 10^{27}$ rad^2/s^2, which is in excellent agreement with the literature value of 4.69×10^{27} rad^2/s^2 derived from the Sellmeier equation in Ref. [106]. The fact that the mismatch parameter increases with the square of the frequency detuning causes the spectrum to be very wide, having a FWHM of about 34 nm even for a 5-mm-long crystal.

Again, we observe that the sixth side lobe is standing out with respect to the neighboring side lobes. This deviation is caused by small and slowly varying deformations of the poling structure. Finally, we observe that the Maker fringes on the red side are weaker than the fringes on the blue side. We tentatively attribute this unbalance to imperfections in the calibration of the spectral response of the spectrometer and the intensified CCD camera.

3.4.3 Maker fringes in temperature dependence of SHG

The temperature-dependent conversion efficiency of the SHG process in the same PPKTP crystal is measured with the setup in Fig. 3.1(c). The obtained result, shown in Fig. 3.6, contains Maker Fringes [100] as the curve's shape is again governed by the phase-matching condition in the crystal. The spacing between the subsequent side lobes decreases at large temperatures due the nonlinear relationship between temperature and refractive index of KTP [101]. Again, the sixth and ninth side lobe are standing out with respect to the neighboring peaks. These non-sinc-like features are caused by small and slowly varying deformations in the poling structure. We now achieve phase matching at a temperature of 54.1 °C, hereby using a pump wavelength of 825.9 nm. Phase matching in the SPDC experiments (see Fig. 3.2) was achieved at a different temperature of 60.7 °C because of the slightly longer relevant SPDC wavelength of 826.2 nm.

It is preferred to plot the measured Maker fringes as a function of mismatch parameter ϕ rather than temperature. In order to make this conversion, accurate knowledge of the temperature dependence of the refractive index is needed. The temperature-dependent wave-vector mismatch in Eq. (3.4) is well described with two coefficients c_1 and c_2, defined via

$$\Delta n_z(2\omega, T) - \Delta n_z(\omega, T) = c_1[T - T_0] + c_2[T - T_0]^2, \tag{3.7}$$

because of the approximate quadratic temperature dependence of KTP's refractive index [101].

We have determined c_1 and c_2 from the measured tuning curve $\eta(T)$ by using the following procedure. The peaks and nodes of the measured tuning curve serve as markers for the mismatch parameter: $\phi = \pm(n + 1/2)\pi$ at the peaks and $\phi = \pm n\pi$ at the nodes. These markers yield the mismatch parameter ϕ at a number of temperatures. Coefficients c_1 and c_2 are obtained from a parabolic fit of Eq. (3.1) to the obtained set of mismatch parameters, after substituting Eqs. (3.7) and (3.4) into Eq. (3.1). In order to obtain reliable values for c_1 and c_2, we have applied this fitting method to five different PPKTP crystals. The tuning curve of one of these crystals is shown in Fig. 3.7. It closely resembles the ideal sinc^2-shape, thus showing that the poling structure of this second 5 mm long crystal is almost without any deformation. This curve is measured at a slightly longer pump wavelength of 826.4 nm instead of 825.9 nm causing phase matching to occur at 63.7 °C instead of 54.1 °C.

Our resulting coefficients are $c_1 = (24.0 \pm 0.2) \times 10^{-6}$ °C^{-1} and $c_2 = (4.8 \pm 0.3) \times 10^{-8}$ °C^{-2} at an approximate pump wavelength of 826 nm and a reference temperature of $T_0 = 25$ °C. The influence of the thermal expansion [102] on ϕ is only small ($\sim 4\%$) compared to the influence of the change in refractive index. The obtained coefficients are used to add a ϕ axis at the top of Fig. 3.6 and Fig. 3.7. The conversion from the measured $\eta(T)$ to the preferred form of $\eta(\phi)$ is now completed. We will use $\eta(\phi)$ for further analysis in Sec.3.5.

We now compare our values for c_1 and c_2 with existing literature. Reference [101] gives an explicit expression for $\Delta n_z(\omega, T)$ between vacuum wavelengths of 532 nm and 1585 nm. From this expression we calculate $c_1 = 23.56 \times 10^{-6}$ °C^{-1} and $c_2 = 8.6 \times 10^{-8}$ °C^{-2}. The c_1 coefficient is in reasonable agreement with our value, but there is a distinct discrepancy between the values for c_2. We conclude that it is inappropriate to extrapolate the expression for $\Delta n_z(\omega, T)$ in Ref. [101] to our pump wavelength of 413 nm. This wavelength is needed to calculate $\Delta n_z(2\omega, T)$ in Eq. (3.7).

Finally, we have measured the temperature dependence of SHG in five different PPKTP crystals of various lengths: 2 mm, 5 mm (two crystals), 10 mm, and 20 mm. The results of the two 5-mm-long crystals have already been presented in Figs. 3.6 and 3.7. For the three other crystals, the period of the sinc-pattern is inversely proportional to the length of the crystal, as expected from Eq. (3.1). All crystals are of very high quality as the observed deviations from the ideal sinc-shape are even weaker than the features visible in Fig. 3.6.

3.5 Interpretation of Maker fringes in terms of poling quality

3.5.1 Fourier analysis of small and slowly varying deformations of the poling structure

An ideal periodically poled crystal has a sinc^2-shaped tuning curve. In practice, however, small deformations of the poling structure are often present, and such deformations reveal themselves as non-sinc-like features in the tuning curve $\hat{\eta}(\delta\Delta k)$. Fejer *et al.* [89] have analyzed the effects of various types of deformations on the tuning curve. In this subsection, we extend their treatment to a Fourier analysis of small and slowly varying deformations of the poling structure along the crystal. Faster deformations on a length scale of only a few lattice periods go unnoticed, as they are associated with very high harmonics that fall outside the experimental range of the observed Maker fringes. We make a clear distinction between slowly varying deformations of the poling phase and slowly varying deformations of the poling duty-cycle.

We consider second harmonic generation (SHG) and spontaneous parametric down-conversion (SPDC) under the conditions described in Sec. 3.2. The crystal length L_0 and the number of domains N relate to the design value of the poling period via $\Lambda_0 = 2L_0/N$. The tuning curve is peaked at any wave-vector mismatch Δk_0 obeying $|\Delta k_0| = 2\pi m/\Lambda_0$, where m can be any odd-valued quasi-phase-matching order. The positions of the domain boundaries required for perfect poling are $x_{n,0} = n\Lambda_0/2$.

Our analysis is restricted to imperfect positioning of the domain boundaries, i.e., to poling functions $d(x)$ that occupy two discrete levels $\pm d_{\mathrm{eff}}$. We specify the spatial deformations via the position error $\delta x_n \equiv x_n - x_{n,0}$ of the n_{th} domain boundary and introduce the phase error at the domain boundaries for fixed $\Delta k = \Delta k_0$ as

$$\Phi_n \equiv \Delta k_0 \delta x_n. \tag{3.8}$$

Note that our definition of Φ_n only contains the effects of the poling deformation. This definition differs from the one used by Fejer *et al.* [89], as their Φ_n also includes the accumulated phase due to the wave-vector mismatch $\delta\Delta k \equiv \Delta k - \Delta k_0$.

The conversion efficiencies of SHG and SPDC are affected by the poling deformations. The up-converted electric field in the process of SHG, normalized to the field in case of perfect poling is [89]

$$\hat{E}(\delta\Delta k) \equiv \frac{E(\delta\Delta k)}{E_{\text{perfect}}} = \frac{1}{N}\sum_{n=1}^{N} e^{-i\delta\Delta k x} e^{-i\Phi_n}. \tag{3.9}$$

Next, we note that the poled crystal contains $N/2$ "building blocks" each consisting of two domains with opposite poling. Each building block is characterized by its length, being approximately equal to Λ_0, and its composition, i.e., the duty-cycle of the poling. The variations in these two quantities are related to the sum and differences of Φ_n and Φ_{n+1}. By introducing a slowly varying phase function $\Phi(x)$ and amplitude function $A(x)$ as

$$\Phi(\bar{x}_{n,0}) \equiv \tfrac{1}{2}(\Phi_n + \Phi_{n+1}), \tag{3.10}$$

$$A(\bar{x}_{n,0}) \equiv \cos\left[\tfrac{1}{2}(\Phi_n - \Phi_{n+1})\right], \tag{3.11}$$

where $\bar{x}_{n,0} \equiv (n + \frac{1}{2})\Lambda_0/2$, we can rewrite Eq. (3.9) as

$$\hat{E}(\delta\Delta k) \approx \frac{1}{L}\int_{-L/2}^{L/2} A(x) e^{-i\Phi(x)} e^{-i\delta\Delta k x} dx. \tag{3.12}$$

The complex amplitude $A(x)\exp[-i\Phi(x)]$ basically isolates the Fourier components of the two-level poling function $d(x)$ close to wave vector Δk_0. The phase function $\Phi(x)$ quantifies the displacement of the building blocks, whereas the amplitude function $A(x)$ is related to the duty-cycle of these blocks via $A(x) = \sin(\pi \times \text{dutycycle})$. The tuning curve, defined as the normalized conversion efficiency, is

$$\hat{\eta}(\delta\Delta k) = |\hat{E}(\delta\Delta k)|^2. \tag{3.13}$$

Equations (3.12) and (3.13) also apply to the SPDC process (per spatial and spectral mode), for which the wave-vector mismatch is calculated via Eq. (3.5).

Equation (3.12) exhibits the following symmetries. Deformations that are restricted to duty-cycle variations only, thus having $\Phi(x) = 0$, yield $\hat{E}(\delta\Delta k) = \hat{E}^*(-\delta\Delta k)$ and a symmetric tuning curve. Turning the crystal around corresponds to the operations $\Phi(x) \Rightarrow -\Phi(-x)$, $A(x) \Rightarrow A(-x)$, and hence $\hat{E}(\delta\Delta k) \Rightarrow \hat{E}^*(\delta\Delta k)$. Therefore, a measurement of the tuning curve $\hat{\eta}(\delta\Delta k)$ can not distinguish between the two possible crystal orientations. Symmetrically deformed crystals have real-valued $\hat{E}(\delta\Delta k)$.

For further analysis we expand the phase function $\Phi(x)$ and the amplitude function $A(x)$ in Fourier series as

$$\Phi(x) - \frac{a_0}{2} = \sum_{n=1}^{\infty} a_n \cos\left(\frac{2\pi n x}{L}\right) + b_n \sin\left(\frac{2\pi n x}{L}\right), \tag{3.14}$$

$$\frac{A(x)}{A_0} - 1 = \sum_{n=1}^{\infty} c_n \cos\left(\frac{2\pi n x}{L}\right) + d_n \sin\left(\frac{2\pi n x}{L}\right), \tag{3.15}$$

where a_n, b_n, c_n, and d_n are real-valued coefficients and $0 \le A_0 \le 1$ is the real-valued average amplitude. Any nonzero a_0 can be interpreted as a longitudinal displacement of the crystal, which is obviously neither an internal crystal property nor a parameter that influences the detected tuning curve. We shall assume small deformations $\Phi(x) \ll 1$, so that a first-order Taylor expansion of $\exp[-i\Phi(x)] \approx 1 - i\Phi(x)$ can be made. By inserting the Fourier decompositions in Eq. (3.12), and hereby neglecting second-order terms with amplitudes like $a_n c_n$, we find

$$\begin{aligned}\frac{\hat{E}(\phi)}{A_0} \approx\ & \mathrm{sinc}(\phi) + \sum_{n=1}^{\infty} \frac{c_n - i a_n + b_n + i d_n}{2}\, \mathrm{sinc}(\phi + n\pi) \\ & + \sum_{n=1}^{\infty} \frac{c_n - i a_n - b_n - i d_n}{2}\, \mathrm{sinc}(\phi - n\pi),\end{aligned} \tag{3.16}$$

where $\phi \equiv \frac{1}{2}\delta\Delta k L$ is the mismatch parameter. The dependence of the generated field on the wave-vector mismatch $\delta\Delta k$ is thus found to comprise a series of shifted sinc-functions with relative weights that contain essential information on the slow (= large scale) variations of the poling period. The tuning curve $\hat{\eta}(\phi)$ is symmetric with respect to $\phi = 0$ if at least all $b_n = 0$ in combination with either all $d_n = 0$ or all $a_n = 0$.

We will now calculate the values of the tuning curve at the positions of the peaks and nodes of the non-deformed sinc-function, as these give a good impression of the poling deformation. Inserting Eq. (3.16) into Eq. (3.13) we find

$$\hat{\eta}(\phi = \pm n\pi) \approx A_0^2 \left| \frac{\tilde{\alpha}_n \mp \tilde{\beta}_n}{2} \right|^2, \tag{3.17}$$

$$\hat{\eta}\left(\phi = \pm\left[s - \tfrac{1}{2}\right]\pi\right) \approx A_0^2 \left| \frac{1}{(s - \frac{1}{2})\pi} + \frac{\tilde{\zeta}_s \mp \tilde{\xi}_s}{2} \right|^2, \tag{3.18}$$

for the nodes and peaks, respectively. The complex $\tilde{\alpha}_n$, $\tilde{\beta}_n$, $\tilde{\zeta}_s$, and $\tilde{\xi}_s$ are linked to the deformation coefficients as

$$\begin{aligned}
\tilde{\alpha}_n &\equiv (-1)^n \; [c_n - i a_n], & (3.19)\\
\tilde{\beta}_n &\equiv (-1)^n \; [b_n + i d_n], & (3.20)\\
\tilde{\zeta}_s &\equiv \frac{2}{\pi}\sum_{n=1}^{\infty}\tilde{\alpha}_n \left[\frac{1}{2(s-n)-1}+\frac{1}{2(s+n)-1}\right], & (3.21)\\
\tilde{\xi}_s &\equiv \frac{2}{\pi}\sum_{n=1}^{\infty}\tilde{\beta}_n \left[\frac{1}{2(s-n)-1}-\frac{1}{2(s+n)-1}\right]. & (3.22)
\end{aligned}$$

The $\{\tilde{\zeta}_s, \tilde{\xi}_s\}$ coefficients are uniquely determined by the deformation coefficients $\{\tilde{\alpha}_n, \tilde{\beta}_n\}$. The inverse transformations

$$\begin{aligned}
\tilde{\alpha}_n &= \frac{2}{\pi}\sum_{s=1}^{\infty}\tilde{\zeta}_s \left[\frac{1}{2(s-n)-1}+\frac{1}{2(s+n)-1}\right], & (3.23)\\
\tilde{\beta}_n &= \frac{2}{\pi}\sum_{s=1}^{\infty}\tilde{\xi}_s \left[\frac{1}{2(s-n)-1}-\frac{1}{2(s+n)-1}\right], & (3.24)
\end{aligned}$$

and the following constraint

$$\sum_{s=1}^{\infty}\frac{\tilde{\zeta}_s}{2s-1}=0, \tag{3.25}$$

can be derived from Eqs. (3.21) and (3.22). A sketch of this derivation and the physical interpretation of the coefficients are discussed in the final paragraph of this section. The fact that the inverse transformations exist, implies that both the $\{\tilde{\alpha}_n, \tilde{\beta}_n\}$-set and the $\{\tilde{\zeta}_s, \tilde{\xi}_s\}$-set individually contain all information on the poling deformations.

Equation (3.17) shows that the n_{th} node at each side of the main sinc-peak is determined by the $\tilde{\alpha}_n$ coefficient and $\tilde{\beta}_n$ coefficient only. This is because the maxima of the shifted sinc-functions in Eq. (3.16) coincide with the minima of the fundamental and all other shifted sinc-functions. The $\tilde{\alpha}$ coefficient affects both nodes in a symmetric way, whereas the $\tilde{\beta}$ coefficient can create an unbalance between the nodes. Equation (3.18) shows that the s_{th} side maximum at each side of the main sinc-peak is determined by the $\tilde{\zeta}_{(s+1)}$ coefficient and $\tilde{\xi}_{(s+1)}$ coefficient only. The reason being that $\tilde{\zeta}_{(s+1)}$ and $\tilde{\xi}_{(s+1)}$ are the coefficients of sinc functions that are shifted by $(s+1/2)\pi$, thus exchanging the role of minima and maxima. The $\tilde{\zeta}$ coefficient affects both side lobes in a symmetric way, whereas the $\tilde{\xi}$ coefficient can create an unbalance between the side lobes.

The transformation from the $\{\tilde{\alpha}_n, \tilde{\beta}_n\}$ coefficients to the $\{\tilde{\zeta}_s, \tilde{\xi}_s\}$ coefficients is related to a transformation from the Fourier basis $\{\cos[2\pi n x/L],\ \sin[2\pi n x/L]\}$ to an alternative basis comprising the shifted harmonic functions $\{\cos[2\pi(s -$

$\frac{1}{2})x/L]$, $\sin[2\pi(s-\frac{1}{2})x/L]\}$. Apart from sign conventions, Eqs. (3.21)-(3.24) correspond to projections between those two function bases with an imposed zero-offset constraint. The explicit relation between the $\{\tilde{\zeta}_s, \tilde{\xi}_s\}$ coefficients and the poling deformations is

$$\begin{aligned}\Phi(x) - \frac{a_0}{2} &= \sum_{s=1}^{\infty}\left\{(-1)^s \mathrm{Im}(\tilde{\zeta}_s)\cos\left[\frac{2\pi\left(s-\frac{1}{2}\right)x}{L}\right]\right. \\ &\qquad\left. +(-1)^{s+1}\mathrm{Re}(\tilde{\xi}_s)\sin\left[\frac{2\pi\left(s-\frac{1}{2}\right)x}{L}\right]\right\}, \qquad (3.26)\end{aligned}$$

$$\begin{aligned}\frac{A(x)}{A_0} - 1 &= \sum_{s=1}^{\infty}\left\{(-1)^{s+1} \mathrm{Re}(\tilde{\zeta}_s)\cos\left[\frac{2\pi\left(s-\frac{1}{2}\right)x}{L}\right]\right. \\ &\qquad\left. +(-1)^{s+1}\mathrm{Im}(\tilde{\xi}_s)\sin\left[\frac{2\pi\left(s-\frac{1}{2}\right)x}{L}\right]\right\}. \qquad (3.27)\end{aligned}$$

The constraint in Eq. (3.25) ensures that the averages of the right-hand sides of Eq. (3.26) and Eq. (3.27) are zero.

3.5.2 Analysis of Maker fringes in terms of poling quality

As a typical experimental example we will analyze the measured tuning curve shown in Fig. 3.6 in a quantitative way. The poling quality of this crystal is very high as its tuning curve almost perfectly resembles the sinc^2-shape as given by Eq. (3.2). However, small deviations from the ideal curve are clearly visible, as, for example, the sixth and ninth side lobes are standing out with respect to the neighboring peaks. These non-sinc-like features are caused by small and slowly varying deformations in the poling structure that cover hundreds of poling periods. The reason is that the measured ϕ range covers about 20 sinc-nodes only, whereas the total amount of sinc-nodes in between two phase-matching orders, like $m = 1$ and $m = 2$, equals the number of domains which is about $2L_0/\Lambda_0 = 2770$.

An important ingredient of the Fourier analysis presented in Sec. 3.5.1 is the subdivision of the crystal into "building blocks", each block comprising two consecutive domains with opposite poling. The analysis distinguishes between variations of the poling phase, i.e., the longitudinal displacement of the building blocks, and variations of the poling duty-cycle that are related to the composition of the building blocks. The Fourier coefficients $\{a_n, b_n\}$, defined in Eq. (3.14), correspond to poling phase variations and the coefficients $\{c_n, d_n\}$ in Eq. (3.15) correspond to duty-cycle variations. We compare the experimental observations with our Fourier-model by first considering the effects of solely poling phase variations and afterwards considering the effects of solely duty-cycle variations.

We start by considering the effects of solely poling phase variations, mathematically corresponding to $c_n = d_n = 0$. This assumption is inspired by the fact that this category of deformations has a first-order effect on the tuning curve, whereas duty-cycle variations are only visible in second-order [see Eqs. (3.10) and (3.11)]. The symmetry with respect to $\phi = 0$ observed in Fig. 3.6 indicates that $b_n \approx 0$. The most prominent features are observed in the $\pm 6_{\mathrm{th}}$ and $\pm 9_{\mathrm{th}}$ side lobes (one outside figure). The tuning curve at the $\pm 6_{\mathrm{th}}$ peaks is measured to be $\hat{\eta} = 0.54\%$, whereas the expected value is only $\hat{\eta} = 0.24\%$. From these values and the assumption of an approximate constant duty-cycle, we find $\tilde{\zeta}_7 \approx \pm 0.11i$. The associated phase function $\Phi(x) = \pm 0.11 \cos(6\frac{1}{2} \times \frac{2\pi x}{L})$ corresponds to a periodic displacement of the domain boundaries by only $0.11\Lambda_0/2\pi m = 64$ nm over a typical period of $1/6\frac{1}{2}$ of the crystal length. This calculation shows that even very small variations in the poling phase have the potential to strongly enhance the intensities of the side lobes.

The assumption of an approximately fixed duty-cycle is however incompatible with the observation that the $\pm 3_{\mathrm{rd}}$ and $\pm 8_{\mathrm{th}}$ side lobes are lower than the expected peak height at both sides of the central peak. Equation (3.18) shows that a pair of side lobes can be lowered symmetrically, only if $\Re(\tilde{\zeta}) < 0$. Any nonzero real part of $\tilde{\zeta}$ is formed by nonzero c_n coefficients and thus by variations of the poling duty-cycle. We therefore conclude that the observed non-sinc-like features in Fig. 3.6 can not be caused by slowly varying deformations of the poling phase alone.

Next, we consider the effects of solely duty-cycle variations, mathematically corresponding to $a_n = b_n = 0$. This assumption is inspired by the fact that the observed tuning curve is almost perfectly symmetric, which is automatically the case when solely duty-cycle variations are assumed. Equation (3.18) gives the height of the side lobes, and it indicates that a real-valued $\tilde{\zeta}_s$ has a first-order effect on the side lobe strength, whereas an imaginary-valued $\tilde{\xi}_s$ has only a second-order effect. Therefore, it is possible to make a good estimate of $\{\tilde{\zeta}_s\}$ from the measured side lobe strengths alone. For example, from the measured $\pm 6_{\mathrm{th}}$ side lobes in Fig. 3.6, it is found that $\tilde{\zeta}_7 \approx 0.049$, corresponding to the amplitude function $A(x) = A_0[1 + 0.049 \cos(6\frac{1}{2} \times \frac{2\pi x}{L})]$. Assuming an average duty-cycle of 50%, the 9.8% variation in the amplitude function $A(x)$ corresponds to a duty-cycle variation between 36% and 64%. We thus find that the potential effect of duty-cycle variations on the tuning curve is relatively weak compared to the potential effect of poling phase deformations.

One might wonder whether or not it is possible to retrieve all deformation coefficients from a measurement of the tuning curve $\hat{\eta}(\phi)$. In general, it is not possible to do this inversion. For example, a sign-flip of all a_n and d_n coefficients will not change the outcome of the measurement. The large number of free parameters in the deformation model possibly limits the amount of retrievable information even further. Under some assumptions on the nature of the deformations, like the ones on duty-cycle variation discussed above, more stringent requirements on the amplitudes of the deformations apply. Whatever the assumptions, the observed tuning curve always corresponds to a Fourier analysis of the amplitude function $A(x)$ and the poling phase function $\Phi(x)$. Non-sinc-like features in the tuning curve $\hat{\eta}(\phi)$ around the $n_{\rm th}$ side minimum must correspond to variations in $A(x)$ and $\Phi(x)$ with a typical period of L/n.

Finally, we summarize the above-described analysis on the nature and strength of the poling deformations. The approximate symmetry in Fig. 3.6 indicates that all $b_n \approx 0$. The measurement also proves that some c_n coefficients must be nonzero as some pairs of side lobes are lowered symmetrically at both sides of the main peak. In order to fully explain the observed symmetry in the tuning curve, it is also needed that either all $a_n \approx 0$ or all $d_n \approx 0$. We assume that $a_n \approx 0$, as we suppose that any realistic duty-cycle deformation mechanism would not distinguish between the c_n and d_n coefficients. We thus conclude that the poling deformations in the investigated PPKTP crystal comprise duty-cycle variations only. The stronger sixth side lobes in Fig. 3.6 correspond to a periodic 9.8% peak-to-peak variation in the amplitude function $A(x) = \sin(\pi \times \text{dutycycle})$.

It is likely that the origin of the variations of the duty-cycle lies in the fabrication process of PPKTP. The process for the fabrication of the domain pattern is based on electric field poling [112]. An important issue during the patterning process is domain broadening [109, 113]. The amount of domain broadening directly determines the duty-cycle, and hence domain broadening is likely to be the origin of the small deformations that we observe. Our observation in Sec. 3.4.1, that the poling deformations are the same at any z position of the pump beam, is consistent with the observation of Rosenman *et al.* [113], that domain broadening occurs dominantly in the first few microns close to the electrical contacts needed for the poling production.

3.6 Conclusions

We have demonstrated three different methods to measure the tuning curve of a periodically poled $KTiOPO_4$ crystal (PPKTP), utilizing the processes of spontaneous parametric down-conversion (SPDC) and second harmonic generation (SHG). The three methods concern a measurement of the angular intensity pattern of collinear SPDC light, the spectrum of SPDC light, and the temperature-dependent conversion efficiency in SHG. We have shown that the three methods are fully consistent, and that the outcomes are in agreement with current knowledge of KTP's material properties. We refer to the observed fringe pattern in the tuning curve as Maker fringes [100]. The angular intensity pattern of SPDC light directly visualizes the Maker fringes. We therefore consider this method to be an ideal tool to quickly characterize the poling quality.

The observed angular intensity pattern in SPDC exhibits two interesting aspects. First, we have observed that the fringe pattern is slightly elliptical, which is caused by the birefringence of KTP. The observed ellipticity of 5.5% is in excellent agreement with current knowledge of KTP's birefringence. Secondly, we observe that the images exhibit a small degree of fringe blurring and an offset intensity of about 0.15%. These two observations can possibly be explained by a small degree of scattering from the crystal, predominantly in near-forward directions.

Our measurements of the Maker fringes contain essential information about slowly varying deformations of the poling structure. These large scale imperfections of the poling structure manifest themselves as deformations of the tuning curve close to the point of perfect phase matching. We have developed a Fourier analysis for these deformations. An important ingredient of the analysis is the subdivision of the crystal into "building blocks", each block comprising two consecutive domains with opposite poling. The Fourier analysis distinguishes between variations of the poling phase, i.e., the longitudinal displacement of the blocks, and variations of the poling duty-cycle that are related to the composition of the building blocks. We give explicit expressions for the tuning curve, depending on the Fourier coefficients of the deformations. Our measurements of the tuning curve exhibit small non-sinc-like features. It is proven that these deviations can not be explained by slowly varying deformations of the poling phase alone. We show that the observed features are probably caused by variations of the poling duty-cycle alone. A specific feature in the observed tuning curve corresponds to a variation of the duty-cycle between 36% and 64%.

We have measured the angular intensity pattern of SPDC light for various pump positions on the crystal. The measurements reveal a uniformity in both transverse directions, as some prominent features in the fringe pattern are present at any pump position. Closer inspection, however, reveals a very small variation of the fringe pattern along the y direction of the crystal. We do not observe any variation of the fringe pattern along the z direction. The ferroelectric poling structure is fabricated via low temperature electrical poling, by applying a periodic electrode pattern on one of the polar z surfaces of the crystal. We conclude that the poling deformations must originate from close to the electrodes and remain uniform along the z direction of the crystal.

3.7 Acknowledgements

This work has been supported by the Stichting voor Fundamenteel Onderzoek der Materie. We thank A. Skliar for providing information about the crystals and the production process.

4

Engineering of two-photon spatial quantum correlations behind a double slit

This chapter demonstrates the engineering of spatially entangled two-photon states behind a double slit by tailoring the incident pure two-photon state. We experimentally characterize many different two-photon states by measuring their complete two-photon interference patterns in the far field of the double slit. Spatial entanglement right behind the double slit can reside in either the modulus or the phase of the two-photon field. The balance between these two types of entanglement is fully controlled by experimentally utilizing the phase-front curvatures of the pump beam and the phase-matching profile. We project either a far-field image or a magnified near-field image of the two-photon source onto the double slit. Our theoretical analysis shows how the two-photon interference pattern behind the double slit effectively acts as a phase-sensitive probe of the incident two-photon field profile. We thus present phase-sensitive measurements of the generated two-photon field profile probed in an image plane of the two-photon source.

W. H. Peeters, J. J. Renema, and M. P. van Exter, *Engineering of two-photon spatial quantum correlations behind a double slit*, Physical Review A **79**, 043817 (2009)

(Selected for the Virtual Journal of Quantum Information, May 2009)

4.1 Introduction

Two photons are spatially entangled if their spatial degrees of freedom, residing in the phase space of transverse position and transverse momentum, are quantum correlated. This form of entanglement can be easily generated via the nonlinear process of spontaneous parametric down-conversion (SPDC), where a single pump photon splits into a pair of down-converted photons [59, 68]. Spatial quantum correlations between two photons have played a pivotal role in many landmark experiments on fourth-order spatial interference [7, 23], ghost imaging and ghost interference [52, 68, 114, 115], quantum lithography [30, 116], and orbital angular-momentum entanglement [16,117]. Other experiments have addressed wave-particle complementarity [25,29] and duality of one-photon and two-photon interferences [27–29,78]. Identification of spatial entanglement has been demonstrated via combined position-momentum measurements [118, 119] and a recent violation of Bell inequalities [120, 121].

Spatial entanglement created via SPDC is of a high-dimensional form, and the spatial Schmidt modes are generally quite complicated [9]. This spatial structure becomes less complicated by projecting each photon onto an array of holes. Behind a double slit, for example, the spatial entanglement exists between two transmitted photons of which each photon resides in a two-dimensional Hilbert space spanned by the upper slit and lower slit modes. Two-photon transmission through a double slit has been demonstrated with both indistinguishable [27, 29] and distinguishable photons [24–26, 28, 30–35]. Extensions to high-dimensional forms of entanglement have been realized by using multi-slit apertures [122–125]. Methods for characterizing spatial entanglement behind a double slit have been demonstrated in Refs. [32, 33, 35].

To set the stage for further discussion, we restrict ourselves to double-slit illumination schemes that obey mirror symmetry with respect to the optical axis. The transmitted two-photon state then takes the form

$$|\Psi_{2\mathrm{ph}}\rangle = \cos(\alpha/2)\left(\frac{|\uparrow\downarrow\rangle + |\downarrow\uparrow\rangle}{\sqrt{2}}\right) + e^{i\varphi}\sin(\alpha/2)\left(\frac{|\uparrow\uparrow\rangle + |\downarrow\downarrow\rangle}{\sqrt{2}}\right), \tag{4.1}$$

where $|\uparrow\rangle$ and $|\downarrow\rangle$ represent transmissions through the upper slit and lower slit, respectively, and where α and φ represent the state parameters. In principle, the above expression covers a large variety of two-photon spatial quantum correlations behind a double slit.

Experiments so far have addressed only a subclass of all two-photon states represented by Eq. (4.1). In many papers [24–29, 32, 33, 35, 122–125], the double slit is positioned far away from the two-photon source where transmission is dominated by photons emerging from opposite slits so that $0 \leq \alpha \leq \frac{1}{2}\pi$. Some of these papers have demonstrated how to control α within this range [28,29,33,125]. The opposite case, where both photons emerge from the same slit and $\alpha = \pi$, has been realized by positioning the double slit very close to the two-photon source [30,34]. This two-photon state plays a central role in the field of quantum lithography [116]. Until now, parameter α has not been tuned within the range $\frac{1}{2}\pi \leq \alpha \leq \pi$. No attention has been paid to the experimental tuning of φ either, and most experiments seem to operate at $\varphi \approx 0$. Yet, it is known that φ is highly relevant for the degree and type of spatial entanglement behind the double slit [33]. One could, for example, consider a maximally entangled state at $\alpha = \varphi = \frac{1}{2}\pi$ where the entanglement resides in the phase rather than the modulus of the two-photon field right behind the double slit [126].

In this chapter we demonstrate full control over the state parameters α and φ. We achieve this by tailoring the imaging system in between the two-photon source and a single double slit. We switch between two imaging schemes: the near-field imaging scheme and the far-field imaging scheme. The near-field imaging scheme images (a plane close to) the two-photon source onto the double slit. We will call φ the *curvature phase* because we control this phase by utilizing the phase front curvatures of both the phase-matching profile and the pump beam profile. We characterize more than 30 different two-photon states by measuring their complete two-photon interference patterns in the far field of the double slit. Our theoretical analysis provides a direct connection between the incident two-photon field profile and the state parameters α and φ. We show that the two-photon interference pattern behind the double slit effectively acts as a phase-sensitive probe of the incident two-photon field profile.

In our experiments, we use frequency degenerate SPDC in a periodically poled crystal where the signal and idler photons have the same polarization (type-I SPDC). Hence, the obtained spatial quantum correlations exist between indistinguishable photons. Our theoretical analysis, however, also applies to type-I SPDC in a uniform crystal and type-II SPDC in a periodically poled crystal. The analysis in this chapter can thus also be used to engineer spatial quantum correlations between distinguishable photons.

The chapter is organized as follows. The first theoretical part in Sec. 4.2 describes how to engineer two-photon spatial quantum correlations behind the double slit. We describe how parameters α and φ depend on the incident two-photon field for the far-field and near-field imaging schemes. The second theoretical part in Sec. 4.3 describes one-photon and two-photon interferences behind the double slit. Section 4.4 describes the experimental apparatus. The experimental results can be found in Sec. 4.5. The tuning of the two-photon state is illustrated with a number of measured two-photon interference patterns. The observed one-photon and two-photon interference patterns are compared with theory. The chapter ends with a concluding section and a discussion on the possibility to tune two-photon spatial quantum correlations in a higher-dimensional Hilbert space. The Appendix discusses the validity of our engineering model for various types of phase matching.

4.2 Theory: Two-photon state engineering

4.2.1 Electromagnetic field behind double slit

The electromagnetic field behind a double slit is considered. We assume the field to be the response to an incident quasimonochromatic two-photon field in a pure state. Transmission through the double slit can happen in three ways: either both photons come through, one photon comes through and the other one is blocked, or both photons are blocked. The density matrix of the electromagnetic field behind the double slit can thus be written as

$$\hat{\rho}_{\text{out}} = P_0|\text{vac}\rangle\langle\text{vac}| + P_1\hat{\rho}_{1\text{p}} + P_2|\Psi_{2\text{ph}}\rangle\langle\Psi_{2\text{ph}}|, \tag{4.2}$$

where the first term represents vacuum, the second term represents a mixed one-photon field (one photon blocked), and the third term represents a pure two-photon field (both photons transmitted). Equation (4.2) emphasizes that experiments involving a single detector depend on both the one-photon component and the two-photon component.

We now direct our attention to the two-photon part $|\Psi_{2\text{ph}}\rangle$ of the transmitted state. Each photon can pass the double slit through either the upper or lower slit. We will denote these two spatial modes by $|\uparrow\rangle$ and $|\downarrow\rangle$, respectively. The most general form of the two-photon part of the transmitted state can thus be written as

$$|\Psi_{2\text{ph}}\rangle = c_1|\uparrow\uparrow\rangle + c_2|\uparrow\downarrow\rangle + c_3|\downarrow\uparrow\rangle + c_4|\downarrow\downarrow\rangle, \tag{4.3}$$

where the two Hilbert spaces belong to the two photons. We will now restrict ourselves to illumination setups that obey mirror symmetry with respect to the optical axis (see Fig. 4.1). This symmetry implies that $c_1 = c_4$ and $c_2 = c_3$ so that reversal of all arrows leaves the quantum state unaltered. With this restriction, the most general form of the two-photon state becomes

$$|\Psi_{2\text{ph}}\rangle = \cos(\alpha/2)\left(\frac{|\uparrow\downarrow\rangle + |\downarrow\uparrow\rangle}{\sqrt{2}}\right) + e^{i\varphi}\sin(\alpha/2)\left(\frac{|\uparrow\uparrow\rangle + |\downarrow\downarrow\rangle}{\sqrt{2}}\right), \tag{4.4}$$

being a coherent superposition of two states that we will denote as *antipaired* and *paired*. In the antipaired state the two photons emerge from opposite slits. In the paired state the photons stick together and emerge from the same slit, being either the upper slit or the lower slit. Figure 4.2 shows how the two-photon state can be

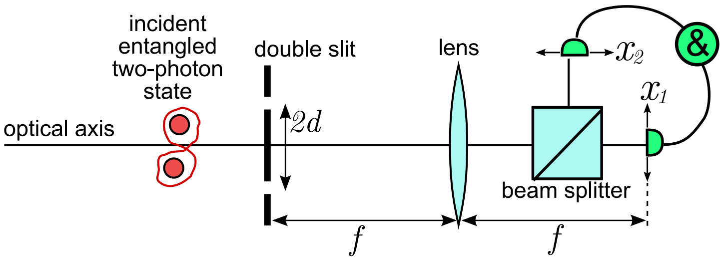

Figure 4.1: Detection part of the double-slit setup supporting the theoretical framework in Secs. 4.2 and 4.3.

depicted as a point on a two-particle Bloch sphere. We call φ the *curvature phase* because it depends on the phase-front curvature of the incident two-photon field (details in Secs. 4.2.2-4.2.5).

The quantum state in Eq. (4.4) represents a spatially entangled qubit pair, where the quantum information of each photonic qubit is encoded in its spatial properties. The degree of entanglement within a qubit-pair is often quantified via the concurrence [127, 128]. For our case, the concurrence becomes [33]

$$C = \sqrt{1 - \sin^2(\alpha)\cos^2(\varphi)}. \tag{4.5}$$

On the two-qubit Bloch sphere of Fig. 4.2, the concurrence equals the distance from the point on the sphere to the vertical axis of the sphere. Quantum states on the horizontal equator ($\varphi = \pm\pi/2$) are maximally entangled regardless the value of α. Quite remarkably, until now, hardly any attention has been paid to the experimental tuning of φ. This chapter describes how to tune both α and φ.

In our experiments, the two photons are not distinguishable by their energy or polarization. Probabilistic separation is achieved with a beam splitter behind the double slit (see Fig. 4.1). The spatial quantum correlations are detected after post selection on simultaneous clicks of two detectors in the output ports of the beam splitter. The events in which the photons are reflected or transmitted in pairs are discarded. The experiments could fairly easily be extended to distinguishable spatially entangled photons by using type-II SPDC in a periodically poled crystal (see Sec. 4.2.3).

4.2.2 Quantum state engineering

The main point of this chapter is to demonstrate full control over the two-photon state behind the double slit as given by Eq. (4.4). We thus need to describe how α and φ depend on the incident quasimonochomatic pure two-photon state $|\Psi_{\text{in}}\rangle$. The

$$\left|\Psi_{2\mathrm{ph}}\right\rangle = \cos\left(\tfrac{\alpha}{2}\right)\left|\Psi^{+}\right\rangle + e^{\mathrm{i}\varphi}\sin\left(\tfrac{\alpha}{2}\right)\left|\Phi^{+}\right\rangle$$

$$\left|\Psi^{+}\right\rangle \equiv \frac{1}{\sqrt{2}}\Big(\left|\uparrow\downarrow\right\rangle + \left|\downarrow\uparrow\right\rangle\Big) \quad \text{[anti-paired]}$$

$$\left|\Phi^{+}\right\rangle \equiv \frac{1}{\sqrt{2}}\Big(\left|\uparrow\uparrow\right\rangle + \left|\downarrow\downarrow\right\rangle\Big) \quad \text{[paired]}$$

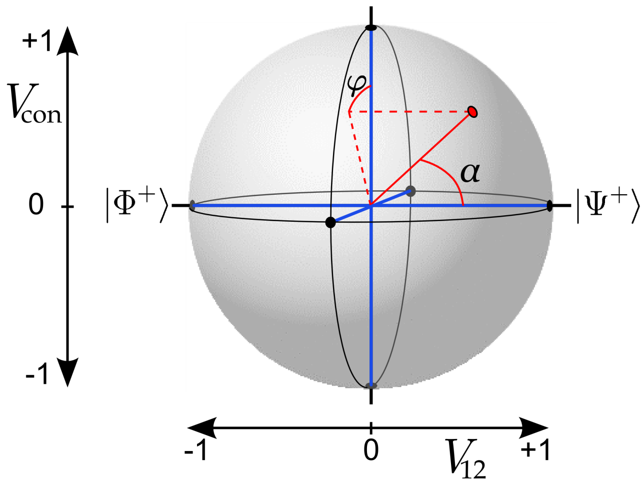

Figure 4.2: Bloch-sphere representation of a two-qubit state $|\Psi_{2\mathrm{ph}}\rangle$ that is restricted to the two-dimensional expression shown above. The states $|\Phi^+\rangle$ and $|\Psi^+\rangle$ are two of the four maximally entangled Bell states. The indicated two-photon visibilities $V_{12} = \cos(\alpha)$ and $V_{\mathrm{con}} = \sin(\alpha)\cos(\varphi)$ directly relate to the position on the sphere. The concurrence of $|\Psi_{2\mathrm{ph}}\rangle$ is given by $C = \sqrt{1 - V_{\mathrm{con}}^2}$. The two-qubit state is thus maximally entangled on the horizontal equator.

incident state is fully characterized by the two-photon field profile in the double-slit plane,

$$A_{\mathrm{slits}}(x_1, x_2) \equiv \langle \mathrm{vac}|\hat{E}^{(+)}_{\mathrm{slits}}(x_1)\hat{E}^{(+)}_{\mathrm{slits}}(x_2)|\Psi_{\mathrm{in}}\rangle. \tag{4.6}$$

The operator $\hat{E}^{(+)}_{\mathrm{slits}}(x)$ is the positive frequency electric field operator at transverse position x in the double-slit plane. The two-photon field profile can be interpreted as the complex probability amplitude for simultaneous detection of one photon at position x_1 and the other photon at transverse position x_2.

The two-photon field profile behind the double slit is just the sampled version of the incident two-photon field profile. We now assume that the slits are narrower than any spatial structure of the incident two-photon field profile. The transmitted two-photon state is then fully characterized by four complex amplitudes $A_{\mathrm{slits}}(\pm d, \pm d)$, where $2d$ is the slit separation. Because of the assumed mirror symmetry with respect to the optical axis we have $A_{\mathrm{slits}}(d, d) = A_{\mathrm{slits}}(-d, -d)$ and

$A_{\text{slits}}(d,-d) = A_{\text{slits}}(-d,d)$. The first pair of two-photon amplitudes corresponds to paired photons, and the latter pair corresponds to antipaired photons. The coefficients of the transmitted two-photon state in Eq. (4.4) can thus be associated with the incident two-photon field profile via

$$p \equiv e^{i\varphi} \tan\left(\frac{\alpha}{2}\right) = \frac{A_{\text{slits}}(d,d)}{A_{\text{slits}}(d,-d)}. \tag{4.7}$$

Here, we have defined p as the *engineering parameter*, which fully determines the transmitted two-photon state. Equation (4.7) plays a central role in this chapter because it describes the relationship between the incident two-photon field profile and the two-photon state behind the double slit.

4.2.3 Incident two-photon state

In this section we calculate the incident two-photon field profile for a two-photon state produced via the nonlinear process of SPDC. We consider frequency degenerate SPDC in the low-conversion regime with cw pumping along the positive z direction. The nonlinear crystal has two parallel planar facets in transverse xy planes separated by length L. We assume the divergence of the pump beam to be small such that the Rayleigh range is much larger than the crystal length. The pump photon has energy $\hbar\omega_p$, and the signal and idler photons each has approximately energy $\hbar\omega_0 = \frac{1}{2}\hbar\omega_p$.

The phase-matching condition is essential for the precise form of the generated two-photon field profile. All equations derived below are based on noncritical type-I phase matching. Noncritical phase matching is generally applied in periodically poled crystals, and it means that the pump beam is orientated along a principal axis of the crystal. However, in the Appendix we show that our analysis also applies to noncritical type-II as well as critical type-I phase matching. In the latter case, the transverse walk-off distance of the pump should be much smaller than the pump beam diameter, which can be achieved by sufficiently loose focusing of the pump.

The first step toward quantum state engineering is to calculate the two-photon field profile in the crystal-center plane. Following Ref. [69], we write for the momentum representation of this two-photon field profile

$$\tilde{A}_{\text{crys}}(\mathbf{q}_1, \mathbf{q}_2) \propto \tilde{E}_p(\mathbf{q}_1 + \mathbf{q}_2)\tilde{\xi}(\mathbf{q}_1 - \mathbf{q}_2), \tag{4.8}$$

where the tilde symbol indicates the spatial Fourier transform, $\tilde{E}_p(\mathbf{q})$ is the momentum representation of the pump profile in the crystal-center plane, and $\mathbf{q}_{1,2}$ are the transverse wave vectors of the two photons. The phase-matching profile is

$$\tilde{\xi}(\Delta\mathbf{q}) = \text{sinc}\left(\phi_0 + \frac{L|\Delta\mathbf{q}|^2}{8n_0\omega_0/c}\right), \tag{4.9}$$

where $\mathrm{sinc}(x) \equiv \sin(x)/x$, L is the crystal length, and n_0 is the refractive index at the down-converted frequency. The ϕ_0 term accounts for the phase mismatch in forward direction.

The second step is to calculate the propagation from the crystal toward the double slit. The propagation of the two-photon field profile is described via

$$A_{\mathrm{slits}}(\mathbf{x}_1, \mathbf{x}_2) = \iint A_{\mathrm{crys}}(\mathbf{x}', \mathbf{x}'') h(\mathbf{x}_1, \mathbf{x}') h(\mathbf{x}_2, \mathbf{x}'') d\mathbf{x}' d\mathbf{x}'', \tag{4.10}$$

where $h(\mathbf{x}, \mathbf{x}')$ is the (classical) electric field propagator [129] from the crystal to the double slit at angular frequency ω_0. The two-photon field profile remains factorized after propagation through any paraxial $ABCD$ lens system. Therefore, it is convenient to think of the pump profile and the phase-matching profile as two separately propagating profiles. The two-photon field profile at any position z along the optical axis can thus be written as

$$A(\mathbf{x}_1, \mathbf{x}_2; z) \propto E_{p,z}\left(\frac{\mathbf{x}_1 + \mathbf{x}_2}{2}; z\right) \xi_z\left(\frac{\mathbf{x}_1 - \mathbf{x}_2}{2}; z\right), \tag{4.11}$$

where $E_{p,z}(\mathbf{x}; z)$ is the pump beam, $\xi_z(\mathbf{x}; 0) \equiv \xi(\mathbf{x})$, and $\xi_z(\mathbf{x}; z)$ is the phase-matching profile propagated at angular frequency ω_p from the crystal center to position z.

In the final step, we calculate the engineering parameter p from Eq. (4.7). This calculation requires a one-dimensional description of the incident two-photon field profile. Below, we argue why it is allowed to single out one transverse dimension in Eq. (4.11) for the imaging schemes that we use. It may, however, not be concluded that a one-dimensional treatment is permitted for any general imaging scheme. The problem is that the phase-matching profile $\xi_z(\mathbf{x}; z)$ does not factorize in two functions for the two transverse dimensions. The pump beam $E_{p,z}(\mathbf{x}; z)$, which we will assume to have a Gaussian profile, nicely factorizes in the two transverse directions.

In the far-field imaging scheme [see Fig. 4.3(b)], the slit separations that we use are much smaller than the phase-matching profile. The phase-matching profile is thus approximately constant in the region of the slits, and the two-photon field scales with the pump profile. Singling out one dimension is thus allowed for the far-field imaging scheme.

Our near-field imaging scheme [see Fig. 4.3(a)] is based on an astigmatic form of imaging, where lens 1 is a cylinder lens and lens 2 is a standard lens. This astigmatic form of imaging produces only a crystal image in the direction perpendicular to the slits (x direction), while it retains the far-field image in the direction parallel to the slits (y direction). The size of the phase-matching profile along the x direction is now similar to the slit separation, whereas the profile is much more extensive along

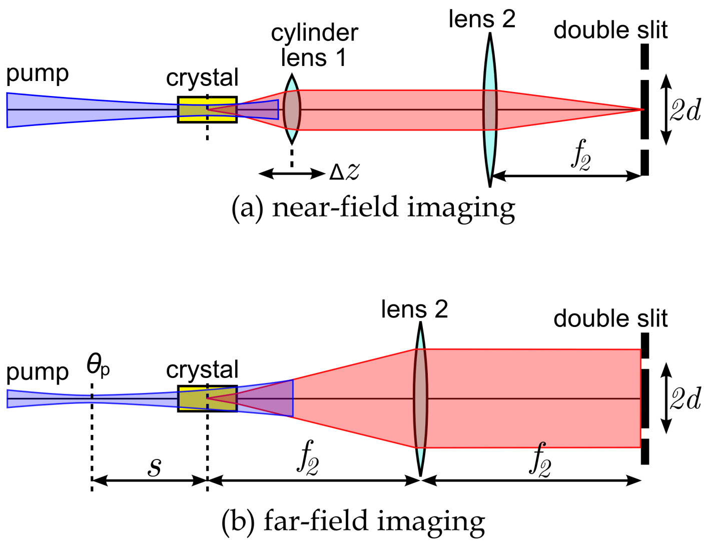

Figure 4.3: Two schemes for quantum state engineering. (a) Near-field imaging: a plane inside or close to the crystal is imaged onto the double slit. The two engineering parameters are the magnification $M \equiv f_2/f_1$ and the longitudinal position Δz of lens 1. The illustration shows $\Delta z = 0$, where the front focal plane of lens 1 coincides with the crystal center. (b) Far-field imaging: the far field of the crystal, which is pumped by a Gaussian beam, is imaged onto the double slit. The two engineering parameters are the pump divergence θ_p and longitudinal position of the pump waist s.

the y direction. Furthermore, detection occurs via projection on round detection modes that are much smaller than the phase-matching profile along y direction in the double-slit plane (2.1 mm versus 9.2 mm full width at half maximum intensity). The incident two-photon field profile is thus probed only around $q_y \simeq 0$, and singling out the x dimension is allowed.

4.2.4 Near-field imaging scheme

Our near-field imaging scheme can produce any two-photon state on the left hemisphere of the two-qubit Bloch sphere (see Fig. 4.2). The working principle is that the crystal is imaged onto the double slit. For collinear phase matching ($|\phi_0| \ll \pi$), the two photons leave the crystal from approximately the same transverse position, and they arrive in the same way at the double slit [130]. Hence, the two-photon state behind the double slit is dominated by the paired contribution.

The near-field imaging scheme is shown in Fig. 4.3(a). The pump beam is weakly focused in the crystal-center plane. A plane close to the crystal center, i.e., within the Rayleigh range of the pump beam, is imaged onto the double slit with two lenses. The double slit is positioned in the back focal plane of the second lens;

the corresponding object plane then coincides with the front focal plane of the first lens. The precise position of the object plane can now be tuned by moving the first lens longitudinally. We call this displacement the defocus distance Δz, where $\Delta z = 0$ if the object plane coincides with the crystal-center plane, and $\Delta z > 0$ for an increased distance between lens and crystal. The magnification of the imaging system is $M \equiv f_2/f_1$, where f_1 and f_2 are the focal lengths of the first and the second lens, respectively. The slit separation is $2d$.

The profile at the double slit is just the magnified version of the two-photon field profile in the object plane. The engineering parameter p, which completely determines the two-photon state behind the double slit via Eq. (4.7), becomes

$$p = \frac{A\left(\frac{+d}{M}, \frac{+d}{M}; \Delta z\right)}{A\left(\frac{+d}{M}, \frac{-d}{M}; \Delta z\right)}, \tag{4.12}$$

where $A(x_1, x_2; z)$ is the two-photon field profile of Eq. (4.11). Note that the object plane inside the crystal has actually moved over a distance $n_0 \Delta z$. For convenience, we have used the propagation length Δz instead of $n_0 \Delta z$. This choice implies that $A(x_1, x_2; z)$ must be treated as a two-photon field profile that has propagated over a distance z through an imaginary medium with refractive index $n = 1$.

It is important to realize that the phase-matching profile $\xi_z(x; \Delta z)$ is much narrower than the pump profile $E_{p,z}(x; \Delta z)$. As a consequence, d/M is much smaller than the waist of the pump beam in the relevant range of operation. Therefore, we can approximate the engineering parameter via

$$p = \frac{E_{p,z}\left(\frac{d}{M}; \Delta z\right) \xi_z(0; \Delta z)}{E_{p,z}(0; \Delta z) \xi_z\left(\frac{d}{M}; \Delta z\right)} \approx \frac{\xi_z(0; \Delta z)}{\xi_z\left(\frac{d}{M}; \Delta z\right)}. \tag{4.13}$$

The argument and the absolute value of p are determined by the phase front curvature of $\xi_z(x; \Delta z)$ and amplitude variations of $\xi_z(x; \Delta z)$, respectively.

By using the expression for the phase-matching profile in Eq. (4.9), we find the explicit expression

$$p = \frac{\int \mathrm{sinc}\left(\phi_0 + x^2\right) \exp(-ibx^2) dx}{\int \mathrm{sinc}\left(\phi_0 + x^2\right) \exp(-ibx^2 - iax) dx}, \tag{4.14}$$

where $\mathrm{sinc}(x) \equiv \sin(x)/x$ and ϕ_0 is the phase mismatch. The dimensionless parameters

$$a \equiv \frac{2d}{M\sqrt{Lc/(n_0\omega_p)}}, \tag{4.15}$$

$$b \equiv \frac{\Delta z}{L/(2n_0)}, \tag{4.16}$$

are the scaled slit separation and the scaled defocus distance, respectively. The two-photon state behind the double slit can be engineered by tailoring parameters a and b. Unfortunately, there is no simple analytic expression for the integrals in Eq. (4.14).

We can gain physical intuition for the influence of a and b on parameter p by considering two general properties of the phase-matching profile $\xi_z(x;z)$. First, the phase front of $\xi_z(x;z)$ is flat at the crystal center. This flatness causes parameter p to be real valued for $\Delta z = 0$ making the curvature phase $\varphi = 0$. Second, $|p| > 1$ at any Δz, as the maximum of $\xi_z(x;z)$ stays at the optical axis during propagation. Numerical evaluations show that 98% of the left hemisphere of the two-qubit Bloch sphere is covered by varying $a \in [0,8]$ and $b \in [-6,6]$. These evaluations also show that the coverage can be brought arbitrarily close to 100% for larger ranges of a and b.

4.2.5 Far-field imaging scheme

Our far-field imaging scheme can produce any two-photon state on the right-hand hemisphere of the two-qubit Bloch sphere (see Fig. 4.2). The working principle is that the far field of the crystal is imaged onto the double slit. The photons propagate with approximate opposite transverse momenta, so the photons arrive at approximate opposite transverse positions in the double-slit plane. Hence, the two-photon state behind the double slit is dominated by the antipaired contribution.

The far-field imaging scheme is shown in Fig. 4.3(b). The crystal is pumped with a weakly focused Gaussian beam with divergence θ_p defined via $\tilde{E}_p(\theta\omega_p/c) \propto \exp(-\theta^2/\theta_p^2)$. The waist of the pump beam lies at a distance s in front of the crystal center. The far field of the crystal is symmetrically imaged onto the double slit by a lens with focal length f_2. The slit separation is $2d$.

It is important to realize that the far-field pump profile $\tilde{E}_p(q)$ is much narrower than the far-field phase-matching profile $\tilde{\xi}(q)$. As a consequence, d/f_2 is much smaller than the divergence of the phase-matching profile in the relevant range of operation. Therefore, the engineering parameter p can be approximated via

$$p = \frac{\tilde{E}_p\left(\frac{d\omega_p}{f_2 c}\right)\tilde{\xi}(0)}{\tilde{E}_p(0)\tilde{\xi}\left(\frac{d\omega_p}{f_2 c}\right)} \approx \frac{\tilde{E}_p\left(\frac{d\omega_p}{f_2 c}\right)}{\tilde{E}_p(0)}, \tag{4.17}$$

where the first equality is found by combining Eqs. (4.7), (4.8), and (4.10).

Insertion of the described pump profile yields the explicit expression

$$p = \exp\left[-\left(\frac{d}{f_2\theta_p}\right)^2\left(1+\frac{is}{z_{\mathrm{R}}}\right)\right], \tag{4.18}$$

where $z_{\mathrm{R}} \equiv 2c/(\theta_p^2\omega_p)$ is the Rayleigh range of the pump beam. From this expression it is clear that any two-photon state with $|p| < 1$ can be produced by tailoring the divergence of the pump beam θ_p and its waist location s. These two-photon states lie on the right-hand hemisphere of the two-qubit Bloch sphere in Fig. 4.2.

4.3 Theory: Interference behind the double slit

4.3.1 State determination by two-photon interference

This section describes how we analyze the engineered two-photon state. We show that the two-photon interference pattern in the far field of the double slit serves as a fingerprint of the quantum state described by Eq. (4.4). Figure 4.1 shows the geometry of the detection setup. The far field of the double slit is formed in the back focal plane of a lens with focal length f. The two photons are probabilistically separated by a beam splitter (see Sec. 4.2.1). Two detectors are positioned in the far-field planes formed in the two output ports of the beam splitter.

In the limit of narrow slits, the coincidence count rate in the far field of the double slit becomes [33]

$$\begin{aligned} R_{\mathrm{cc}}(x_1,x_2) \quad \propto \quad & 1 + V_{\mathrm{diff}}\cos(\phi_1-\phi_2) \\ & + V_{\mathrm{sum}}\cos(\phi_1+\phi_2) \\ & + V_{\mathrm{con}}\left[\cos(\phi_1)+\cos(\phi_2)\right], \end{aligned} \tag{4.19}$$

where the interslit phase differences ϕ_i relate to the detector positions x_i via $\phi_i = 2d\omega_0 x_i/fc$, where $2d$ is the slit separation and $\hbar\omega_0$ is the energy of each photon.

The coefficients are given by

$$V_{\text{diff}} = \cos^2(\alpha/2), \tag{4.20}$$
$$V_{\text{sum}} = \sin^2(\alpha/2), \tag{4.21}$$
$$V_{\text{con}} = \sin(\alpha)\cos(\varphi), \tag{4.22}$$

where we call V_{sum} the visibility in the sum of coordinates and V_{diff} the visibility in the difference of coordinates. Coefficient V_{con} relates to the fringe pattern in the single count rate conditioned on transmission of the second photon through the double slit. Therefore, we call V_{con} the *conditional one-photon visibility*. Note that V_{con} is allowed to become negative and that this sign has a clear and measurable physical meaning. It is just for convenience that we incorporate the sign of $\sin(\alpha)\cos(\varphi)$ in what we call the conditional one-photon visibility.

The visibilities in the sum and difference of coordinates obey $V_{\text{diff}} + V_{\text{sum}} = 1$. It is convenient to remove this redundancy and use only one quantity. Therefore, we define

$$V_{12} \equiv V_{\text{diff}} - V_{\text{sum}} = \cos(\alpha), \tag{4.23}$$

as the *two-photon visibility difference*. The interference pattern of Eq. (4.19) is now determined by just two quantities being V_{12} and V_{con}.

The far-field two-photon interference pattern serves as a fingerprint of the two-qubit state. State parameter α is determined by $V_{12} = \cos(\alpha)$ and state parameter $|\varphi|$ is then determined by $V_{\text{con}} = \sin(\alpha)\cos(\varphi)$. The two-qubit Bloch sphere in Fig. 4.2 graphically connects these visibilities to the two-photon state: the in-plane horizontal coordinate is V_{12} and the vertical coordinate is V_{con}. The sign of φ, indicating whether the state is on the front or rear side of the sphere, cannot be determined from the two-photon interference pattern. This sign, however, has limited physical meaning as the two-photon interference pattern, anywhere behind the double slit, is invariant under sign reversal of φ.

The experimental visibilities can easily be expressed in terms of the engineering parameter p, which characterizes the two-photon state behind the double slit via Eq. (4.7). By combining Eqs. (4.7), (4.22) and (4.23), we find

$$V_{12} = \frac{1 - |p|^2}{1 + |p|^2}, \tag{4.24}$$
$$V_{\text{con}} = \frac{p + p^*}{1 + |p|^2}, \tag{4.25}$$

enabling us to explicitly predict the outcome of the experiments based on the calculated parameter p.

4.3.2 Interpretation of the two-qubit Bloch sphere

The two-qubit Bloch sphere in Fig. 4.2 is a graphical representation of a pure two-qubit state that is restricted to the indicated linear superposition of two Bell states. All possible two-photon states on this sphere share a common Schmidt basis [33,83]. These Schmidt states are located on the north and south poles of the sphere, being $|\eta_+\rangle|\eta_+\rangle$ and $|\eta_-\rangle|\eta_-\rangle$, respectively, where $|\eta_\pm\rangle \equiv \frac{1}{\sqrt{2}}(|\uparrow\rangle \pm |\downarrow\rangle)$. The concurrence C is thus directly related to the vertical coordinate V_{con} on the sphere. By combining Eqs. (4.5) and (4.22) we find [33]

$$C = \sqrt{1 - V_{\mathrm{con}}^2}. \tag{4.26}$$

The physical interpretation of Eq. (4.26) is simple. If the photon pair is strongly entangled ($C \simeq 1$), the spatial state of each individual photon is necessarily mixed and cannot produce a strong interference pattern on its own ($V_{\mathrm{con}} \simeq 0$). In the opposite case of an approximately nonentangled state ($C \simeq 0$), the state of each individual photon is almost pure and produces strong interference ($V_{\mathrm{con}} \simeq 1$).

The sphere provides a clear graphical interpretation of a well-known complementarity relation between between V_{12} and V_{con}. By combining Eqs. (4.22) and (4.23) it is easily shown that [131,132]

$$V_{12}^2 + V_{\mathrm{con}}^2 \leq 1, \tag{4.27}$$

or, after inserting Eq. (4.26),

$$V_{12}^2 \leq C^2. \tag{4.28}$$

The stronger the entanglement, the larger $|V_{12}|$ is allowed to become. The absolute two-photon visibility difference $|V_{12}|$ determines the correlation strength of the transverse positions of the photons right behind the double slit. Absence of this type of correlation, however, does *not* imply absence of entanglement because the entanglement could also reside in the phase rather than the modules of the two-photon field profile [126]. Inequality (4.27) becomes an equality for two-photon states with zero curvature phase ($\varphi = 0$).

The two-qubit Bloch sphere also suggests the existence of a third visibility,

$$V_p \equiv \sin(\alpha)\sin(\varphi) = \frac{-i(p - p^*)}{1 + |p|^2}, \tag{4.29}$$

being the coordinate along the "out of paper" direction. Together with V_{12} and V_{con}, this third coordinate forms an exact complementarity relation

$$V_{12}^2 + V_p^2 = C^2. \tag{4.30}$$

In the fully entangled case, where $C = 1$ and $V_{\text{con}} = 0$, a projective measurement on photon A provides all quantum information on photon B. The basis in which this quantum information is obtained depends on the character of the entanglement. At $V_{12} = \pm 1$ and $V_p = 0$, a projection of photon A in the slit basis $|\uparrow\rangle, |\downarrow\rangle$ provides full "which path" information on photon B. At $V_{12} = 0$ and $V_p = \pm 1$, photon A must be projected onto the states $|\uparrow\rangle \pm i|\downarrow\rangle$ to obtain which path information on photon B. It is yet unclear how to experimentally determine the third coordinate V_p.

4.3.3 One-photon interference

We consider the pattern of the total intensity in the far field of a double slit that is illuminated with a pure two-photon state. The visibility of this fringe pattern is called the *unconditional one-photon visibility* V_{unc}. The unconditional and conditional one-photon visibilities generally differ from each other because V_{con} solely depends on the two-photon component behind the double slit, whereas V_{unc} also depends on the one-photon part. The electromagnetic field behind the double slit is often even dominated by the one-photon part, i.e., $P_1 > P_2$ in Eq. (4.2).

For symmetric double-slit illumination, the intensity profile in the far-field plane of the double slit (see Fig. 4.1) is of the form

$$I(x) \propto 1 + V_{\text{unc}} \cos(\phi), \tag{4.31}$$

where the interslit phase difference ϕ relates to the detector position x via $\phi = 2d\omega_0 x/fc$. Equation (4.31) implicitly defines the unconditional one-photon visibility V_{unc}. The second-order correlation function at the slits determines V_{unc} via [133]

$$V_{\text{unc}} = \frac{G^{(1)}(d, -d)}{G^{(1)}(d, d)}. \tag{4.32}$$

The outcome of this equation is real valued due to the assumed illumination symmetry of the setup. Like the conditional one-photon visibility, we have defined the unconditional one-photon visibility such that it can become negative.

To calculate V_{unc}, we need the second-order correlation function in the plane of the double slit. The second-order correlation function in a transverse plane can be calculated via [61]

$$G^{(1)}(\mathbf{x}_1, \mathbf{x}_2; z) \propto \int A^*(\mathbf{x}_1, \mathbf{x}; z) A(\mathbf{x}_2, \mathbf{x}; z) d\mathbf{x}, \tag{4.33}$$

where $A(\mathbf{x}_1, \mathbf{x}_2; z) \equiv \langle \text{vac}|\hat{E}^{(+)}(\mathbf{x}_1; z)\hat{E}^{(+)}(\mathbf{x}_2; z)|\Psi_{\text{in}}\rangle$ is the two-photon field profile and $|\Psi_{\text{in}}\rangle$ is a pure monochromatic two-photon state associated with light propagating along the optical axis. Equation (4.33) has a broader range of validity than an alternative method based on the Van Cittert-Zernike theorem [78]. The latter theorem can only be used beyond the Rayleigh range of the two-photon source, and the two-photon source should be sufficiently spatially incoherent. The validity of Eq. (4.33) is retained close to the two-photon source, even for partially coherent (realistic) two-photon sources.

As a first case, we calculate V_{unc} for the near-field imaging scheme that is treated in Sec. 4.2.4 and shown in Fig. 4.3(a). By combining the generated two-photon field in Eqs. (4.8) and (4.9), the propagation to the double slit [Eq. (4.10)], and the formulas for the unconditional one-photon visibility in Eqs. (4.32) and (4.33), we find

$$V_{\mathrm{unc,cr}} = \frac{\displaystyle\int \mathrm{sinc}^2\left(\phi_0 + x^2\right)\exp(iax)dx}{\displaystyle\int \mathrm{sinc}^2\left(\phi_0 + x^2\right)dx}, \tag{4.34}$$

where $\mathrm{sinc}(x) \equiv \sin(x)/x$ and a is the (dimensionless) scaled slit separation defined in Eq. (4.15). Again, we have assumed the pump profile to be much wider than the phase-matching profile. Unfortunately, there is no simple analytic expression for the integrals in Eq. (4.34).

As a second case, we consider the far-field imaging scheme that is treated in Sec. 4.2.5 and shown in Fig. 4.3(b). By combining Eqs. (4.8), (4.10), (4.32), and (4.33) we find

$$V_{\mathrm{unc,ff}} = \exp\left[-\frac{1}{2}\left(\frac{d}{f_2\theta_p}\right)^2\left(1+\frac{s^2}{z_{\mathrm{R}}^2}\right)\right], \tag{4.35}$$

where $2d$ is the slit separation, θ_p is the pump divergence, and $z_{\mathrm{R}} \equiv 2c/(\theta_p^2\omega_p)$ is the Rayleigh range of the pump beam. Again, we have assumed the far-field phase-matching profile to be much wider than the far-field pump profile. For this far-field imaging case, Eq. (4.35) can also be obtained via the Van Cittert-Zernike theorem.

4.3.4 Duality between unconditional one-photon interference and two-photon interference

The relationship between unconditional one-photon interference and (conditional) two-photon interference was studied earlier in Refs. [27–29, 78]. Saleh *et al.* [78] theoretically pointed out that there exists a profound duality between the two phenomena if far-field imaging is applied. In this section, we show how this duality manifests itself in our model. We find new duality relations that apply to our far-field imaging scheme, and we point out that the precise form of the duality relations strongly depends on the applied imaging scheme.

We consider far-field imaging [see Fig. 4.3(b)] with a pump beam that is loosely focused in the crystal-center plane ($s = 0$). For this specific imaging scheme we find that $p = V_{\mathrm{unc,ff}}^2$ by comparing engineering parameter p in Eq. (4.18) with V_{unc} in Eq. (4.35). By inserting p into via Eqs. (4.24) and (4.25), we directly find duality relations

$$V_{12} = \frac{1 - V_{\mathrm{unc,ff}}^4}{1 + V_{\mathrm{unc,ff}}^4} \tag{4.36}$$

$$V_{\mathrm{con}} = \frac{2V_{\mathrm{unc,ff}}^2}{1 + V_{\mathrm{unc,ff}}^4} \tag{4.37}$$

which strictly correspond to the specified imaging geometry. Equations (4.36) and (4.37) describe how the unconditional intensity pattern serves as a fingerprint of the two-photon state.

In other imaging geometries, the duality relations become generally different or might even be multivalued. For example, the duality between V_{12} and $V_{\mathrm{unc,ff}}$ was reported differently in Eq. (3.16) in Ref. [78] because the authors assumed a top-hat-shaped flat pump profile inside the crystal instead of a Gaussian-shaped flat pump profile. As another example, no one-to-one duality relations exist for the near-field imaging scheme [see Fig. 4.3(a)]. If near-field imaging is applied, some values of V_{unc} individually correspond to multiple values of V_{12} and V_{con} (see Fig. 4.6).

4.4 Experimental apparatus

4.4.1 General information

A schematic representation of the experimental apparatus is shown in Fig. 4.4. This apparatus can implement the near-field imaging scheme as well as the far-field imaging scheme. The working principles of these two imaging schemes are explained in Secs. 4.2.4 and 4.2.5. The technical details of the apparatus are given in Secs. 4.4.2 and 4.4.3.

4.4.2 Experimental apparatus in front of double slit

Photon pairs are generated via collinear spontaneous parametric down conversion (SPDC) in a periodically poled $KTiOPO_4$ (PPKTP) crystal. The conversion is such that pump, signal, and idler waves have the same linear polarization. We pump the crystal with a continuous-wave y-polarized Gaussian beam propagating along the z direction (laser: Kr^+, 200 mW at 413.1 nm). We operate in the quasimonochromatic limit by applying detection behind narrow-band spectral filters ($\Delta\lambda = 5$ nm at 826.2 nm). The crystallographic x axis of the PPKTP is oriented along z direction (pump direction) and the crystallographic z axis is oriented along the y direction (poling direction). The crystal is $L = 5.09$ mm long, 1 mm thick in y direction,

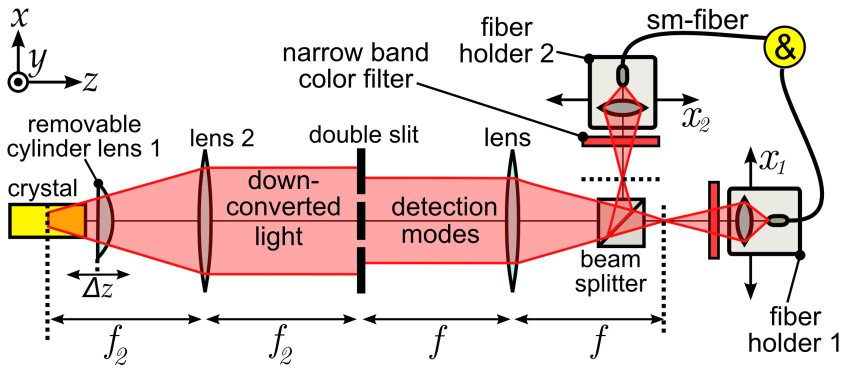

Figure 4.4: Schematic representation of the experimental apparatus. The down-converted light propagates from the crystal to the double slit via either the near-field imaging scheme (with cylinder lens) or the far-field imaging scheme (without cylinder lens). The longitudinal position of the cylinder lens can be adjusted. The two-photon interference pattern in the far field of the double slit is measured by scanning the fiber holders transversely. The two fiber holders are identical and consist of a single-mode (SM) fiber and an objective. The &-symbol represents the detection of simultaneous photon arrivals.

and 2 mm wide in x direction. The pump beam is absorbed behind the crystal by a GaP wafer that is antireflection coated for 826 nm.

It is important to know the phase mismatch ϕ_0 because it strongly affects the engineering parameter p in the near-field imaging scheme [see Eq. (4.14)]. For our 5-mm-long crystal, the temperature dependence of the phase mismatch is measured to be $\frac{\partial \phi_0}{\partial T} = 1.059\ ^\circ\mathrm{C}^{-1}$ [134]. The phase-match temperature is found to be $T_0 = (60.39 \pm 0.04)\ ^\circ\mathrm{C}$ from measurements of the temperature-dependent spectrum of the SPDC light in forward direction. All double-slit experiments are performed at a temperature $T = (60.70 \pm 0.01)\ ^\circ\mathrm{C}$ corresponding to a phase mismatch of $\phi_0 = 0.33 \pm 0.05$.

We illuminate the symmetric and centered double slit either with a centered far-field image of the source using an f-f imaging system (far-field imaging scheme) or a centered magnified image of the crystal by adding an extra cylinder lens (near-field imaging scheme). The double slit is positioned at 80 cm from the crystal center, and the fixed far-field imaging lens with focal length $f_2 = (400 \pm 1)$ mm is positioned halfway. The removable cylinder lens with focal length f_1 produces a sharp image of the crystal-center plane only in the direction perpendicular to the slits; the cylinder lens leaves the imaging in the parallel direction unaffected. The cylinder lens can be moved further away from the crystal by an amount that we call the defocus distance Δz. The y-oriented slits are created by wire electrical discharge machining in a phosphor bronze plate.

Some size parameters of the experimental apparatus are adjustable in order to be able to engineer many different two-photon states behind the double slit. In the near-field imaging scheme, we adjust the slit separation $2d$, the focal length of the cylinder lens f_1, and the defocus distance Δz. In the far-field imaging scheme, we adjust the slit separation $2d$, the pump divergence θ_p, and the distance from the pump waist to the crystal center s.

We have used six double-slit apertures with slit separations of $\{313, 510, 600, 758, 950, 1400\}$ μm, all values with ± 15 μm uncertainty. The corresponding slit widths are $\{138, 150, 193, 135, 235, 225\}$ μm. We used three different cylinder lenses with focal lengths of 12.7, 19.0, and 25.4 mm, all values with $\pm 2\%$ uncertainty. The defocus distance is varied between -0.20 and 3.30 mm. The null position of Δz corresponds to the point where the front focal plane coincides with the crystal center. This position is calibrated to a precision of ± 0.04 mm by reflecting a reference beam, which is backwardly focused in the primary focal plane of the cylinder lens on the front and rear crystal facets (reversed autocollimation). For the far-field imaging experiments with $s = 0$, we used three different pump divergences 0.73, 1.31, and 2.27 mrad, all values with 10% uncertainty. Some measurements have been performed with pump waists in front of the crystal such that $s \neq 0$.

4.4.3 Experimental apparatus behind double slit

The two photons behind the double slit are probabilistically separated with a beam splitter behind the double slit. The events where the photons are both reflected or both transmitted are discarded (see Sec. 4.2.1). A lens with focal length $f = 400$ mm is positioned between the double slit and the beam splitter. The lens images the far field of the double slit onto two intermediate detection planes in the two output ports of the beam splitter.

Detection occurs via projection onto the mode profiles of two single-mode fibers. In the double-slit plane, the centered Gaussian detection modes have (loose) waist diameters of 2.1 mm for each mode (full widths at half maximum intensity). Correspondingly, the detection modes have waist diameters of 70 μm in the intermediate detection planes (full widths at half maximum intensity). The finite size of the detection modes does not affect the observed fringe visibility because the field projection is phase sensitive, and the period of the two-photon fringe pattern is at least 240 μm which is more than three times larger than the width of the detection modes. The two-photon interference pattern is measured by scanning two computer-controlled detection stages transversely. Each detection stage comprises the fiber tip and an objective with an effective focal length of 8 mm. The detection modes thus only move in the far field of the double slit, while their intensity profiles remain fixed in the double-slit plane.

The single-mode fibers are coupled to single-photon counting modules (Perkin-

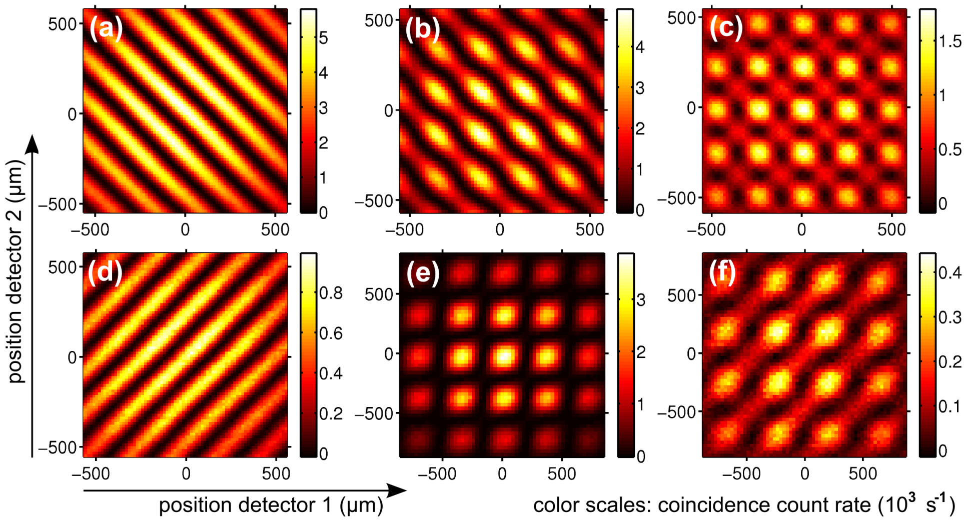

Figure 4.5: Various measured two-photon interference patterns in the far field of a double slit. Measurements (a)-(c) are obtained with the near-field imaging scheme and (d)-(f) are obtained with the far-field imaging scheme. Measurements (c) and (f) have nonzero curvature phase. The slit separation is 1.40 mm *for measurements (a)-(d),* 0.95 mm *for measurement (e), and* 0.76 mm *for measurement (f). The indicated coincidence count rates have been corrected for accidental coincidences.*

Elmer SPCM-AQR-14-FC). Simultaneous photon detections are registered by coincidence electronics. The applied gate time of our pulse correlator is $\tau_g = (1.73 \pm 0.01)$ ns. If two photons from *different* photon pairs are detected within this time window, it is fallaciously registered as a coincidence count. The count rate of these so-called *accidental* counts is

$$R_{\mathrm{ac}} = R_1 R_2 \tau_g, \tag{4.38}$$

where R_1 and R_2 are the raw single count rates in detector 1 and detector 2, respectively. The "real" coincidence count rate is obtained by subtracting the accidental count rate from the measured coincidence count rate. In our experiments, the accidental count rate typically accounts for about 10 % to 45 % of the rawly-measured coincidence count rate. The photon count integration time is 1 s for each pixel of the measured two-photon interference patterns.

4.5 Experimental results

4.5.1 General information

In this section we demonstrate the engineering of many different two-photon states behind the double slit. Each two-photon state is characterized via a measurement of the two-photon interference pattern in the far field of the double slit. The interference patterns provide the conditional one-photon visibility V_{con} and the two-photon visibility difference V_{12} for each two-photon state. The manner in which these visibilities relate to the engineered two-photon state is graphically indicated on the two-qubit Bloch sphere in Fig. 4.2. The intensity fringe patterns are also recorded. These yield the unconditional one-photon visibility V_{unc}. The analysis and tuning of the two-photon interference pattern are discussed in Sec. 4.5.2. Quantitative comparison with theory is performed in Secs. 4.5.3-4.5.6.

4.5.2 Analysis and tuning of two-photon interference patterns

Six examples of measured two-photon interference patters are shown in Figs. 4.5(a)-4.5(f). This selection covers a whole range of different double-slit imaging types. The upper row is measured with the near-field imaging scheme, and the lower row is measured with the far-field imaging scheme. The left column contains the two extreme cases where the slit separation is large compared to the coherence width of the down-converted light at the double slit. The central column is measured with slit separations similar to the coherence width. The right-hand column is measured with a certain amount of defocusing, meaning that either $\Delta z \neq 0$ for the near-field imaging scheme or $s \neq 0$ for the far-field imaging scheme.

The general form of the two-photon interference pattern, given by Eq. (4.19), allows for an insightful interpretation of the fringe visibilities. The three visibilities V_{sum}, V_{diff} and V_{con} become isolated after projections on the $+45°$ diagonal, the $-45°$ diagonal, and the horizontal axis, respectively. Mathematically, these projections result in

$$R_{+45^\circ}(x_1 + x_2) \quad \propto \quad 1 + V_{\mathrm{sum}} \cos\left(\frac{x_1 + x_2}{x_s/2\pi}\right), \tag{4.39}$$

$$R_{-45^\circ}(x_1 - x_2) \quad \propto \quad 1 + V_{\mathrm{diff}} \cos\left(\frac{x_1 - x_2}{x_s/2\pi}\right), \tag{4.40}$$

$$R_{0^\circ}(x_1) \quad \propto \quad 1 + V_{\mathrm{con}} \cos\left(\frac{x_1}{x_s/2\pi}\right), \tag{4.41}$$

where x_s is the fringe period for coherent light at the down-converted wavelength. In order not to deform the projection, it is important to select an integer number of fringe periods in the direction orthogonal to the projection axis. Each fringe pattern has been analyzed by fitting these three projections after including the effect of limited angular diffraction due to the finite slit width [33]. The two-photon visibility difference is then found via its definition $V_{12} \equiv V_{\text{diff}} - V_{\text{sum}}$. The sum $V_{\text{diff}} + V_{\text{sum}} = 1$ is automatically obeyed if the experimental apparatus is aligned properly.

In the far-field imaging scheme, the two photons arrive at approximately opposite positions in the double-slit plane. Hence, two-photon transmission is dominated by the antipaired two-photon component causing V_{12} to be positive. One quickly recognizes that the lower three interference patterns have positive V_{12} because the fringes projected on the $-45°$ diagonal are more distinct than the fringes projected on the $+45°$ diagonal. The extreme case, where the slit separation is large compared to the pump divergence, is shown in Fig. 4.5(d). This two-photon state is almost completely antipaired as we find $V_{12} = (96 \pm 1)\%$. Paired two-photon transmission can be increased by increasing the pump divergence relative to the slit separation. Such an increase has been applied to situation (e) where the fringe orientation is hardly visible and $V_{12} = (25 \pm 3)\%$.

The tuning of V_{12} in the near-field imaging scheme is analogous. The photons arrive at approximately equal positions in the double-slit plane. Hence, two-photon transmission is dominated by the paired two-photon amplitude, causing V_{12} to be negative. The extreme case is shown in Fig. 4.5(a), where the slit separation is large compared to the size of the magnified phase-matching profile. The corresponding two-photon state is almost completely paired and we determine $V_{12} = -(96 \pm 1)\%$. The antipaired two-photon transmission can be enhanced by increasing the magnification of the imaging system or reducing the slit separation. In situation (b), the slit separation is reduced to about the size of the magnified phase-matching profile $\xi_z\left(\frac{x}{M}; \Delta z = 0\right)$ resulting in $V_{12} = -(89 \pm 1)\%$.

The conditional one-photon visibility can be interpreted as the fringe visibility produced by each individual photon of the transmitted pair. By projecting the two-photon fringe pattern on the horizontal axis, it is easily recognized that patterns (a) and (d) have $V_{\text{con}} \approx 0$. The conditional one-photon visibility is close to 100% for pattern (e). Patterns (b) and (f) feature $V_{\text{con}} < 0$ because each of these two patterns has a minimum in the center of the image. The other four patterns have centered maxima corresponding to $V_{\text{con}} \geq 0$. Calibration of detector positions $x_{1,2} = 0$ is performed via measurements of the coincidence count rate without double slit. Patterns (b) and (f) correspond to two-photon states on the lower hemisphere of the two-qubit Bloch sphere in Fig. 4.2.

Patterns (c) and (f) are special because they have nonzero curvature phase φ. Such configurations can only be achieved with defocused two-photon imaging, meaning that $\Delta z \neq 0$ for near-field imaging or $s \neq 0$ for far-field imaging. The characterizing feature of defocusing is the emergence of a checkerboardlike pattern.

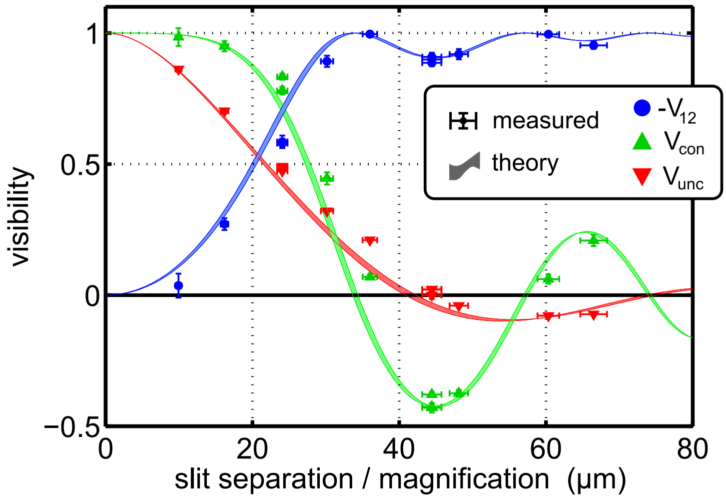

Figure 4.6: Measured visibilities obtained with the near-field imaging scheme of Fig. 4.3(a) at $\Delta z = 0$, for various reduced slit separations $2d/M$. The theoretical two-photon visibilities V_{12} and $V_{\rm con}$ are calculated via Eqs. (4.24) and (4.25) for the two-photon state with engineering parameter p from Eq. (4.14). The theoretical curve for the unconditional one-photon visibility $V_{\rm unc}$ is calculated via Eq. (4.34). The uncertainty in the theoretical curves, indicated by finite curve widths, originates from the uncertainty in the phase mismatch $\phi_0 = 0.33 \pm 0.05$. No fit parameters are used for the theoretical curves.

This changes the topology of the interference pattern by splitting the dark curves of zero coincidences into patches of low coincidence counts. A checkerboardlike pattern reduces the conditional one-photon visibility so that the two-photon state is brought closer to the horizontal equator of the two-qubit Bloch sphere.

The degree of entanglement is directly related to the conditional one-photon visibility via Eq. (4.26). Maximum entanglement manifests itself as $V_{\rm con} = 0$ and a total absence of separability of the interference pattern in horizontal and vertical directions. Patterns (a) and (d), on one hand, correspond to maximally entangled states as these have zero conditional one-photon visibility. Pattern (e), on the other hand, corresponds to an almost nonentangled two-photon state as the pattern almost factorizes.

The curvature phase is highly relevant for the degree of entanglement. Pattern (c), for example, has $V_{12} = -0.14 \pm 0.01$ which is rather close to zero, and, at the same time, it is strongly entangled with a concurrence of $C = 0.906 \pm 0.008$. Such combination is only possible if the curvature phase is nonzero. The curvature phase is $|\varphi| = (64.7 \pm 1.0)^\circ$ for pattern (c). The entanglement has almost fully "migrated" from the modulus to the phase of the two-photon field profile right behind the double slit [126].

4.5.3 Near-field imaging at $\varphi = 0$

This section presents the experimental results obtained with the near-field imaging scheme of Fig. 4.3(a) with zero defocus $\Delta z = 0$. We only vary the reduced slit separation $2d/M$, where M is the magnification of the imaging system. Working at zero defocus, we expect to engineer two-photon states with zero curvature phase $\varphi = 0$. Figure 4.6 depicts the measured visibilities V_{12}, V_{con}, and V_{unc} versus the reduced slit separation. The vertical error bars are based on the internal errors and scan resolutions of the two-photon interference patterns. The theoretical curves for V_{12} and V_{con} are based on Eqs. (4.24), (4.25), and (4.14). The theoretical curve for V_{unc} is a plot of Eq. (4.34). We observe good agreement between experiment and theory.

The three plots in Fig. 4.6 contain a wealth of information. First of all, the shape of each curve is directly related to the phase-matching profile of the periodically poled crystal. Our theoretical curves are based on the sinc-shaped phase-matching profile in momentum representation [see Eq. (4.9)]. The observed agreement between experiment and theory means that the phase-matching profile is indeed sinc shaped in its momentum representation. Second, we observe that V_{con} and V_{unc} are negative for some values of the reduced slit separation. Negativity of these parameters means that we observe minima instead of maxima in the centers of the measured interference patterns. Finally, we observe that V_{con} and V_{unc} are different from each other. For the near-field imaging scheme, there is no one-to-one duality relation between these visibilities like there is for the far-field imaging scheme [see Eq. (4.37)]. Interestingly, the experiments prove that V_{unc} can be zero, while the two-photon state behind the double slit is not maximally entangled for the same geometry ($V_{\text{con}} \neq 0$).

Closer inspection of Fig. 4.6 indicates that the majority of the measurements seem to be slightly on the right-hand side of the theoretical curves. We do not know the origin of this systematic error for certain, but a suspicious parameter is the phase mismatch ϕ_0. It was determined to be $\phi_0 = 0.33 \pm 0.05$ from measurements of the SPDC spectrum. However, if we would plot the theoretical visibilities using $\phi_0 = 0.65$ we would observe excellent agreement between theory and measured visibilities. This means that a systematic error of only 0.3 °C in the phase-matching temperature would already explain the observed small systematic difference between experiment and theory.

In Fig. 4.7 the engineered two-photon states are depicted as points in a square with V_{12} and V_{con} along the axes. The points on the left half plane correspond to the measurements from the near-field imaging scheme. The measurements are in excellent agreement with the complementarity relation $V_{12}^2 + V_{\text{con}}^2 = 1$ that is predicted for two-photon states with zero curvature phase $\varphi = 0$.

Previously, of the two-photon states with $V_{12} < 0$, only the fully paired two-

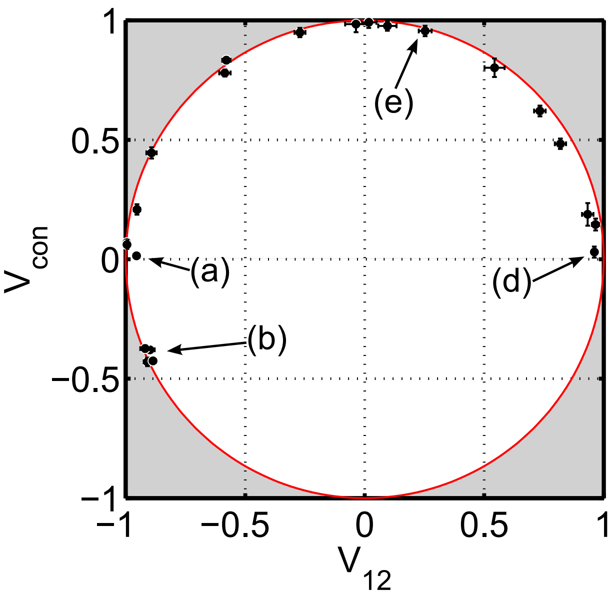

Figure 4.7: Measured visibilities of engineered two-photon states with zero curvature phase $\varphi = 0$. The two-photon states on the left side are prepared with the near-field imaging scheme in Fig. 4.4(a) at $\Delta z = 0$. The two-photon states on the right are prepared with the far-field imaging scheme in Fig. 4.4(b) at $s = 0$. The annotated measurements correspond to fringe patterns in Fig. 4.5. The exterior of the circle is forbidden by the complementarity relation $V_{\rm con}^2 + V_{12}^2 \leq 1$. Figure 4.2 graphically indicates how $V_{\rm con}$ and V_{12} relate to the engineered two-photon state.

photon state had been prepared by positioning a double slit with large slit separation very close to the crystal [30,34,125]. We now demonstrate that the fully paired two-photon state can also be prepared by imaging the two-photon source onto a double slit. To the best of our knowledge, two-photon states corresponding to $-1 < V_{12} < 0$ or $V_{\rm con} < 0$ have never been prepared before. Our experiments with the near-field imaging scheme are the first phase-sensitive measurements of the two-photon field structure in the image plane of the crystal center. Our measurements of $V_{\rm unc}$ in this regime are measurements of the second-order coherence function in the image plane of the crystal center.

4.5.4 Far-field imaging at $\varphi = 0$

We present the experimental results obtained with the far-field imaging scheme of Fig. 4.3(b) with zero defocus ($s = 0$), where we expect to engineer two-photon states with zero curvature phase $\varphi = 0$. We only vary the relative slit separation $2d/(2f_2\theta_d)$, where $2f_2\theta_d$ is the diameter of the pump beam in the double-slit plane.

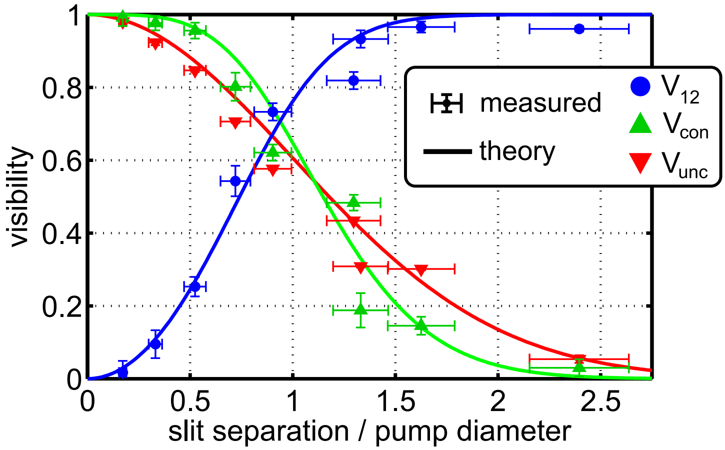

Figure 4.8: Measured visibilities obtained with the far-field imaging scheme of Fig. 4.3(b) at $s = 0$ for various configurations of the slit separation $2d$ relative to the Gaussian pump diameter in the double-slit plane $2f_2\theta_p$. The theoretical two-photon visibilities V_{12} and $V_{\rm con}$ are calculated via Eqs.(4.24) and (4.25) for the two-photon state with engineering parameter p from Eq. (4.18). The expected curve for the unconditional one-photon visibility $V_{\rm unc}$ is calculated via Eq. (4.35). No fit parameters are used for the theoretical curves.

Figure 4.8 depicts the measured visibilities V_{12}, $V_{\rm con}$, and $V_{\rm unc}$ versus the relative slit separation. The horizontal error bars are determined by the 10% uncertainty in the pump divergence. The vertical error bars are based on the internal error and scan resolution of the two-photon interference patterns. The theoretical curves for V_{12} and $V_{\rm con}$ are based on Eqs. (4.24), (4.25), and (4.18). The theoretical curve for $V_{\rm unc}$ is a plot of Eq. (4.35).

We observe excellent agreement between theory and the measured visibilities. For small slit separations we observe that the two-photon visibility difference $V_{12} \approx 0$, meaning that the moduli of the paths of the two photons are hardly correlated. We also observe that these states are approximately nonentangled because $V_{\rm con} \approx 1$. For larger slit separations V_{12} approaches 1, indicating that the concurrence increases, and $V_{\rm con}$ goes down. Furthermore, we observe that the conditional and the unconditional one-photon visibilities are different from each other. Interesting is the observation that the curves for $V_{\rm con}$ and $V_{\rm unc}$ cross each other. This crossing has neither been predicted nor observed before. It is in agreement with the duality relation of Eq. (4.37).

Each engineered two-photon state can be depicted as a point in a square with V_{12} and $V_{\rm con}$ along the axes. This representation is visualized in Fig. 4.7, where the points on the right half plane correspond to our measurements from the far-field imaging scheme. The measurements are in excellent agreement with the complementarity relation $V_{12}^2 + V_{\rm con}^2 = 1$ that is predicted for two-photon states with zero

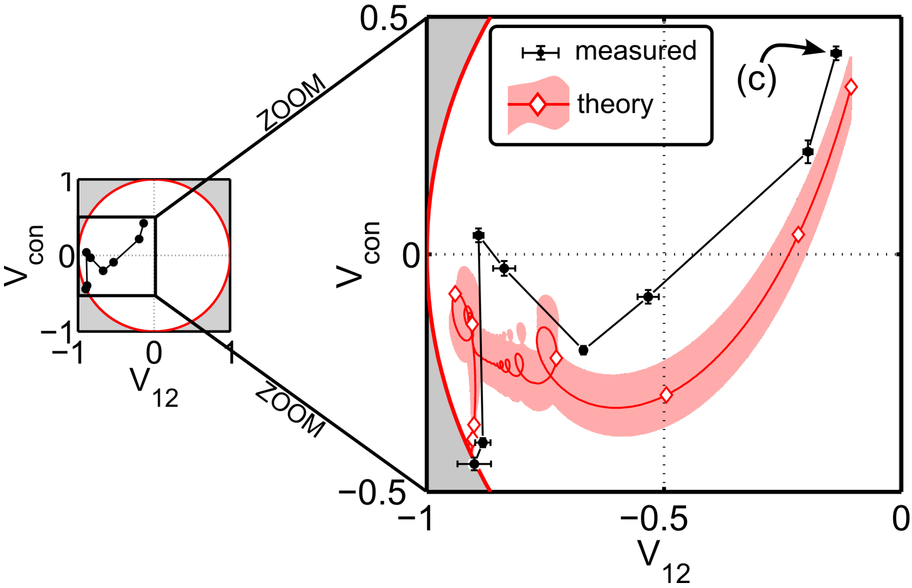

Figure 4.9: Measured visibilities of two-photon states engineered with the near-field imaging scheme of Fig. 4.3(a) at increasing defocus Δz. The series contains measurements at eight equidistant displacements of the cylinder lens ranging from $\Delta z = -(0.20 \pm 0.04)$ mm to $\Delta z = (3.30 \pm 0.04)$ mm at the annotated measurement (c). The theoretical curve is calculated via Eqs. (4.24) and (4.25) with engineering parameter p from Eq. (4.14). The points on the theoretical curve (diamonds) relate to the measured points in the indicated order. The uncertainty of the theoretical curve originates from the phase mismatch $\Delta\phi_0 = 0.33 \pm 0.05$ and a $\pm 3\%$ uncertainty in the reduced slit separation $2d/M$. The annotated measurement corresponds to fringe pattern (c) in Fig. 4.5.

curvature phase $\varphi = 0$. Previously, an experimental demonstration of complementarity was performed by Abouraddy *et al.* [29], albeit with less accuracy.

4.5.5 Near-field imaging at nonzero curvature phase

Two-photon states with nonzero curvature phase have been engineered with the near-field imaging scheme in Fig. 4.3(a) at nonzero defocus distance $\Delta z \neq 0$. A plane slightly behind the crystal center is imaged onto the double slit. Due to the propagation away from the crystal-center plane, the phase-matching profile $\xi_z(z; \Delta z)$ has developed a certain wave-front curvature. This wave-front curvature causes the curvature phase φ to become nonzero. The curvature phase is highly relevant for the two-photon interference pattern behind the double slit. The characterizing feature of two-photon states with $0 < |\varphi| < \pi$ is that $V_{12}^2 + V_{\rm con}^2 < 1$, implying that these states are located in the interior of the complementarity circle. The curvature phase is also relevant for the degree of entanglement.

Figure 4.9 shows the two-photon visibilities V_{12} and V_{con} of eight two-photon states that are engineered with the near-field imaging scheme at increasing defocus distance Δz. For this series, we have used a reduced slit separation of $2d/M = (44.5 \pm 1.3)$ μm and eight equidistant values of Δz. We observe that the two-photon state at $\Delta z \approx 0$ has approximately zero curvature phase, as this measurement lies on the complementarity circle $V_{12}^2 + V_{\mathrm{con}}^2 = 1$. For increasing defocus, we observe that the two-photon states obtain nonzero curvature phases, as their two-photon visibilities lie in the interior of the complementarity circle.

The theoretical curve, including its uncertainty region, is calculated from the engineering parameter p given by Eq. (4.14). The visibilities V_{12} and V_{con} are then derived via Eqs. (4.24) and (4.25). The wiggly nature of the theoretical curve in Fig. 4.9 originates from the Fresnel-type integrals in the equation for p. We observe reasonable agreement between theory and experiment. All the more so, a strong resemblance is found when considering the relative orientation of two points within any pair of successive measurement points. This resemblance is striking because these relative orientations are quite erratic while the defocus distance Δz is increased over equidistant values.

The measurements in Fig. 4.9 are the first phase-sensitive measurements of the two-photon field structure in an image of a plane close to the crystal center, i.e., within the Rayleigh range of the phase-matching profile $\xi_z(x; z)$.

4.5.6 Far-field imaging at nonzero curvature phase

Two-photon states with nonzero curvature phase have also been engineered with the far-field imaging scheme in Fig. 4.3(b) at $s \neq 0$. The phase front of the pump beam in the double-slit plane is curved now because the pump waist is located in front of the nonlinear crystal. The wave-front curvature of the pump beam in the double-slit plane causes the curvature phase φ to become nonzero. States with nonzero curvature phase have $V_{12}^2 + V_{\mathrm{con}}^2 < 1$ implying that such states are located in the interior of the complementarity circle. The curvature phase is relevant for the two-photon interference pattern as well as the degree of entanglement.

Figure 4.10 shows the two-photon visibilities V_{12} and V_{con} of six two-photon states that are engineered with the far-field imaging scheme with $s \neq 0$. We observe that the two-photon state behind the double slit has nonzero curvature phase as the states lie inside the complementarity circle. We also demonstrate that it is possible to reach the lower hemisphere of the two-qubit Bloch sphere ($V_{\mathrm{con}} < 0$ in Fig. 4.2) by altering the pump beam. Two-photon states on the lower hemisphere have never been prepared before.

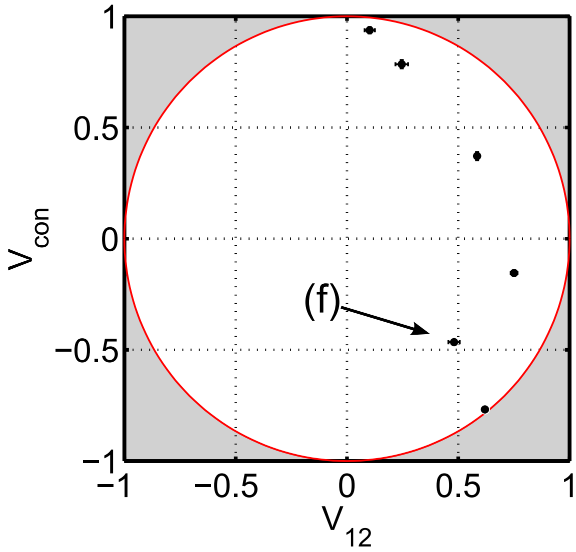

Figure 4.10: Measured visibilities of two-photon states engineered with the far-field imaging scheme of Fig. 4.3(b) at pump beam defocus $s \neq 0$. The annotated measurement corresponds to fringe pattern (f) in Fig. 4.5.

4.6 Conclusion

This chapter demonstrates the engineering and characterization of spatially entangled two-photon states behind a double slit that is symmetrically illuminated with a pure two-photon state. Engineering is achieved by tailoring the optical imaging system in between the two-photon source and the double slit. We have discussed a near-field imaging scheme where the two-photon source itself is imaged onto the double slit. The curvature phase φ has also been introduced. It is shown that φ is highly relevant for the two-photon interference pattern as well as the degree of entanglement behind the double slit. State characterization is achieved by performing measurements of the complete two-photon interference pattern in the far field of the double slit.

The presented analysis of two-photon state engineering is complete for illumination systems within the following three restrictions. First, we consider illumination schemes and double slits that obey mirror symmetry around the optical axis (see Sec. 4.2.1). Second, we assume slits that are narrower than the transverse coherence width of the illumination (see Sec. 4.2.2). Third, the two-photon source is based on any type of SPDC in a periodically poled crystal or type-I SPDC in a uniform crystal provided that the transverse walk-off of the pump beam is negligible with respect to its width (see Sec. 4.2.3 and Appendix).

For a symmetric setup and narrow slits, the two-photon state behind the double slit becomes a coherent superposition of a *paired* state, where the photons emerge form the same slit, and an *antipaired* state, where the photons appear from opposite slits. The relative phase between both contributions is the curvature phase φ. The absolute balance between the paired and antipaired components is described by state parameter α.

It is demonstrated how to engineer any two-photon state in this form. The paired two-photon component dominates if the near-field imaging scheme is used. The antipaired two-photon component dominates if the far field of the source is imaged onto the double slit. The precise balance between the paired and antipaired components is controlled by tailoring the magnification properties of these imaging systems. The curvature phase φ is fully controlled by utilizing the phase-front curvatures of the pump profile $E_{p,z}(x;z)$ and phase-matching profile $\xi_z(x;z)$. The phase-matching profile governs the engineered two-photon state in the near-field imaging scheme. The pump profile governs the engineered two-photon state in the far-field imaging scheme.

We have shown that the two-photon interference pattern in the far field of the double slit serves as a fingerprint of the engineered two-photon state. The pattern directly yields the one-photon visibility V_{con} and the two-photon visibility difference V_{12}. These visibilities conveniently relate to the position on the two-qubit Bloch sphere that we have presented to graphically depict any engineered two-photon state. This sphere is also highly convenient to read off the concurrence.

We have engineered and characterized more than 30 different two-photon states. Good agreement between measurements and theory is observed. Two-photon states exhibiting strong curvature phase, states with $V_{\text{con}} < 0$, and states with $-1 < V_{12} < 0$ have never been prepared before. Our experiments with the near-field imaging scheme are phase-sensitive measurements of the two-photon field structure in an image of a plane close to the crystal center, i.e., within the Rayleigh range of the phase-matching profile $\xi_z(x;z)$.

Using the near-field imaging scheme, we have presented measurements of the unconditional one-photon visibility V_{unc} in an image plane of the crystal center. In the far-field imaging scheme, we have demonstrated the duality between V_{con} and V_{unc} for Gaussian pump profile that is loosely focused in the crystal-center plane. The experimental results are in agreement with theory.

4.7 Discussion: tuning in high-dimensional Hilbert space

In this chapter, the tuning range of the engineered two-photon states has been restricted to a two-dimensional Hilbert space spanned by two out of four maximally entangled Bell states [see Eq. (4.4)]. However, spatially entangled two-photon states generated via SPDC allow for tuning in much higher-dimensional Hilbert space. We will now discuss some experimental tuning parameters that remained untouched in this chapter.

The entire four-dimensional Hilbert space of Eq. (4.3) becomes accessible if one allows asymmetric illumination schemes with distinguishable photons. The coefficients c_1 and c_4 become uncoupled by allowing asymmetric illumination schemes. Such asymmetry could be achieved by applying an asymmetric pump profile or by moving the double slit transversely to a noncentered position. The coefficients c_2 and c_3 become uncoupled if one uses distinguishable photons in combination with an asymmetric illumination scheme. Distinguishable spatially entangled photons can be produced via type-II SPDC in a periodically poled crystal [31, 34, 115] or by using two double-slit apertures positioned in the two output ports of a beam splitter. An experiment where $c_2 = -c_3$ has been demonstrated in Ref. [31] by placing birefringent crystals in front of the double slit.

One can also turn to multidimensionally entangled two-photon states by using multi-slit apertures [122–125]. To tune between different multidimensionally entangled states, one could use a variable pump profile based on a spatial light modulator. Another interesting tuning parameter is the temperature-dependent phase mismatch ϕ_0 of the periodically poled crystal. The analysis in this chapter may serve as a good starting point to make the extension to quantum state engineering of multidimensionally entangled two-photon states.

4.8 Acknowledgements

We acknowledge stimulating discussions with J. P. Woerdman, D. Bouwmeester, and E. F. C. Driessen. The research is supported by the Stichting voor Fundamenteel Onderzoek der Materie (FOM).

4.9 APPENDIX: Validity of the model for various phase-matching geometries

The theoretical analysis in this chapter is based on noncritical type-I phase matching (see Sec. 4.2.3). In this Appendix, however, we show that the analysis also applies to noncritical type-II as well as critical type-I phase matching. Noncritical phase matching is generally applied in quasi-phase-matched processes, and critical phase matching is generally applied in uniform crystals.

We will first give expressions for the two-photon field profile in the crystal-center plane for various phase-matching geometries. We consider a nonlinear crystal with two parallel planar facets in transverse xy planes. For the critically phase-matched cases treated below, the crystallographic optical axis lies in the positive yz plane.

Following Refs. [69] and [89] we use a generic quasimonochromatic expression for the two-photon field profile in the crystal-center plane.

$$\tilde{A}_{\text{crys}}(\mathbf{q}_1, \mathbf{q}_2) \propto \tilde{E}_p(\mathbf{q}_1 + \mathbf{q}_2)\text{sinc}\left[\tfrac{1}{2}L\Delta k_z(\mathbf{q}_1, \mathbf{q}_2)\right], \tag{4.42}$$

where $\text{sinc}(x) \equiv \sin(x)/x$, and the wave-vector mismatch

$$\begin{aligned}\Delta k_z(\mathbf{q}_1, \mathbf{q}_2) \quad &= \quad k_z(\mathbf{q}_1 + \mathbf{q}_2, \omega_p, \sigma_p) - k_z(\mathbf{q}_1, \omega_0, \sigma_1) \\ &\quad\quad -k_z(\mathbf{q}_2, \omega_0, \sigma_2) - \left(2\pi\Lambda^{-1}\right),\end{aligned} \tag{4.43}$$

where $k_z(\mathbf{q}, \omega, \sigma)$ is the z component of the wave vector of a plane wave with transverse wave vector $\mathbf{q}$, angular frequency ω, and polarization σ. The fourth term between parentheses does not apply to uniform crystals; it only applies to periodically poled crystals where Λ is the poling period. All other symbols are defined in Sec. 4.2.3 of the main text. Equation (4.42) is valid for any type of phase matching as it is based on a simple plane-wave expansion. The Taylor expansion of Eq. (4.43) up to second-order becomes approximately

$$\Delta k_z(\mathbf{q}_1, \mathbf{q}_2) \approx C + \frac{|\mathbf{q}_-|^2}{4n_0\omega_0/c} + \begin{cases} 0 & \text{for noncritical type-I and type-II,} \\ -\rho[\mathbf{q}_+]_y & \text{for critical type-I } (e \rightarrow oo), \\ +\frac{1}{2}\rho[\mathbf{q}_+ - \mathbf{q}_-]_y & \text{for critical type-II } (o \rightarrow oe), \end{cases} \tag{4.44}$$

where C is the wave-vector mismatch in the forward direction, $\mathbf{q}_\pm \equiv \mathbf{q}_1 \pm \mathbf{q}_2$, n_0 is the refractive index at the down-converted frequency, and ρ is the walk-off angle for extraordinary-polarized light ($\rho > 0$ if directed away from the crystallographic optical axis). We have omitted the relatively small direction, frequency, and polarization dependencies of the refractive index in all second-order terms. We have also omitted the frequency dependence of the walk-off angle ρ.

In the noncritically phase-matched case, above equations directly lead to Eqs. (4.8) and (4.9) describing the generated two-photon field profile in the main text of this chapter. We therefore conclude that the analysis in this chapter applies to all noncritically phase-matched SPDC processes. For noncritical type-II phase matching, one can easily add the polarization dependence of the refractive index to the phase-matching profile in Eq. (4.9) of the main text by substituting n_0 for $2n_1n_2/(n_1 + n_2)$, where n_1 and n_2 are the refractive indices of the two down-converted photons.

For critical type-I phase matching, a linear term appears in the wave-vector mismatch in Eq. (4.44). This linear term can be neglected if the pump beam is sufficiently loosely focused; loose focusing causes the momentum representation $\tilde{E}_p(\mathbf{q}_+)$ to become compact such that it over-rules the much broader $\mathbf{q}_+$ dependence of Δk_z in Eq. (4.42). This criterion is met if the walk-off term $\frac{1}{2}L\rho[\mathbf{q}_+]_y$ in the argument of the sinc function is much smaller than a radian at a typical value of $[\mathbf{q}_+]_y = 2/w_p$, where w_p is the width of the Gaussian pump beam in real space and $2/w_p$ is the width of the pump beam in transverse momentum space. The loose-focusing criterion thus becomes $L\rho \ll w_p$ for critical type-I phase matching, simply stating that the transverse walk-off distance $L\rho$ must be much smaller than the pump beam width. In Sec. 4.2.3, we have already assumed loose focusing (Rayleigh range pump $\gg$ crystal length) in order to obtain simple expressions for the engineering parameters in Eqs. (4.14) and (4.18). The loose-focusing criterion $L\rho \ll w_p$ for critical type-I phase matching is generally stronger.

For critical type-II phase matching, the linear term *cannot* be screened by loose focusing. It is immediately clear from Eq. (4.44) that the linear term in $[\mathbf{q}_-]_y$ affects Eq. (4.42) even if the momentum representation $\tilde{E}_p(\mathbf{q}_+)$ is very compact. It is therefore generally not correct to use Eqs. (4.8) and (4.9) for critical type-II SPDC. Note, however, that even in this critical type-II case, our engineering description remains valid if the slits are oriented in the y direction; the linear walk-off term $[\mathbf{q}_-]_y$ becomes irrelevant if the transverse walk-off is directed along the orientation of the slits.

5

Observation of two-photon speckle patterns

We report the observation of speckle patterns in quantum correlations within light that is scattered by a disordered medium. The random medium is illuminated with spatially entangled photon pairs, and fourth-order speckle patterns are spatially resolved by two independently scanning detectors. Spatial entanglement gives two-photon speckle a much richer structure than ordinary one-photon speckle. Our experiments demonstrate that two-photon speckle from a surface scatterer and a volume scatterer look entirely different.

W. H. Peeters, J. J. D. Moerman, and M. P. van Exter, *Observation of two-photon speckle patterns*, Physical Review Letters **104**, 173601 (2010)

5.1 Introduction

Optical speckle is the random interference pattern that is observed when coherent radiation is scattered by a disordered scattering medium. The phenomenon has been studied widely since the invention of the laser [41]. Textbook studies generally consider the scattered intensity, which can be regarded as the one-photon probability density. Recently, the concept of speckle was theoretically extended to the two-photon probability density, which is observable as the coincidence count rate between two detectors [36]. The idea is to illuminate a random medium with spatially entangled photon pairs, produced via spontaneous parametric down-conversion (SPDC) [56, 59, 64, 69], such that a two-photon speckle pattern is formed in the coincidence count rate.

Two-photon speckle is of great interest for the research on multiple scattering of nonclassical waves [36, 135–137]. The coincidence count rate is the key observable when studying entangled states in random media, and two-photon speckle directly visualizes the spatial structure of the entanglement in the scattered light. The subject of two-photon speckle is related to a recent observation of spatial quantum correlations in multiply scattered light [137]. In this observation, however, only the spatially integrated power was measured. Until now, the structure within spatial quantum correlations in multiply scattered light has remained unexplored. Furthermore, two-photon speckle is important for the research on two-photon imaging [52, 66, 78, 114, 138–140], in which random media have not been investigated thus far.

In this chapter we report the experimental observation of two-photon speckle. Spatially entangled photon pairs are scattered of random media, and quantum correlations in the scattered light are spatially resolved by two independently scanning detectors in the far field. First, we introduce a theoretical expression for the autocorrelation function of the two-photon speckle pattern. Second, we present experimental two-photon speckle patterns for surface and volume scatterers, and we demonstrate in which respect they are different. Finally, we discuss requirements for the incident light necessary to generate two-photon speckle.

5.2 Theory

Figure 5.1 schematically depicts the experimental setup. A static linear scattering medium is illuminated with photon pairs that originate from a low-gain SPDC source pumped by a continuous-wave laser with full spatial coherence. Detection occurs quasimonochromatically in the far field of the scatterer in transmission geome-

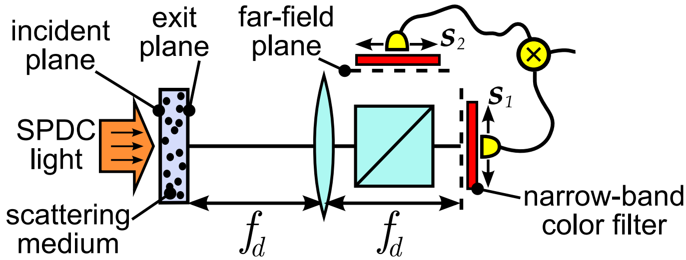

Figure 5.1: Experimental scheme.

try*. Scattered photons are probabilistically separated at a beam splitter, detected by independently scanning single-photon counters, and correlated by coincidence logic.

The transverse spatial properties of a pure spatially entangled photon pair are described by the two-photon probability amplitude† [56]

$$A(\mathbf{x}_1, \mathbf{x}_2) \equiv \langle \mathrm{vac}|\hat{E}^{(+)}(\mathbf{x}_1)\hat{E}^{(+)}(\mathbf{x}_2)|\Psi\rangle, \tag{5.1}$$

where $\hat{E}^{(+)}(\mathbf{x})$ is the positive-frequency electric-field operator at transverse position $\mathbf{x}$. The profile $A(\mathbf{x}_1, \mathbf{x}_2)$ is the complex probability amplitude for simultaneous detection of one photon at transverse position $\mathbf{x}_1$ and the other photon at transverse position $\mathbf{x}_2$. The coincidence count rate between two detectors thus scales as $R(\mathbf{x}_1, \mathbf{x}_2) \propto |A(\mathbf{x}_1, \mathbf{x}_2)|^2$. Below, we refer to $A(\mathbf{x}_1, \mathbf{x}_2)$ and $R(\mathbf{x}_1, \mathbf{x}_2)$ as the two-photon field and two-photon intensity, respectively. We will express the transverse coordinates $\mathbf{s}_{1,2}$ in the far-field plane in terms of angles $\boldsymbol{\theta}_{1,2} \equiv \mathbf{s}_{1,2}/f_d$, where f_d is the focal length of the far-field imaging lens (see Fig. 5.1).

The formation of two-photon speckle in the coincidence count rate occurs via quantum interference in the randomly scattered two-photon field (theory in Ref. [36]). Extending the analysis in Ref. [36], we concentrate on the average two-photon speckle shape, which depends on both detector displacements in the far-field. The speckle shape is contained in the autocorrelation function of the two-photon speckle pattern

$$C(\boldsymbol{\theta}_1, \boldsymbol{\theta}_2; \delta\boldsymbol{\theta}_1, \delta\boldsymbol{\theta}_2) \equiv \overline{R_{\mathrm{FF}}\left(\boldsymbol{\theta}_1^-, \boldsymbol{\theta}_2^-\right) R_{\mathrm{FF}}\left(\boldsymbol{\theta}_1^+, \boldsymbol{\theta}_2^+\right)}, \tag{5.2}$$

* By quasimonochromatic we mean that the optical detection bandwidth $\Delta\nu$ is small in comparison with $\tau_{\mathrm{scat}}^{-1}$, where τ_{scat} is the spread in scattering times. The two-photon speckle contrast is expected to diminish for large bandwidth since the spatial electric-field propagator typically varies over frequency intervals $\tau_{\mathrm{scat}}^{-1}$.

† The sub-picosecond structure in the $t_2 - t_1$ coordinate of the two-photon probability amplitude is left out, because spatial-temporal correlations [64] will be absent within the applied optical detection bandwidth $\Delta\nu$ that is much smaller than the phase-matching bandwidth.

where $R_{\mathrm{FF}}\left(\boldsymbol{\theta}_1, \boldsymbol{\theta}_2\right)$ is the coincidence count rate in the far-field plane, and $\boldsymbol{\theta}_{1,2}^{\pm} \equiv \boldsymbol{\theta}_{1,2} \pm \frac{1}{2}\delta\boldsymbol{\theta}_{1,2}$. The bar denotes averaging over different realizations of disorder.

To arrive at a nice expression for the two-photon speckle autocorrelation function $C(\boldsymbol{\theta}_1, \boldsymbol{\theta}_2; \delta\boldsymbol{\theta}_1, \delta\boldsymbol{\theta}_2)$, we make two assumptions. First, we assume the opening angle of the scattered light to be much wider than the diffraction angles associated with the average two-photon intensity in the exit plane $\overline{R_{\mathrm{ex}}(\mathbf{x}_1, \mathbf{x}_2)}$ (strong-scattering regime). Second, the scattered two-photon field is assumed to exhibit Gaussian statistics*. With these assumptions, Eq. (5.2) can be rewritten as (see appendix 5.8)

$$C(\boldsymbol{\theta}_1, \boldsymbol{\theta}_2; \delta\boldsymbol{\theta}_1, \delta\boldsymbol{\theta}_2) \approx \overline{R_{\mathrm{FF}}(\boldsymbol{\theta}_1, \boldsymbol{\theta}_2)}^2 \left[1 + \left|\mu'(\delta\boldsymbol{\theta}_-, \delta\boldsymbol{\theta}_+)\right|^2\right], \tag{5.3}$$

where the speckle shape function $\mu'(\delta\boldsymbol{\theta}_-, \delta\boldsymbol{\theta}_+)$ is expressed in a rotated basis where $\delta\boldsymbol{\theta}_\pm \equiv \frac{1}{\sqrt{2}}(\delta\boldsymbol{\theta}_1 \pm \delta\boldsymbol{\theta}_2)$. The key result is the speckle shape function

$$\mu'(\delta\boldsymbol{\theta}_-, \delta\boldsymbol{\theta}_+) = \frac{\mathfrak{F}\left[\overline{R'_{\mathrm{ex}}(\mathbf{x}_-, \mathbf{x}_+)}\right]\left(k\delta\boldsymbol{\theta}_-, k\delta\boldsymbol{\theta}_+\right)}{\mathfrak{F}\left[\overline{R'_{\mathrm{ex}}(\mathbf{x}_-, \mathbf{x}_+)}\right](0,0)}, \tag{5.4}$$

where $\mathfrak{F}$ denotes the spatial Fourier transform, and k is the radial wavenumber of a down-converted photon in vacuum. The average two-photon intensity in the exit plane of the scatterer $\overline{R'_{\mathrm{ex}}(\mathbf{x}_-, \mathbf{x}_+)}$ is expressed in a rotated basis where $\mathbf{x}_\pm \equiv \frac{1}{\sqrt{2}}(\mathbf{x}_1 \pm \mathbf{x}_2)$, and $\mathbf{x}_{1,2}$ denote transverse positions of the photons in the exit plane.

The theoretical result in Eqs. (5.3)-(5.4) shows that the average shape of two-photon speckle spots in the far field is Fourier related to the spatial structure of the average two-photon intensity in the exit plane. Note that the two-photon speckle size can be very different along the difference coordinate $\boldsymbol{\theta}_1 - \boldsymbol{\theta}_2$ and the sum coordinate $\boldsymbol{\theta}_1 + \boldsymbol{\theta}_2$. The size of the speckle spots along the difference-coordinate is inversely proportional to the distance between the photons in the exit plane, whereas the size along the sum-coordinate depends on the sum-coordinate of the photons in the exit plane.

Equations (5.3)-(5.4) have a well-known analog in ordinary one-photon speckle. The one-photon speckle theorem assumes spatially coherent illumination, and it states that the shape of one-photon speckle spots in the far field is Fourier related to the average intensity in the exit plane [41]. The analogy is based on similarities between the autocorrelation function of the electric-field amplitude $\overline{E^*(\mathbf{x})E(\mathbf{x}')}$ for the one-photon case and the autocorrelation function of a pure two-photon probability amplitude $\overline{A^*(\mathbf{x}_1, \mathbf{x}_2)A(\mathbf{x}'_1, \mathbf{x}'_2)}$ for the two-photon case†. The latter function

* This assumption is valid for high-dimensional entanglement and becomes approximate for small Schmidt numbers (see Fig. 2 in Ref. [36])

† This analogy is different from a previously investigated duality between the first-order coherence function and the two-photon probability amplitude [78, 138, 139]

is closely related to the two-photon cross-spectral density function [141]. Both functions mathematically denote two-photon field mixtures, either via a quantum average (in Ref. [141]) or via different realizations of disorder (in our case).

5.3 Experimental setup

The experimental setup is depicted in Fig. 5.2. Photon pairs are generated via SPDC in a cw-pumped collinear type-I geometry in a 5-mm-long periodically poled $KTiOPO_4$ crystal (pump 200 mW at 413 nm). The crystal center is imaged onto the incident plane of the scatterer. Detection occurs via projection onto single-mode fibers that are coupled to photon counters and coincidence logic ($\tau_{\mathrm{gate}} = 1.73$ ns). Spatial resolution in the far-field planes is achieved with tight foci of the detection modes ($w_{\mathrm{det}} = 140$ μm). When the fiber holders are scanned transversely, the detection modes move in their far-field planes but remain fixed in the exit plane of the scatterer. The detectors are placed behind narrow band spectral filters such that the experiment operates in the quasimonochromatic regime (5 nm at 826 nm). The figures in this chapter show coincidence count rates that are corrected for accidental coincidence counts. The generated two-photon field for our source is thoroughly analyzed in Refs. [142, 143]. The Schmidt number of the spatial entanglement, which quantifies the effective number of independent spatial modes, is $K \approx 83$ [10].

Our experiments are designed to demonstrate the importance of the Fourier relation for the two-photon speckle shape in Eqs. (5.3)-(5.4). Three different scatter configurations are chosen (see Fig. 5.2). Configurations (a) and (b) represent surface scatterers involving a single diffuser. Configuration (c) mimics a volume scatterer comprising two diffusers positioned in one another's far field. A surface scatterer does not directly affect the transverse position of an incident photon. Hence, the two-photon speckle shape will correspond to the strong positional correlations of the incident light. A volume scatterer, on the other hand, is capable of moving a photon transversely during the photon's propagation from the incident plane to the exit plane. As a consequence, the average positional correlation in the exit plane will be smeared out, and the two-photon speckle shape is expected to be entirely different. This is remarkable, since in the case of ordinary one-photon speckle, speckle spots are identical for surface and volume scatterers [41].

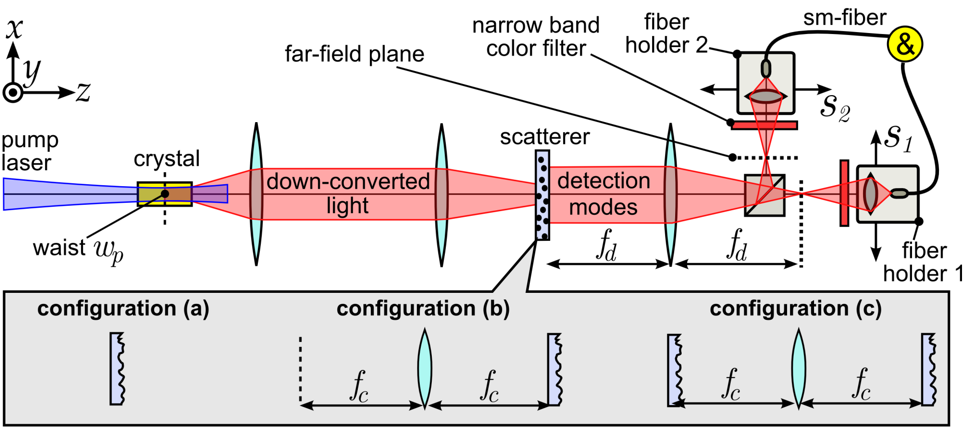

Figure 5.2: Experimental setup. Scattered photons are probabilistically separated at a beam splitter, collected by two single-mode (SM) fibers, and detected by photon counters and coincidence logic. Three scatter configurations can be chosen (a)-(c). The full width at half maximum scattering angle of each diffuser is 22 mrad. *The indicated length scales are* $w_p = 160$ μm, $f_c = 10$ mm, *and* $f_d = 250$ mm.

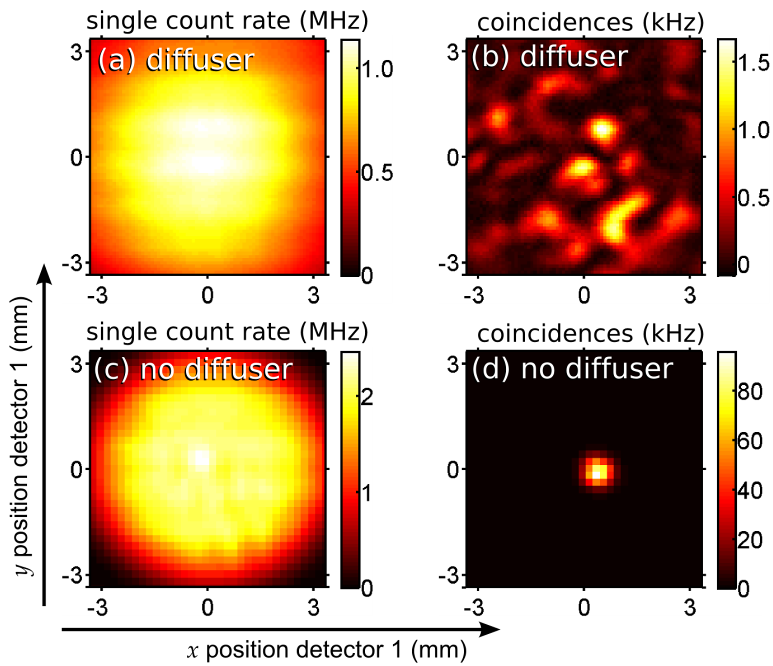

Figure 5.3: (a) Measured single count rate in the far field of a diffuser. (b) Measured coincidence count rate in the same experiment. This two-photon speckle pattern is recorded while keeping the position of detector 2 fixed. Panels (c) and (d) display the reference measurement.

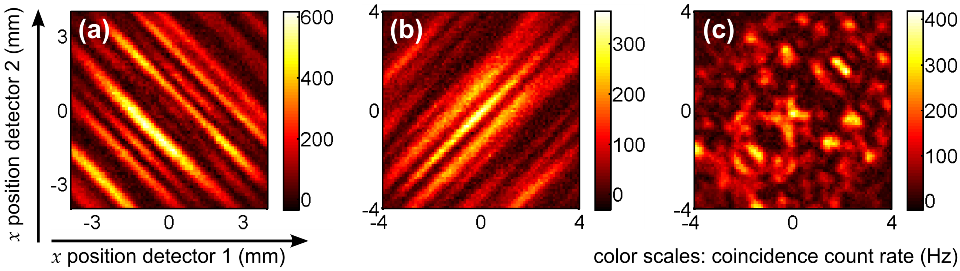

Figure 5.4: Measured two-photon speckle patterns recorded with two independently scanning detectors. The patterns (a)-(c) directly correspond to scattering configurations (a)-(c) in Fig. 5.2.

5.4 Experimental results

First, we discuss an experiment with one scanning and one fixed detector. The experiment is performed in configuration (a) involving a single diffuser. Figures 5.3(a)-(b) show the single count rate and the coincidence count rate, respectively. It is remarkable that speckle is only observed in the coincidence count rate. Because of spatial entanglement, projection of the photon in the fixed detector corresponds to a collapse of the other photon into a speckle pattern. The absence of any ordinary one-photon speckle is consistent with the multimode character of the entangled SPDC light. The reference experiment, in the absence of scattering, is displayed in Figs. 5.3(c)-(d). The sharp peak in the coincidence count rate locates the mirrored position of detector 2.

Second, we discuss experiments where the positions of *both* detectors are scanned independently in a horizontal line (see Fig. 5.4). Only by scanning them both, one gains knowledge about the size of the two-photon speckle spots along both the difference coordinate and the sum coordinate. The two-photon speckle patterns in Figs. 5.4 (a)-(c) correspond to the three scattering configurations in Fig. 5.2. All patterns obey mirror symmetry with respect to the diagonal due to the indistinguishability of the photons. Remarkable is the fact that the three patterns look entirely different. The two-photon speckle spots are strongly elongated for the single diffuser [Figs. 5.4(a) and 5.4(b)] while the spots are almost isotropic for the volume scatterer [Figs. 5.4(c)].

In configuration (a) the two-photon source itself is imaged onto the diffuser. The two photons arrive at approximate equal positions on the diffuser since they are created in that way inside the nonlinear crystal. The two-photon intensity is thus tight along the difference coordinate in the plane of the diffuser. In agreement with the Fourier relationship in Eq. (5.4), two-photon speckle in Fig. 5.4(a) appears elongated along the difference coordinate. In configuration (b) the far field of the two-photon source is imaged onto the diffuser, and the photons have approximately opposite transverse positions. Accordingly, we observe two-photon speckle spots that are elongated along the sum coordinate in Fig. 5.4(b). In configuration (c) the second diffuser is illuminated with far-field patterns similar to Fig. 5.4 (a). The average two-photon intensity is now wide in both x_+ and x_- directions. In accordance, we observe two-photon speckle spots in Fig. 5.4(c) that are small along both diagonal coordinates.

The orientation of the speckle spots in Figs. 5.4(a)-(b) and the isotropy in Fig. 5.4(c) can be qualitatively understood via the Klyshko picture of two-photon imaging [52, 71]. This interpretation follows one detected photon backwards in time to be converted into the second forward-propagating photon via a virtual reflection at the nonlinear crystal. However, a quantitative understanding of the two-photon speckle size requires detailed knowledge of the spatial and angular limitations of the generating process [56, 69]; i.e., one needs the explicit expression for the generated two-photon field for our source [142, 143].

We now discuss a quantitative analysis of the two-photon speckle size for configuration (a). Seven experimental speckle patterns yield average speckle sizes of (0.44 ± 0.05) and (4.4 ± 0.2) mm along the sum diagonal and difference diagonal, respectively. The theoretical values are 0.41 and 5.4 mm as calculated from Eqs. (5.3)-(5.4) and the generated two-photon field [142, 143]. The confined dimension is in excellent agreement with theory while the elongated size is slightly smaller than expected. We attribute this small disagreement to the fact that our experiment does not fully operate in the strong-scattering regime assumed in Eqs. (5.3)-(5.4).

5.5 Discussion

Two-photon speckle becomes interesting only if the incident light contains multimode spatial correlations. If the incident light were in a single spatial mode, any scattered two-photon speckle pattern would factorize into the one-photon intensities via $R(\boldsymbol{\theta}_1, \boldsymbol{\theta}_2) \propto I(\boldsymbol{\theta}_1)I(\boldsymbol{\theta}_2)$. This pattern obviously contains the same information as the intensity pattern $I(\boldsymbol{\theta})$.

Correlations in thermal light cannot generate the nonfactorizable features in Fig. 5.4. Thermal correlations are phase insensitive and are not affected by a diffuser [66]. This is easily understood via the Klyshko-type picture for phase-insensitive correlations, in which the crystal is replaced by a phase-conjugate mirror instead of a real mirror [140]. Two-photon speckle is thus essentially different from ghost imaging because the latter works fine with thermal light [138, 144]. The difference stems from the fact that in our scheme *both* photons pass through the sample, whereas in ghost imaging, one of the photons propagates through an empty reference arm. The features in Fig. 5.4 require phase-sensitive correlations in the incident light [66]. These correlations are commonly generated via the nonlinear process of SPDC and are not present in thermal light. Our experiments are performed with nonclassical light where subsequent entangled photon pairs can be temporally resolved [66].

The presence of the nonfactorizable features in Fig. 5.4 demonstrates that two-photon speckle has a richer structure than ordinary one-photon speckle. Because of the spatial entanglement between the photons, projection of one of the photons corresponds to a full collapse of the other photon into a speckled mode profile [see Fig. 5.3(b)]. The dimensionality of the entanglement quantifies the effective number of different projected one-photon speckle patterns. If someone wishes to generate all these speckle patterns with a coherent laser beam, she or he will have to adjust the mode profile of the incident beam many times. Spatial entanglement allows one to obtain many projected one-photon speckle patterns *without* changing the geometry of the incident light.

5.6 Conclusion

We have observed two-photon speckle patterns in the far-field of disordered scattering media. Spatial entanglement of the incident light gives two-photon speckle a much richer structure than ordinary one-photon speckle. Our work paves the way for future research on multiple scattering of entangled photons. It would be interesting to establish the connection with universal conductance fluctuations [44] and enhanced backscattering of light [42].

5.7 Acknowledgements

We thank J. P. Woerdman, T. Kauffmann, and H. Di Lorenzo Pires for useful discussions. This research was supported by the Dutch Science Foundation NWO/FOM and the EU under the FET-Open Agreement “HIDEAS” No. FP7-ICT-221906.

5.8 APPENDIX: Derivation of the two-photon speckle autocorrelation function

This appendix presents a derivation of Eqs. (5.3)-(5.4) in the main text of this chapter. Inspired by one-photon speckle analysis [41], we approximate the autocorrelation function of the two-photon field in the exit plane of the scatterer by a quasihomogeneous function [145]. In such a form the autocorrelation function separates into a wide function of the average coordinate and a narrow function of the difference coordinate, i.e.,

$$\begin{aligned}\Gamma_{\mathrm{ex}}\left(\mathbf{x}_1,\mathbf{x}_2;\delta\mathbf{x}_1,\delta\mathbf{x}_2\right) &\equiv \overline{A^*_{\mathrm{ex}}\left(\mathbf{x}_1^-,\mathbf{x}_2^-\right)A_{\mathrm{ex}}\left(\mathbf{x}_1^+,\mathbf{x}_2^+\right)}\\ &\approx \overline{R_{\mathrm{ex}}(\mathbf{x}_1,\mathbf{x}_2)}\times f_{\mathrm{ex}}(\delta\mathbf{x}_1,\delta\mathbf{x}_2),\end{aligned} \tag{5.5}$$

where $\mathbf{x}^{\pm}_{1,2}\equiv\mathbf{x}_{1,2}\pm\frac{1}{2}\delta\mathbf{x}_{1,2}$, $A_{\mathrm{ex}}(\mathbf{x}_1,\mathbf{x}_2)$ is the two-photon field in the exit plane of the scatterer, and $\overline{R_{\mathrm{ex}}(\mathbf{x}_1,\mathbf{x}_2)}$ is the average two-photon intensity in the exit plane. The compact function $f_{\mathrm{ex}}(\delta\mathbf{x}_1,\delta\mathbf{x}_2)$ is related to the opening angle of the scattered light. We associate this approximation with strongly scattering surfaces with large surface height fluctuations ($\gg\lambda$) and a transverse correlation of the surface roughness that is short as compared to the structure in the average two-photon intensity (strong-scattering regime).

Next, we propagate Γ_{ex} to the far-field plane to obtain Γ_{FF} being the two-photon field correlation function in the far-field plane. Spatial propagation of a two-photon field is described by applying the electric field propagator to each coordinate individually, yielding [78]

$$A_{\mathrm{FF}}(\mathbf{s}_1,\mathbf{s}_2)=\int d\mathbf{x}_1 d\mathbf{x}_2 h(\mathbf{s}_1,\mathbf{x}_1)h(\mathbf{s}_2,\mathbf{x}_2)A_{\mathrm{ex}}(\mathbf{x}_1,\mathbf{x}_2), \tag{5.6}$$

where $\mathbf{s}_{1,2}$ are the transverse positions in the far-field plane and

$$h(\mathbf{s},\mathbf{x})=\frac{k}{2\pi i f_d}\exp\left(-ik\frac{\mathbf{s}\cdot\mathbf{x}}{f_d}\right), \tag{5.7}$$

is the far-field propagator of the electric field, f_d is the focal length of the far-field imaging lens, and k is the radial wavenumber of a down-converted photon in vacuum. By combining Eqs. (5.5)-(5.7) one obtains the two-photon field correlation function in the far-field plane

$$\begin{aligned}\Gamma_{\mathrm{FF}}(\mathbf{s}_1,\mathbf{s}_2;\delta\mathbf{s}_1,\delta\mathbf{s}_2) &= \left(\frac{k}{2\pi f_d}\right)^4\mathfrak{F}\left[\overline{R_{\mathrm{ex}}(\mathbf{x}_1,\mathbf{x}_2)}\right]\left(k\frac{\delta\mathbf{s}_1}{f_d},k\frac{\delta\mathbf{s}_2}{f_d}\right)\\ &\quad\times\mathfrak{F}\left[f_{\mathrm{ex}}(\delta\mathbf{x}_1,\delta\mathbf{x}_2)\right]\left(k\frac{\mathbf{s}_1}{f_d},k\frac{\mathbf{s}_2}{f_d}\right),\end{aligned} \tag{5.8}$$

where $\mathfrak{F}$ denotes spatial Fourier transform. This correlation function has a similar separable form as Eq. (5.5).

Finally, we assume Gaussian statistics of the two-photon field in the far-field of the scatterer. This assumption requires high-dimensional entanglement of the input field; it becomes approximate for small Schmidt numbers (see Fig. 2 in Ref. [36]). The complex Gaussian moment theorem [41] now yields an expression for the desired coincidence correlation function C in terms of Γ_{FF}

$$\begin{aligned} C(\mathbf{s}_1, \mathbf{s}_2; \delta\mathbf{s}_1, \delta\mathbf{s}_2) &= \overline{R_{\mathrm{FF}}(\mathbf{s}_1^-, \mathbf{s}_2^-)} \times \overline{R_{\mathrm{FF}}(\mathbf{s}_1^+, \mathbf{s}_2^+)} + |\Gamma_{\mathrm{FF}}\,(\mathbf{s}_1, \mathbf{s}_2; \delta\mathbf{s}_1, \delta\mathbf{s}_2)\,|^2 \\ &\approx \overline{R_{\mathrm{FF}}(\mathbf{s}_1, \mathbf{s}_2)}^2 + |\Gamma_{\mathrm{FF}}\,(\mathbf{s}_1, \mathbf{s}_2; \delta\mathbf{s}_1, \delta\mathbf{s}_2)\,|^2, \end{aligned} \tag{5.9}$$

where $\mathbf{s}_{1,2}^{\pm} \equiv \mathbf{s}_{1,2} \pm \frac{1}{2}\delta\mathbf{s}_{1,2}$, and where we once more used strong scattering in the second line.

By inserting Eq. (5.8) for Γ_{FF} we find

$$C(\mathbf{s}_1, \mathbf{s}_2; \delta\mathbf{s}_1, \delta\mathbf{s}_2) = \overline{R_{\mathrm{FF}}(\mathbf{s}_1, \mathbf{s}_2)}^2 \left[1 + \left|\mu'(\delta\mathbf{s}_-, \delta\mathbf{s}_+)\right|^2\right], \tag{5.10}$$

and $\delta\mathbf{s}_{\pm} \equiv \frac{1}{\sqrt{2}}(\delta\mathbf{s}_1 \pm \delta\mathbf{s}_2)$ and where the shape function

$$\mu'(\delta\mathbf{s}_-, \delta\mathbf{s}_+) = \frac{\mathfrak{F}\left[\overline{R'_{\mathrm{ex}}(\mathbf{x}_-, \mathbf{x}_+)}\right]\left(k\dfrac{\delta\mathbf{s}_-}{f_d}, k\dfrac{\delta\mathbf{s}_+}{f_d}\right)}{\mathfrak{F}\left[\overline{R'_{\mathrm{ex}}(\mathbf{x}_-, \mathbf{x}_+)}\right](0,0)}, \tag{5.11}$$

is Fourier related to the average two-photon intensity in the exit plane $\overline{R'_{\mathrm{ex}}(\mathbf{x}_-, \mathbf{x}_+)}$, expressed in a rotated basis where $\mathbf{x}_{\pm} \equiv \frac{1}{\sqrt{2}}(\mathbf{x}_1 \pm \mathbf{x}_2)$. Equations (5.10)-(5.11) become Eqs. (5.3)-(5.4) in the main text after a simple conversion to angles.

In the above derivation of the correlation functions, we neglected the effect of the symmetry constraint of the two-photon field $A_{\mathrm{ex}}(\mathbf{x}_1, \mathbf{x}_2) = A_{\mathrm{ex}}(\mathbf{x}_2, \mathbf{x}_1)$. This symmetry results in average photon bunching close to the diagonal $\mathbf{s}_1 \approx \mathbf{s}_2$. The approximation is allowed since the number of spatial modes is sufficiently large for the considered case of strong scattering and high-dimensional entanglement. In this regime, the vast majority of the two-photon speckle spots is located far away from the diagonal, where $\mathbf{s}_1 \neq \mathbf{s}_2$ and the effect of photon bunching is not relevant.

6

Spatial pairing and antipairing of photons in random media

We experimentally demonstrate spatial pairing and spatial antipairing of two entangled photons after propagation through a randomly scattering medium. This two-photon interference phenomenon survives averaging over different realizations of disorder. Despite the random nature of the scattering process, the labeled photons have a natural tendency to cluster together or to avoid each other depending of the symmetry properties of the entanglement. Our experimental results are in excellent agreement with our scattering model based on the random unitary matrix ensemble. The (anti)-pairing behavior is closely related to particle exchange symmetries: pairing for bosonic symmetry, antipairing for fermionic symmetry, and anything in between for anyonic symmetry.

6.1 Introduction

In the previous chapter, we analyzed the spatial structure in individual two-photon speckle patterns. These speckle patterns are visible for single realizations of the scattering medium that is illuminated with a spatially entangled two-photon state. Thus far, we have not yet discussed the scattered two-photon probability density *after* averaging over different realizations of disorder. It is in particular interesting to study the effect of two-photon particle symmetry $A(\mathbf{x}_1, \mathbf{x}_2) = A(\mathbf{x}_2, \mathbf{x}_1)$ on the ensemble-averaged two-photon probability density, since the scattered two-photon probability amplitude needs to obey this symmetry in *each* realization of disorder.

To study the essence of the two-photon symmetry, it is desired to have a physical system that allows tuning of the symmetry properties. In other words, it is desired that there is no particle exchange constraint to $A(\mathbf{x}_1, \mathbf{x}_2)$ at all. To achieve this, we must design the physical system in which photon 1 and photon 2 are labeled, either via their energies or via their polarizations. This labeling relieves the symmetry constraint because the two spatial coordinates of $A(\mathbf{x}_1, \mathbf{x}_2)$ now refer to distinguishable photons that are individually addressable via their energy or polarization. To study how symmetry affects two-photon scattering, the scattering process should not modify the labeling degree of freedom of the photons, and the spatial scatter matrix should be identical for the two photons. These constraints on the scattering process are quite stringent, but, as we shall demonstrate, such a scattering system is experimentally feasible.

In this chapter, we study the ensemble-averaged spatial density matrix of the multiply-scattered entangled photon pair. We find that the probability density contains spatial structure depending on the symmetry properties of the incident photon pair. The two photons exhibit a tendency to cluster together (pairing) for bosonic spatial symmetry or to avoid each other (antipairing) for fermionic spatial symmetry. We use the terminology (anti-)pairing instead of (anti-)bunching, because the two photons never occupy the same optical mode due to their orthogonal labels. In Sec. 6.2 we provide a theoretical model based on the random unitary matrix ensemble. Section 6.3 describes experiments in which photon pairing and antipairing is observed. Finally, Secs. 6.4-6.5 contain a concluding discussion and a discussion on potential future research.

6.2 Random unitary scattering of labeled photons

In this section we provide a basic two-photon scattering model describing photon pairing and antipairing after random unitary propagation. We start with a pure quasimonochromatic two-photon state

$$|\Psi_{\rm in}\rangle = \sum_{k=1}^{M}\sum_{l=1}^{M} A_{kl}\hat{a}_k^\dagger \hat{b}_l^\dagger |{\rm vac}\rangle, \tag{6.1}$$

where $\hat{a}_i^\dagger$ and $\hat{b}_i^\dagger$ are photon creation operators of photons with identical spatial profiles i but with orthogonal polarization or energy. The number $M \geq 2$ quantifies the dimensionality of the spatial basis for each photon. The two photons are labeled via their polarization or energy. Therefore, we may also write state Eq. (6.1) in particle notation

$$|\Psi_{\rm in}\rangle = \sum_{k=1}^{M}\sum_{l=1}^{M} A_{kl}|k\rangle_1 \otimes |l\rangle_2, \tag{6.2}$$

where $|k\rangle_1$ denotes the spatial k-state of the photon with label 1, and $|l\rangle_2$ denotes the spatial l-state of the photon with label 2. Normalization of the input state requires

$$\sum_{k=1}^{M}\sum_{l=1}^{M} |A_{kl}|^2 = 1. \tag{6.3}$$

The notation chosen in Eq. (6.2) directly shows how $|\Psi_{\rm in}\rangle$ can be spatially entangled for properly chosen A_{kl}. State $|\Psi_{\rm in}\rangle$ is entangled if it is impossible to write Eq. (6.2) in a separable form.

The incident two-photon state will now undergo a quasimonochromatic, linear, and lossless scattering process. We put two extra restrictions on this scattering process:

(1) The spatial scattering process does not affect the labeling property of the photons.
(2) The spatial scattering matrix is identical for the two photons.

Under condition (1), the two photons remain distinguishable via their label throughout the scattering process. By also obeying condition (2), we can use the same unitary (=energy-conserving) spatial scattering matrix u_{ij} for photon 1 and photon 2. We calculate the scattered output state via a coupling of modes formalism

$$\begin{cases} \hat{c}_i = \sum_{j=1}^{M} u_{ij}\hat{a}_j \\ \hat{d}_i = \sum_{j=1}^{M} u_{ij}\hat{b}_j \end{cases} \iff \begin{cases} \hat{a}_j^\dagger = \sum_{i=1}^{M} u_{ij}\hat{c}_i^\dagger \\ \hat{b}_j^\dagger = \sum_{i=1}^{M} u_{ij}\hat{d}_i^\dagger \end{cases} \tag{6.4}$$

where we used unitarity of u_{ij}, and where $\hat{c}_i$ and $\hat{d}_i$ are photon annihilation operators in the output mode space of photon 1 and photon 2, respectively.

By substituting Eq. (6.4) into Eq. (6.1) we obtain the scattered output state

$$|\Psi_{\text{out}}\rangle = \sum_{k=1}^{M}\sum_{l=1}^{M}\sum_{m=1}^{M}\sum_{p=1}^{M} A_{kl}u_{mk}u_{pl}\hat{c}_m^\dagger \hat{d}_p^\dagger|\text{vac}\rangle, \tag{6.5}$$

The aim is to perform averaging over different realizations of disorder. Therefore, it is most suitable to describe the ensemble-averaged scattered light as a mixed state with density operator

$$\hat{\rho}^{(\text{out})} \equiv \overline{|\Psi_{\text{out}}\rangle\langle\Psi_{\text{out}}|}, \tag{6.6}$$

where the bar denotes averaging over different realizations of disorder. For notational convenience we will express the density operator in a density-matrix form

$$\hat{\rho}^{(\text{out})} = \sum_{q=1}^{M}\sum_{r=1}^{M}\sum_{q'=1}^{M}\sum_{r'=1}^{M} \rho^{(\text{out})}_{qr,q'r'}\hat{c}_q^\dagger \hat{d}_r^\dagger|\text{vac}\rangle\langle\text{vac}|\hat{d}_{r'}\hat{c}_{q'} \tag{6.7}$$

$$\rho^{(\text{out})}_{qr,q'r'} = \langle\text{vac}|\hat{d}_r\hat{c}_q\hat{\rho}^{(\text{out})}\hat{c}_{q'}^\dagger\hat{d}_{r'}^\dagger|\text{vac}\rangle, \tag{6.8}$$

where we used the completeness and orthonormality of the two-photon basis states $\hat{c}_q^\dagger\hat{d}_r^\dagger|\text{vac}\rangle$. By combining Eqs. (6.8), (6.6), and (6.5) we find the density matrix of the scattered two-photon state

$$\rho^{(\text{out})}_{qr,q'r'} = \sum_{k=1}^{M}\sum_{l=1}^{M}\sum_{k'=1}^{M}\sum_{l'=1}^{M} A_{kl}A^*_{k'l'}\overline{u_{qk}u_{rl}u^*_{q'k'}u^*_{r'l'}}. \tag{6.9}$$

In order to perform ensemble averaging, we must choose an ensemble of unitary scattering matrices. In many realistic multiple scattering geometries, the matrix ensemble contains several correlations such as enhanced backscattering [42] and universal conductance fluctuations [44]. We will however omit all these correlations by using the random unitary matrix ensemble, also known as the circular unitary ensemble (CUE)*. This ensemble is implicitly defined via invariant integration over the unitary group [147, 148], which means that any integral over the ensemble is not affected by multiplication of the ensemble with any unitary matrix of choice (see Eq. (21) in Ref. [148]). In a sense, the random unitary matrix ensemble is the most random ensemble imaginable, since it remains unchanged after multiplication by any unitary matrix. At this point, the choice of the CUE is useful because it is

* For example, enhanced backscattering is contained in the circular orthogonal ensemble (COE) for the reflection matrix r, which means that $r = UU^T$ with U in the CUE [146]. The circular orthogonal ensemble obeys $\overline{|r_{ii}|^2} = 2\overline{|r_{ij}|^2}$ for $i \neq j$.

likely that any two-photon interference phenomenon surviving this type of ensemble averaging will also survive in realistic scattering geometries.

By using this additional assumption of the random unitary matrix ensemble, we have derived explicit expressions (see Appendix) for the ensemble-averaged scattered two-photon density matrix in Eq. (6.9). We find that the two photons have a tendency to either pair up or to avoid each other, depending on the symmetry properties of the entanglement. The degree of pairing in the output can be quantified in a single ratio

$$\mathcal{F} \equiv \frac{\rho^{(\text{out})}_{11,11}}{\rho^{(\text{out})}_{12,12}}, \tag{6.10}$$

which we will call the *pairing factor*. The pairing factor is the two-photon detection probability observed with two detectors looking into the same spatial channel divided by the two-photon detection probability observed with two detectors looking into different spatial channels. The key result of the calculation in the Appendix is that $\mathcal{F} \in [0, 2]$ is

$$\mathcal{F} = \frac{1 + \mathcal{S}}{1 + \dfrac{1 - \mathcal{S}}{M - 1}}, \tag{6.11}$$

where the *symmetry parameter* $\mathcal{S} \in [-1, 1]$ defined as

$$\mathcal{S} \equiv \sum_{k=1}^{M} \sum_{l=1}^{M} A_{kl} A^*_{lk}, \tag{6.12}$$

quantifies the degree of spatial symmetry in the incident two-photon state. For large scattering matrices ($M \gg 2$) the pairing factor in Eq. (6.11) reduces to $\mathcal{F} = 1 + \mathcal{S}$.

It is intriguing that the phenomenon of (anti-)pairing survives averaging over the random unitary ensemble. The direct dependence of $\mathcal{F}$ on $\mathcal{S}$ in Eq. (6.11) implies that the symmetry parameter $\mathcal{S}$ is conserved under scattering for any realization of the unitary matrix. We recall that the photons must retain their labeling parameter throughout the scattering process and that the scatter matrix should be identical for both photons. In scattering geometries that do not obey these restrictions, the photons might bunch into the same mode (same energy and polarization), or the two photons could encounter different scattering matrices such that $\mathcal{S}$ is not conserved anymore.

We now discuss four classes of symmetry that could be imposed on coefficients A_{kl} of the incident two-photon state $|\Psi_{\text{in}}\rangle$. These four symmetry classes are listed in Tab. 6.1. Each symmetry class corresponds to a certain symmetry parameter $\mathcal{S}$ and thus to a certain degree of pairing $\mathcal{F}$ via Eq. (6.11). We have denoted the first three symmetries as bosonic, fermionic and anyonic, because of their clear connection with particle exchange symmetries in bosonic, fermionic and anyonic [149]

symmetry name	restriction on A_{kl}	symmetry parameter $\mathcal{S}$
bosonic symmetry	$A_{kl} = A_{lk}$	$\mathcal{S} = 1$
fermionic symmetry	$A_{kl} = -A_{lk}$	$\mathcal{S} = -1$
anyonic symmetry [149]	$A_{k \geq l,l} = e^{i\theta} A_{lk}$	$\mathcal{S} = \cos(\theta)$
zero symmetry	$A_{k \geq l,l} = 0$	$\mathcal{S} = 0$

Table 6.1: Definitions of four classes of symmetries, which can exist in the entangled two-photon state in Eq. (6.1). The symmetry parameter $\mathcal{S}$ is defined in Eq. (6.12). This parameter plays a central role because it is directly related to the pairing factor $\mathcal{F}$ in Eqs. (6.10)-(6.11).

quantum fields. This connection becomes clear in the particle notation of $|\Psi_{\text{in}}\rangle$ in Eq. (6.2). This notation is mathematically equivalent to the first-quantization language*, which can be used for most quantum fields. When using this language for a certain quantum field, one must manually symmetrize the pre-factors to achieve the desired particle exchange symmetry [150]. The symmetry rules for bosonic, fermionic, and anyonic quantum fields, are identical to the restrictions on A_{kl} that are listed in Tab. 6.1. This justifies the names that we have chosen for the different kinds of symmetry in A_{kl}.

If bosonic symmetry is imposed, the labeled photons have a tendency to pair up in the random medium ($\mathcal{S} = 1$ and $\mathcal{F} = 2$). In case of fermionic symmetry, the labeled photons will never scatter into identical spatial mode profiles ($\mathcal{S} = -1$ and $\mathcal{F} = 0$). Remarkably, the labeled photons exhibit similar behavior as true bosons (bunching) or true fermions (antibunching) depending on the imposed class of symmetry. This similarity arises from the full mathematical equivalence between the particle notation of the labeled photons in Eq. (6.2) and the first-quantization language that can be applied to true bosonic and fermionic quantum fields. Interestingly, our labeled photons allow anyonic symmetry as well. For this symmetry, we expect behavior somewhere in between full pairing and full antipairing ($-1 < \mathcal{S} < 1$ and $0 < \mathcal{F} < 2$). Finally, one could also impose no symmetry at all, which we call zero symmetry ($A_{k \geq l,l} = 0$, $\mathcal{S} = 0$, and $\mathcal{F} = 1$). This option mimics scattering of classical particles, where each particle carries an intrinsic identity label.

6.3 Experiments

6.3.1 Experimental scheme

In this section we describe an experimental scheme for the demonstration of two-photon pairing and antipairing of multiply-scattered polarization-labeled photons.

* The first-quantization language is a quantum-mechanical description of elementary particles in terms of wave functions for each particle. This language does not use creation and annihilation operators.

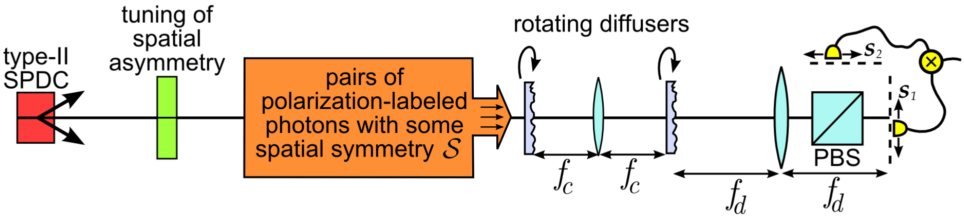

Figure 6.1: Scheme of the experimental process. Polarization-labeled photons are produced via type-II SPDC. The spatial scatter properties of the diffusers are polarization independent, and the diffusers do not affect the polarization. Scattered photons are deterministically separated at a polarizing beam splitter (PBS), detected by independently scanning detectors, and correlated by coincidence logic. Averaging over different realizations of disorder is achieved by fast rotation of the diffusers around the optical axis.

The two-photon interference phenomenon of Eq. (6.11) will be demonstrated for bosonic symmetry ($\mathcal{S} = 1$) and fermionic symmetry ($\mathcal{S} = -1$) in a scattering geometry with a large dimension ($M \gg 2$). The theoretical description is only valid within certain physical conditions of the scattering process. We will address how these conditions are implemented experimentally.

Figure 6.1 schematically depicts the scattering process. The photon pairs are generated via type-II spontaneous parametric down-conversion (SPDC), which produces pairs of polarization-labeled photons [56, 59, 64, 69]. Spatial correlations between the photons arise from conservation of transverse momentum in the down-conversion process. The spatial symmetry parameter $\mathcal{S}$ is tuned by inserting birefringent plates in the far field of the SPDC process (see Sec. 6.3.2 for details*).

In order to demonstrate Eq. (6.11), the scattering process is not allowed to affect the labeling parameter of the photons, which in our case is the polarization. The spatial scattering properties must be identical for both photons. These conditions are met by considering paraxial scattering of diffusers. The random unitary ensemble is approximated with two diffusers positioned in one another's far field and detection in the far field of the second diffuser. Averaging over different realizations of disorder is achieved by relatively fast rotation of the diffusers (see below). The photons are deterministically separated at a beam splitter. The two detectors effectively look at the same spatial profile if the position of detector 2 coincides with the reflected position of detector 1.

* Only the implementation of bosonic and fermionic symmetry is discussed in Sec. 6.3.2. Anyonic symmetry can be straightforwardly implemented by using different wave plates in the anti-symmetrizer in Fig. 6.3. Zero symmetry can be implemented by adding a combination of a polarizer at 45° and a $\lambda/4$-plate at 0° in between the generating crystal and the anti-symmetrizer.

6.3.2 Details of experimental apparatus

The experimental apparatus is schematically depicted in Fig. 6.2. Photon pairs are generated via type-II collinear spontaneous parametric down-conversion (SPDC) in a 5-mm-long periodically poled $KTiOPO_4$ (PPKTP) crystal. The orientation of the crystallographic x, y, and z axes of the PPKTP is indicated in the figure. Down-conversion is operated with a y-polarized pump beam (200 mW at 413.1 nm); the down-converted photons are y and z polarized. Periodic poling is applied along the $\pm z$ axis of the crystal with poling period 11.525 μm along the x axis. The effective nonlinearity, corrected for first-order quasi phase matching, is $(2/\pi)d_{24} = 2.5$ pm/V [111]. This is 4 times less as compared to the nonlinearity in type-I SPDC where the d_{33} of KTP is utilized. Collinear degenerate phase-matching is achieved at $T = 16°$C.

Detection occurs behind narrow band color filters with a full-width-at-half-maximum spectral width of 1 nm around a center wavelength of 826.2 nm. This optical detection bandwidth is below the phase-matching bandwidth* of 1.14 nm. This is required for obtaining an almost spatially pure post-selected two-photon field, after having traced out the subpicosecond structure in its $t_2 - t_1$ coordinate [64]. Spatial purity is required for the generation of high visibility two-photon speckle patterns in experiments with nonrotating diffusers [36]. The spatial properties of the generated two-photon field are practically identical to these of the two-photon field studied in Chapters 4 and 5 because the crystal length, pump beam, and refractive indices are almost identical. Similar two-photon fields have been studied in Refs. [142, 151, 152].

The pump beam is loosely focussed in the crystal-center plane such that the Rayleigh range of the pump beam is much larger than the crystal length (waist $w_p = 160\,\mu$m and Rayleigh range $z_R = \pi w_p^2/\lambda = 20$ cm). Two lenses ($f_a = 200$ mm) in a telescopic configuration directly image the crystal center onto the scattering system.

The scattering system consists of two diffusers that are positioned in one another's far field. Each diffuser is positioned off-center (displaced by 1 cm) such that rotating the diffusers at 15°/s causes good ensemble averaging within the integration time of $12 - 14$ s. Several hundreds of different two-photon speckle spots are being averaged within the integration time of the measurement. The full-width-half-

* The mentioned phase-matching bandwidth $\Delta\lambda = 1.14$ nm is much smaller than the phase-matching bandwidth for type-I SPDC discussed in Chapter 3. This is because the two photons now have orthogonal polarizations and thus propagate with different refractive indices. In the type-II case, the phase-matching bandwidth (FWHM) is calculated from $\Delta\lambda = \lambda_0^2 \Delta\omega/2\pi c$ and the criterion $\mathrm{sinc}^2\left[\frac{L\Delta\omega}{4}\frac{\mathrm{d}}{\mathrm{d}\omega}\left[(n_z(\omega) - n_y(\omega))\omega/c\right]_{\omega=\omega_0}\right] = \frac{1}{2}$, where L is the crystal length, and λ_0 and ω_0 correspond to the vacuum wavelength and angular frequency of a down-converted photon, respectively. The frequency dependent refractive indices of KTP are taken from the Sellmeier dispersion equations in Refs. [106, 107].

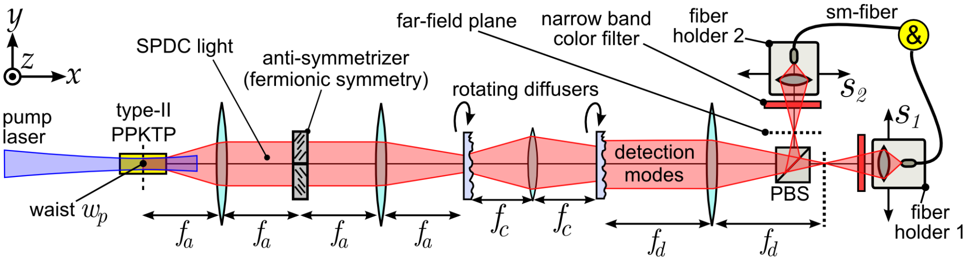

Figure 6.2: Experimental apparatus. Scattered photons are deterministically separated at a polarizing beam splitter (PBS), collected by single mode fibers, and detected by photon counters and coincidence logic. The polarization-labeled photons originate from type-II SPDC having bosonic spatial symmetry. Fermionic spatial symmetry is achieved by adding the anti-symmetrizer (see Fig. 6.3).

maximum scattering angle of each diffuser is 22 mrad. The focal length $f_c = 10$ mm of the lens in between the diffusers is chosen such that the irradiated areas on both diffusers are approximately the same. This is not a strict requirement but merely a convenient choice in relation to the number of speckles and the expected signal to noise ratio.

Behind the scattering system, the two polarization-labeled photons are deterministically separated with a polarizing beam splitter. Detection occurs via projection onto single-mode fibers that are coupled to photon counters and coincidence logic ($\tau_{\text{gate}} = 1.73$ ns). The far-field plane is located in the focal plane of a lens with focal length $f_d = 250$ mm. Spatial resolution in the far-field planes is achieved with tight foci of the detection modes ($w_{\text{det}} = 140$ μm). When the fiber holders are scanned transversely, the detection modes move in their far-field planes but remain fixed in the plane the second diffuser.

An important element of the setup is the "anti-symmetrizer" depicted in Fig. 6.3. When this element is positioned in the far field of the nonlinear crystal it changes the spatial symmetry of the two-photon field from bosonic to fermionic. The anti-symmetrizer consists of two $\lambda/4$-plates closely aligned next to each other (gap is $5 - 15$ μm), and one plate is rotated 90° with respect to the other. The fast and slow axes of the birefringent plates must be oriented parallel to the y and z axes of the coordinate system (defined by the nonlinear crystal). As the photons leave the crystal with approximately opposite transverse momenta, they will generally pass through opposite sides of the anti-symmetrizer. Anti-symmetrization occurs because the phase of the two-photon transmission channel "H-photon left, V-photon right" is $2 \times 90° = 180°$ different from the phase of the two-photon transmission channel "V-photon left, H-photon right". The performance of the anti-symmetrizer is limited by the imperfect angular correlations between the photons, which in turn

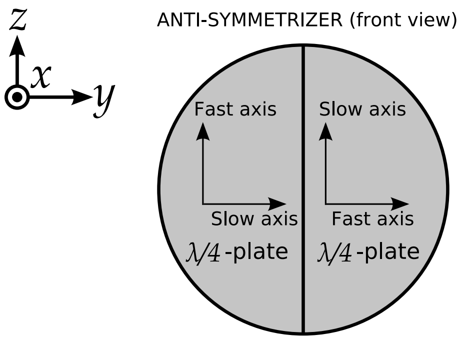

Figure 6.3: Front view of the anti-symmetrizer present in the experimental setup in Fig. 6.2. The orientation in the experimental setup is such that the coordinate system in this figure coincides with the coordinate system in Fig. 6.2.

are limited by the divergence of the pump beam. The probability that both photons pass through the same side must be sufficiently low; the symmetry is only changed when the two photons pass though opposite sides. A very rough estimation of the probability that both photons pass through the same side is $\frac{1}{2}K^{-\frac{1}{2}} = 0.05$, where $K \approx 83$ is the Schmidt number of the entanglement for our source [10]. This limits the symmetry parameter to approximately $\mathcal{S} = 0.95 \times -1 + 0.05 \times 1 = -0.90$.

The element of the anti-symmetrizer is closely related to experimental techniques employed in Refs. [31, 153, 154]. These references use similar birefringent plates in which the polarization state of the entangled light is controlled in a position-dependent fashion. Combining entanglement of two degrees of freedom has already been addressed in all possible combinations: polarization/energy entanglement [155], polarization/transverse-position entanglement [31,74,76,153], and energy/transverse-position entanglement [64]. Combining the entanglement in all three degrees of freedom (polarization, transverse position, and energy) is called hyperentanglement [156, 157].

6.3.3 Experimental results

We have measured the coincidence count rate between two independently-scanning detectors for 2×2 configurations: bosonic and fermionic symmetry, with rotating and nonrotating diffusers for each symmetry. The four recorded two-photon coincidence patterns are displayed in Figs. 6.4(a)-(d). Each data point is recorded with an integration time of $12 - 14$ s, and each pattern takes typically 22 hours to be recorded. All displayed coincidence count rates have been corrected for accidental coincidences, which typically account for 10% of the rawly measured coincidence count rate.

Figures 6.4(a) and (c) display two-photon speckle patterns for bosonic symmetry and fermionic symmetry, respectively. Both patterns show high speckle contrasts, which indicates that the incident two-photon state is spatially pure [36]. Furthermore, both patterns are symmetric with respect to the $s_1 = s_2$ diagonal. This symmetry indicates that the incident two-photon state obeys exchange symmetry (bosonic, fermionic, or anyonic), and that the spatial scatter properties of the scattering system is the same for both photons (polarization independent scattering).

We are mainly interested in what happens on the diagonal $s_1 = s_2$, where both detectors are looking at the same spatial profile. On this diagonal, the relative two-photon speckle intensity is expected to depend on the type of symmetry that is applied. For bosonic symmetry, the two-photon speckle spots on the diagonal are expected to be twice as bright as compared to neighboring speckle spots ($\mathcal{F} = 2$). We indeed observe a couple of remarkably bright two-photon speckle spots on the diagonal of Fig. 6.4(a). For fermionic symmetry, we expect antipairing; not a single speckle spot is allowed to occur on the diagonal ($\mathcal{F} = 0$). We indeed observe complete two-photon darkness on the diagonal of Fig. 6.4(c).

The two-photon interference phenomenon survives averaging over different realizations of disorder. The two-photon speckle patterns are washed out in Figs. 6.4(b) and (d) due to the fast rotation of the diffusers. In the case of bosonic symmetry in figs. 6.4(b), the two-photon intensity on the diagonal clearly stands out. In the case of fermionic symmetry in Fig. 6.4(d), the two photons never occur at the same site.

To quantify the experimental degrees of pairing and antipairing, Fig. 6.5 displays 45°-projections of the ensemble-averaged two-photon patterns. The peak for bosonic symmetry and the dip for fermionic symmetry clearly stand out. The experimental pairing factors are extracted from Gaussian fits through the resulting curves. We obtain $\mathcal{F} = 1.89 \pm 0.05$ and $\mathcal{F} = 0.10 \pm 0.01$ for bosonic symmetry and fermionic symmetry, respectively. Our results clearly demonstrate pairing and antipairing of photons that have propagated through a random medium.

We do not fully understand the observed small deviation from perfect pairing ($\mathcal{F} = 2$) and perfect antipairing ($\mathcal{F} = 0$). Imperfect antipairing might be caused by the fact that a small portion of the photon pairs is transmitted through only one side of the anti-symmetrizer, which will give $\mathcal{S} > -1$ and $\mathcal{F} > 0$ (see Sec. 6.3.2 for details). In the pairing geometry, our experimental realization of a random scatterer (two rotating diffusers) might not correspond to the full ensemble of random matrices, which could cause $\mathcal{F} < 2$. We note that the pairing factor does not depend on the width of the detection modes because the phenomenon of (anti-)pairing is expected to appear in any mode basis. It is though very important that the detection modes of both detectors have practically equal shapes. Any difference between the mode profiles can have a degrading effect on the observed pairing factor. Although

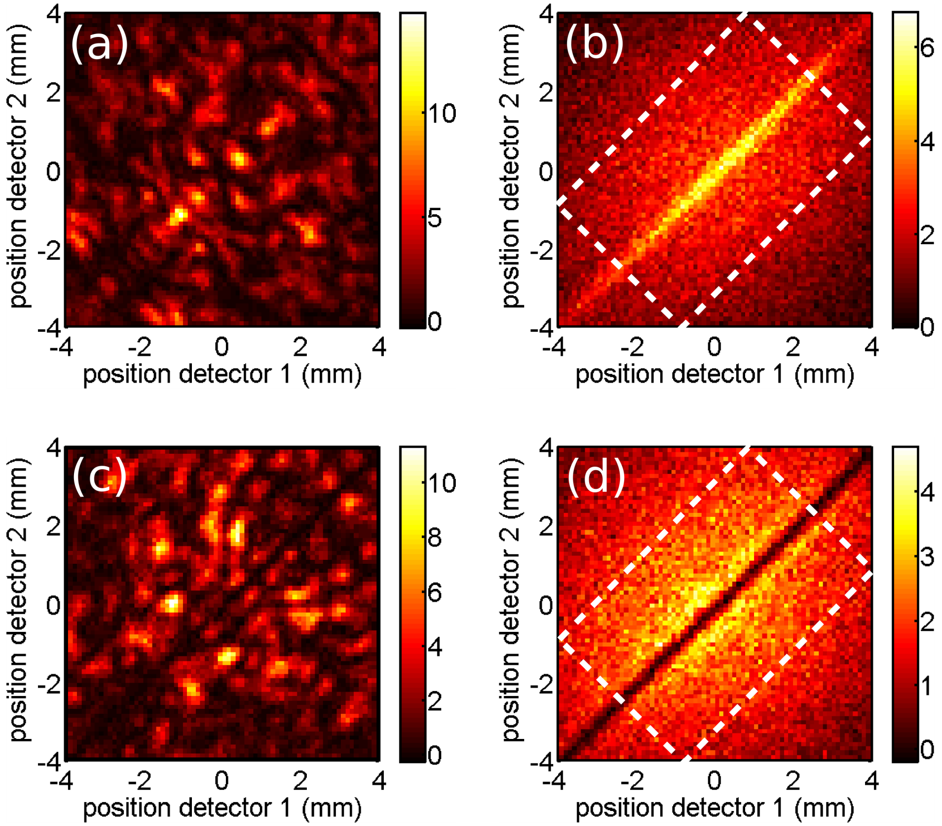

Figure 6.4: Four experimental two-photon patterns for four different configurations: (a) Static random medium and bosonic spatial symmetry. (b) Moving random medium and bosonic spatial symmetry. (c) Static random medium and fermionic spatial symmetry. (d) Moving random medium and fermionic spatial symmetry. The dotted rectangles in panels (b) and (d) indicate the selections that have been used for generating Fig. 6.5.

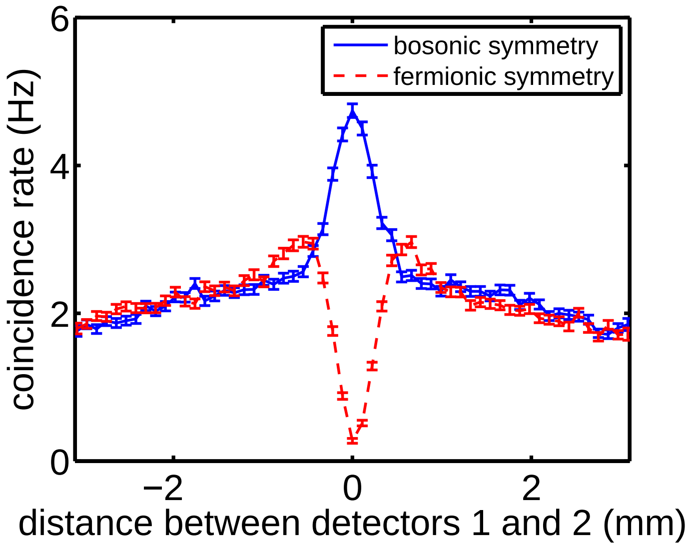

Figure 6.5: Experimental demonstration of pairing for bosonic spatial symmetry and antipairing for fermionic spatial symmetry. This effect has survived ensemble averaging since the random medium was moving fast during recording. These experimental data are extracted from Fig. 6.4 by performing projection operations along the 45° *diagonals within the dotted rectangles.*

we carefully equalized the sizes of our detection modes in the far-field plane, we observed up to 10% differences in divergence and astigmatism (probably caused by limited quality of the fiber tips). This might have had a degrading effect on the observed pairing factors.

We yet have little physical intuition for the physical processes that determine the precise shape of the (anti-)pairing curves in Fig. 6.5. For future reference we note that the FWHM of the peak in the coincidence count rate in Fig. 6.5 is (0.54 ± 0.03) mm. The fermionic dip is somewhat narrower at (0.40 ± 0.02) mm and exhibits small shoulders.

6.4 Concluding discussion

Our scattering experiments with labeled photons demonstrate, for the first time, a (tunable) two-photon interference effect that survives averaging over different realizations of disorder*. It is intriguing to see that some spatial structure survives scattering from rotating diffusers. We have presented a basic theoretical framework underlying the phenomenon. This framework is very effective in explaining the experimental results and is very useful for understanding which experimental parameters are essential. Spatial entanglement plays a central role because, within our theoretical framework, fermionic and anyonic symmetry can not be achieved without entanglement (see Tab. 6.1). The observed effect of (anti-)pairing is a two-photon interference phenomenon since it can be tuned via the phases of the complex two-photon probability amplitudes.

Our scheme provides an experimental toy model that nicely demonstrates the influence of particle exchange symmetries on two-particle propagation. The spatial symmetry between our polarization-labeled photons can be tuned such that it is mathematically equivalent to particle exchange symmetries between indistinguishable (i.e. unlabeled) quantum particles: bosons, fermions and anyons. Our experiments demonstrate how two particles with bosonic exchange symmetry have the tendency to pair up under random unitary scattering. In fermionic symmetry, the particles never come together. Of course, the two photons do not repel each other; it is just that propagation of two fermionic particles to the same site never happens.

Our experiments are closely related to the first observation of spatial antibunching of photons [31]. An observation of spatial antibunching proves nonclassicality of light, but, formally, it is not allowed to use a polarizing beam splitter for such an experiment [31]. We expect that our experimental results would have been qualitatively the same with a normal beam splitter (except for a factor 2 reduction in the coincidence count rate). So if we had used a normal beam splitter, Fig. 6.4(d) would likely have been another observation of spatial antibunching and a proof of nonclassicality of light.

6.5 Outlook

Future research on this two-photon interference phenomenon could address several aspects. First of all, it is desired to get a better understanding of how two-photon (anti-)pairing is related to the geometry of the scattering medium. Currently, we have no theoretical prediction for the shape and widths of the peak and dip in Fig. 6.5. We have little physical intuition for the physical processes that determine the precise shape of these curves.

* Two theoretical papers have recently appeared dealing with two-photon interference effects that survive averaging over different realizations of disorder [37, 38]. Reference [37] studies how Anderson localization in a 1D scatter configuration affects the structure in the ensemble averaged two-photon density for various incident two-photon states. Reference [38] predicts that a two-photon interference phenomenon should appear by itself for sufficiently long randomly scattering wave guides.

Future experiments could address anyonic symmetry to observe pairing factors $0 < \mathcal{F} < 2$. Another interesting option is to observe antipairing with energy-labeled photons. Such a system is particularly interesting because the photons would retain their labeling parameter also in 3D scattering random media. Photons from SPDC are energy-labeled since the total energy of the photon pair is fixed to the photon energy of the pump beam.

It would be very useful to study the phenomenon in scattering systems in which either the labeling of the photons is degraded by the scattering process, or the two photons encounter slightly different scattering matrices. The theoretical formalism must then be extended to a $2M \times 2M$ unitary scattering matrix; the upper-left $M \times M$ submatrix for the first photon, the lower-right submatrix for the second, and the two off-diagonal submatrices for the coupling between the subsystems of the photons.

Finally, it would be interesting to investigate in which way the phenomenon of two-photon (anti-)pairing is related to one-photon interference phenomena. Well-known one-photon interference phenomena that survive averaging over different realizations of disorder are enhanced backscattering and Anderson localization of light [39, 42, 45, 158]. Recent simulations in 1D scattering systems have already shown that profound correlations can exist between (one-photon) Anderson localization and ensemble-averaged two-photon propagation [37].

6.6 Acknowledgements

We thank G. Nienhuis for valuable discussions, and R. D. Gill and S. Zohren for pointing out references on the evaluation of invariant unitary integrals.

6.7 APPENDIX: Scattered density matrix

In this appendix we derive explicit expressions for the scattered two-photon density matrix in Eq. (6.9), recapitulated,

$$\rho^{(\mathrm{out})}_{qr,q'r'} = \sum_{klk'l'} A_{kl} A^*_{k'l'} \overline{u_{qk} u_{rl} u^*_{q'k'} u^*_{r'l'}}. \tag{6.13}$$

The random unitary matrix ensemble will be used for averaging over different realizations of disorder. Any unitary integral of the form

$$\overline{u_{a_1 b_1} ... u_{a_n b_n} u^*_{c_1 d_1} ... u^*_{c_n d_n}}$$

is nonzero if and only if $\mathbf{c} \in P(\mathbf{a})$ and $\mathbf{d} \in P(\mathbf{b})$, where $P(\mathbf{x})$ is the collection of all different permutations of $\mathbf{x}$, [147, 148]. Logically, there are four essentially different nonzero second-order integrals possible, being [147, 148]

$$\alpha_1 \equiv \overline{u_{11}u_{11}u_{11}^*u_{11}^*} = \frac{2M}{M^2(M+1)}, \tag{6.14}$$

$$\alpha_2 \equiv \overline{u_{11}u_{12}u_{11}^*u_{12}^*} = \frac{M}{M^2(M+1)}, \tag{6.15}$$

$$\alpha_3 \equiv \overline{u_{11}u_{22}u_{11}^*u_{22}^*} = \frac{M^2}{M^2(M+1)(M-1)}, \tag{6.16}$$

$$\alpha_4 \equiv \overline{u_{11}u_{22}u_{12}^*u_{21}^*} = \frac{-M}{M^2(M+1)(M-1)}, \tag{6.17}$$

where M is the dimension of the random unitary matrix. When applying this knowledge to Eq. (6.13) it is found that the density matrix elements can take four different values

$$\rho^{(\mathrm{out})}_{qr,q'r'} = \begin{cases} \sum\limits_{klk'l'} A_{kl}A^*_{k'l'}\overline{u_{qk}u_{ql}u^*_{qk'}u^*_{ql'}} & , q=q'=r=r' \\ \sum\limits_{klk'l'} A_{kl}A^*_{k'l'}\overline{u_{qk}u_{rl}u^*_{qk'}u^*_{rl'}} & , (q=q')\neq(r=r') \\ \sum\limits_{klk'l'} A_{kl}A^*_{k'l'}\overline{u_{qk}u_{rl}u^*_{rk'}u^*_{ql'}} & , (q=r')\neq(r=q') \\ 0 & , \text{elsewhere.} \end{cases} \tag{6.18}$$

Now it is a matter of bookkeeping to perform the summation and using the integrals in Eqs. (6.14)-(6.17). The nonzero contributions in the summations of Eq. (6.18) are listed in Tab. 6.2. By applying this list to Eq. (6.18) we obtain

$$\rho^{(\mathrm{out})}_{qr,q'r'} = \begin{cases} \alpha_1\mathcal{D}+\alpha_2(\mathcal{T}-\mathcal{D})+\alpha_2(\mathcal{S}-\mathcal{D}) & , q=q'=r=r' \\ \alpha_2\mathcal{D}+\alpha_3(\mathcal{T}-\mathcal{D})+\alpha_4(\mathcal{S}-\mathcal{D}) & , (q=q')\neq(r=r') \\ \alpha_2\mathcal{D}+\alpha_4(\mathcal{T}-\mathcal{D})+\alpha_3(\mathcal{S}-\mathcal{D}) & , (q=r')\neq(r=q') \\ 0 & , \text{elsewhere} \end{cases}, \tag{6.19}$$

where we introduced three functionals of the input A_{kl} being

$$\mathcal{T} \equiv \sum_{k=1}^{M}\sum_{l=1}^{M} A_{kl}A^*_{kl} \tag{6.20}$$

$$\mathcal{D} \equiv \sum_{k=1}^{M} A_{kk}A^*_{kk}, \tag{6.21}$$

$$\mathcal{S} \equiv \sum_{k=1}^{M}\sum_{l=1}^{M} A_{kl}A^*_{lk}. \tag{6.22}$$

	$\overline{u_{qk}u_{ql}u^*_{qk'}u^*_{ql'}}$	$\overline{u_{qk}u_{rl}u^*_{qk'}u^*_{rl'}}$	$\overline{u_{qk}u_{rl}u^*_{rk'}u^*_{ql'}}$
$k = l = k' = l'$	α_1	α_2	α_2
$(k = k') \neq (l = l')$	α_2	α_3	α_4
$(k = l') \neq (l = k')$	α_2	α_4	α_3

Table 6.2: Listing of nonzero outcomes for the three unitary integrals in Eq. (6.18) for different combinations of the summation indices k, l, k', and l' (note that $q \neq r$). The coefficients α_i are defined in Eqs. (6.14)-(6.17).

The symbols $\mathcal{T}$, $\mathcal{D} \in [0, \mathcal{T}]$, and $\mathcal{S} \in [-(\mathcal{T} - \mathcal{D}), +(\mathcal{T} - \mathcal{D})]$ stand for *total power*, *diagonal power*, and *symmetry parameter*, respectively.

By substituting Eqs. (6.14)-(6.17) for the unitary integrals α_i in Eq. (6.19) we find

$$\rho^{(\text{out})}_{qr,q'r'} = \begin{cases} \dfrac{1}{M}\left(\dfrac{\mathcal{T}+\mathcal{S}}{M+1}\right) & , q = q' = r = r' \\ \dfrac{1}{M(M-1)}\left(\dfrac{M\mathcal{T}-\mathcal{S}}{M+1}\right) & , (q = q') \neq (r = r') \\ \dfrac{1}{M(M-1)}\left(\dfrac{M\mathcal{S}-\mathcal{T}}{M+1}\right) & , (q = r') \neq (r = q') \\ 0 & , \text{elsewhere} \end{cases} \tag{6.23}$$

We now make two remarks of mathematical interest. The first remark is that $\mathcal{T}$ and $\mathcal{S}$ are functionals of A_{kl} that are conserved under transformation via any unitary scattering matrix. This can easily be demonstrated by combining the appropriate elements of $\rho^{(\text{out})}_{qr,qr}$ to obtain the average $\mathcal{T}$ and $\mathcal{S}$ in the output state being

$$\overline{\mathcal{T}^{(\text{out})}} = \sum_{qr} \rho^{(\text{out})}_{qr,qr} = M\rho^{(\text{out})}_{11,11} + M(M-1)\rho^{(\text{out})}_{12,12} = \mathcal{T}, \tag{6.24}$$

$$\overline{\mathcal{S}^{(\text{out})}} = \sum_{qr} \rho^{(\text{out})}_{qr,rq} = M\rho^{(\text{out})}_{11,11} + M(M-1)\rho^{(\text{out})}_{12,21} = \mathcal{S}. \tag{6.25}$$

The second remark is that the unitary integrals in Eqs. (6.14)-(6.17) are uniquely determined by stating that $\mathcal{T}$ is a conserved quantity for any M and any A_{kl}. In other words, by combining Eqs. (6.24) and (6.19) one retrieves Eqs. (6.14)-(6.17). Actually, the unitary integrals are also uniquely determined by stating that $\mathcal{S}$ is a conserved quantity for any M and any A_{kl}. So by combining Eqs. (6.25) and (6.19) one retrieves Eqs. (6.14)-(6.17) as well.

Finally, we restrict ourselves to $\mathcal{T} = 1$, which corresponds to normalized two-photon quantum states in Eq. (6.1). Furthermore, we concentrate on the on-diagonal elements of the scattered density matrix only. The relative strength of these elements is given by the ratio

$$\mathcal{F} \equiv \frac{\rho^{(\text{out})}_{11,11}}{\rho^{(\text{out})}_{12,12}} = \frac{1+\mathcal{S}}{1+\dfrac{1-\mathcal{S}}{M-1}}, \tag{6.26}$$

which we will call the *pairing factor*, where $\mathcal{S} \in [-1, 1]$ and $\mathcal{F} \in [0, 2]$. The pairing factor is the two-photon detection probability observed with two detectors looking into the same spatial channel divided by the two-photon detection probability observed with two detectors looking into different spatial channels. Explicit values for these probabilities are easily retrieved by using

$$\text{Tr}\rho^{(\text{out})}_{qr,q'r'} = M\rho^{(\text{out})}_{11,11} + M(M-1)\rho^{(\text{out})}_{12,12} = 1, \tag{6.27}$$

which is associated with energy-conserving scattering processes.

Bibliography

[1] J. C. Maxwell, *A dynamical theory of the electromagnetic field*, Phil. Trans. Roy. Soc. Lond. **155**, 459 (1865).

[2] J. D. Jackson, *Classical electrodynamics*, 3 ed. (John Wiley & Sons, Hoboken, NJ, 1999).

[3] L. Mandel and E. Wolf, *Optical Coherence and Quantum Optics* (Cambridge University Press, The Pitt Building, Trumpington Street, Cambridge, 1995).

[4] R. Loudon, *The quantum theory of light*, 3 ed. (Oxford University Press, Great Clarendon Street, Oxford, 2000).

[5] R. J. Glauber, *The quantum theory of optical coherence*, Phys. Rev. **130**, 2529 (1963).

[6] D. C. Burnham and D. L. Weinberg, *Observation of Simultaneity in Parametric Production of Optical Photon Pairs*, Phys. Rev. Lett. **25**, 84 (1970).

[7] R. Ghosh and L. Mandel, *Observation of Nonclassical Effects of in the Interference of Two Photons*, Phys. Rev. Lett. **59**, 1903 (1987).

[8] C. K. Hong, Z. Y. Ou, and L. Mandel, *Measurement of subpicosecond time intervals between two photons by interference*, Phys. Rev. Lett. **59**, 2044 (1987).

[9] C. K. Law and J. H. Eberly, *Analysis and Interpretation of High Transverse Entanglement in Optical Parametric Down Conversion*, Phys. Rev. Lett. **92**, 127903 (2004).

[10] H. Di Lorenzo Pires, C. H. Monken, and M. P. van Exter, *Direct measurement of transverse-mode entanglement in two-photon states*, Phys. Rev. A **80**, 022307 (2009).

[11] H. Bechmann-Pasquinucci and W. Tittel, *Quantum cryptography using larger alphabets*, Phys. Rev. A **61**, 062308 (2000).

[12] D. Kaszlikowski, P. Gnaciński, M. Żukowski, W. Miklaszewski, and A. Zeilinger, *Violations of Local Realism by Two Entangled N-Dimensional Systems Are Stronger than for Two Qubits*, Phys. Rev. Lett. **85**, 4418 (2000).

[13] D. Collins, N. Gisin, N. Linden, S. Massar, and S. Popescu, *Bell Inequalities for Arbitrarily High-Dimensional Systems*, Phys. Rev. Lett. **88**, 040404 (2002).

[14] L. Zhang, C. Silberhorn, and I. A. Walmsley, *Secure Quantum Key Distribution using Continuous Variables of Single Photons*, Phys. Rev. Lett. **100**, 110504 (2008).

[15] L. Allen, M. W. Beijersbergen, R. J. C. Spreeuw, and J. P. Woerdman, *Orbital angular momentum of light and the transformation of Laguerre-Gaussian laser modes*, Phys. Rev. A **45**, 8185 (1992).

[16] A. Mair, A. Vaziri, G. Weihs, and A. Zeilinger, *Entanglement of the orbital angular momentum states of photons*, Nature **412**, 313 (2001).

[17] G. Molina-Terriza, J. P. Torres, and L.Torner, *Orbital angular momentum of photons in noncollinear parametric downconversion*, Opt. Comm. **228**, 155 (2003).

[18] S. S. R. Oemrawsingh, X. Ma, D. Voigt, A. Aiello, E. R. Eliel, G. W. 't Hooft, and J. P. Woerdman, *Experimental Demonstration of Fractional Orbital Angular Momentum Entanglement of Two Photons*, Phys. Rev. Lett. **95**, 240501 (2005).

[19] G. Molina-Terriza, J. P. Torres, and L.Torner, *Twisted Photons*, Nature Phys. **3**, 305 (2007).

[20] M. V. Vasnetsov, J. P. Torres, D. V. Petrov, and L. Torner, *Observation of the orbital angular momentum spectrum of a light beam*, Opt. Lett. **28**, 2285 (2003).

[21] R. Zambrini and S. M. Barnett, *Quasi-Intrinsic Angular Momentum and the Measurement of Its Spectrum*, Phys. Rev. Lett. **96**, 113901 (2006).

[22] M. P. van Exter, P. S. K. Lee, S. Doesburg, and J. P. Woerdman, *Mode Counting in High Dimensional Orbital Angular Momentum Entanglement*, Opt. Express **15**, 6431 (2007).

[23] P. H. Souto Ribeiro, C. H. Monken, and G. A. Barbosa, *Measurement of coherence area in parametric downconversion luminescence*, Appl. Opt. **33**, 352 (1994).

[24] C. K. Hong and T. G. Noh, *Two-photon double-slit interference experiment*, J. Opt. Soc. Am. B **15**, 1192 (1998).

[25] T. G. Noh and C. K. Hong, *Manifestation of complementarity in double-slit interference*, J. Korean Phys. Soc. **33**, 383 (1998).

[26] E. J. S. Fonseca, C. H. Monken, and S. Pádua, *Measurement of the de Broglie wavelength of a multiphoton wavepacket*, Phys. Rev. Lett. **82**, 2868 (1999).

[27] E. J. S. Fonseca, C. H. Monken, S. Pádua, and G. A. Barbosa, *Transverse coherence length of down-converted light in the two-photon state*, Phys. Rev. A **59**, 1608 (1999).

[28] E. J. S. Fonseca, J. C. Machado da Silva, C. H. Monken, and S. Pádua, *Controlling two-particle conditional interference*, Phys. Rev. A **61**, 023801 (2000).

[29] A. F. Abouraddy, M. B. Nasr, B. E. A. Saleh, A. V. Sergienko, and M. C. Teich, *Demonstration of the complementarity of one- and two-photon interference*, Phys. Rev. A **63**, 063803 (2001).

[30] M. D'Angelo, M. V. Chekhova, and Y. Shih, *Two-photon diffraction and quantum lithography*, Phys. Rev. Lett. **87**, 013602 (2001).

[31] W. A. T. Nogueira, S. P. Walborn, S. Pádua, and C. H. Monken, *Experimental Observation of Spatial Antibunching of Photons*, Phys. Rev. Lett. **86**, 4009 (2001).

[32] G. Lima, F. A. Torres-Ruiz, L. Neves, A. Delgado, C. Saavedra, and S. Pádua, *State determination for composite systems of two spatial qubits*, J. Phys.: Conference Series **84**, 012012 (2007).

[33] L. Neves, G. Lima, E. J. S. Fonseca, L. Davidovich, and S. Pádua, *Characterizing entanglement in qubits created with spatially correlated twin photons*, Phys. Rev. A **76**, 032314 (2007).

[34] R. Shimizu, T. Yamaguchi, Y. Mitsumori, H. Kosaka, and K. Edamatsu, *Generation of polarization entanglement from spatially correlated photons in spontaneous parametric down-conversion*, Phys. Rev. A **77**, 032338 (2008).

[35] G. Taguchi, T. Dougakiuchi, N. Yoshimoto, K. Kasai, M. Iinuma, H. F. Hofmann, and Y. Kadoya, *Measurement and control of spatial qubits generated by passing photons through double slits*, Phys. Rev. A **78**, 012307 (2008).

[36] C. W. J. Beenakker, J. W. F. Venderbos, and M. P. van Exter, *Two-Photon Speckle as a Probe of Multi-Dimensional Entanglement*, Phys. Rev. Lett. **102**, 193601 (2009).

[37] Y. Lahini, Y. Bromberg, D. N. Christodoulides, and Y. Silberberg, *Quantum Correlations in Two-Particle Anderson Localization*, Phys. Rev. Lett. **105**, 163905 (2010).

[38] J. R. Ott, N. A. Mortensen, and P. Lodahl, *Quantum Interference and Entanglement Induced by Multiple Scattering of Light*, Phys. Rev. Lett. **105**, 090501 (2010).

[39] M. C. W. van Rossum and T. M. Nieuwenhuizen, *Multiple scattering of classical waves: microscopy, mesoscopy, and diffusion*, Rev. Mod. Phys. **71**, 313 (1999).

[40] E. Akkermans and G. Montambaux, *Mesoscopic physics of electrons and photons* (Cambridge University Press, The Edinburgh Building, Cambridge CB2 8RU, UK, 2007).

[41] J. W. Goodman, *Speckle Phenomena in Optics: Theory and Applications* (Roberts and Company Publishers, Greenwood Village, CO, 2007).

[42] M. P. van Albada and A. Lagendijk, *Observation of Weak Localization of Light in a Random Medium*, Phys. Rev. Lett. **55**, 2692 (1985).

[43] C. M. Aegerter and G. Maret, *Coherent Backscattering and Anderson Localization of Light*, Progr. in Opt. **52**, 1 (2009).

[44] F. Scheffold and G. Maret, *Universal Conductance Fluctuations of Light*, Phys. Rev. Lett. **81**, 5800 (1998).

[45] P. W. Anderson, *Absence of diffusion in certain random lattices*, Phys. Rev. **109**, 1492 (1958).

[46] M. Störzer, P. Gross, C. M. Aegerter, and G. Maret, *Observation of the Critical Regime Near Anderson Localization of Light*, Phys. Rev. Lett. **96**, 063904 (2006).

[47] A. Lagendijk, B. van Tiggelen, and D. S. Wiersema, *Fifty years of Anderson localization*, Physics Today **62**, 24 (2009).

[48] A. V. Belinskii and D. N. Klyshko, *Two-photon optics: diffraction, holography, and transformation of two-dimensional signals*, Sov. Phys. JETP **78**, 259 (1994).

[49] J. H. Shapiro and K. X. Sun, *Semiclassical versus quantum behavior in fourth-order interference*, J. Opt. Soc. B **11**, 1130 (1994).

[50] B. I. Erkmen and J. H. Shapiro, *Unified theory of ghost imaging with Gaussian-state light*, Phys. Rev. A **77**, 043809 (2008).

[51] C. K. Hong and L. Mandel, *Theory of parametric frequency down-conversion of light*, Phys. Rev. A **31**, 2409 (1985).

[52] D. N. Klyshko, *Effect of focusing on photon correlation in parametric light scattering*, Sov. Phys. JETP **67**, 1131 (1988).

[53] Z. Y. Ou, L. J. Wang, and L. Mandel, *Vacuum effects on interference in two-photon down conversion*, Phys. Rev. A **40**, 1428 (1989).

[54] M. H. Rubin, D. N. Klyshko, Y. H. Shih, and A. V. Sergienko, *Theory of two-photon entanglement in type-II optical parametric down-conversion*, Phys. Rev. A **50**, 5122 (1994).

[55] A. V. Belinskii and D. N. Klyshko, *Two-Photon Wave Packets*, Laser Phys. **4**, 663 (1994).

[56] M. H. Rubin, *Transverse correlation in optical spontaneous parametric down-conversion*, Phys. Rev. A **54**, 5349 (1996).

[57] V. Giovannetti, L. Maccone, J. H. Shapiro, and F. N. C. Wong, *Generating Entangled Two-Photon States with Coincident Frequencies*, Phys. Rev. Lett. **88**, 183602 (2002).

[58] J. H. Shapiro, *Quantum Gaussian Noise*, Proc. SPIE **5111**, 382 (2003).

[59] Y. Shih, *Entangled biphoton source - property and preparation*, Rep. Prog. Phys. **66**, 1009 (2003).

[60] A. Gatti, R. Zambrini, M. San Miguel, and L. A. Lugiato, *Multiphoton multimode polarization entanglement in parametric down-conversion*, Phys. Rev. A **68**, 053807 (2003).

[61] D. Z. Cao, Z. Li, Y. H. Zhai, and K. Wang, *One-photon and two-photon double-slit interference in spontaneous and stimulated parametric down conversion*, Eur. Phys. J. D **33**, 137 (2005).

[62] F. N. C. Wong, J. H. Shapiro, and T. Kim, *Efficient Generation of Polarization-Entangled Photons in a Nonlinear Crystal*, Laser Phys. **16**, 1517 (2006).

[63] Z. Y. Jeff Ou, *Multi-Photon Quantum Interference* (Springer, 233 Springer Street, New York, 2007).

[64] A. Gatti, E. Brambilla, L. Caspani, O. Jedrkiewicz, and L. A. Lugiato, *X Entanglement: The Nonfactorable Spatiotemporal Structure of Biphoton Correlation*, Phys. Rev. Lett. **102**, 223601 (2009).

[65] S. P. Walborn, C. H. Monken, S. Pádua, and P. H. Souto Ribeiro, *Spatial correlations in parametric down-conversion*, Phys. Rep. [Article in press doi:10.1016/j.physrep.2010.06.003] (2010).

[66] B. I. Erkmen and J. H. Shapiro, *Gaussian state theory of two-photon imaging*, Phys. Rev. A **78**, 023835 (2008).

[67] E. Brambilla, A. Gatti, M. Bache, and L. A. Lugiato, *Simultaneous near-field and far-field spatial quantum correlations in the high-gain regime of parametric down-conversion*, Phys. Rev. A **69**, 023802 (2004).

[68] T. B. Pittman, D. V. Strekalov, D. N. Klyshko, M. H. Rubin, A. V. Sergienko, and Y. H. Shih, *Two-photon geometric optics*, Phys. Rev. A **53**, 2804 (1996).

[69] C. H. Monken, P. H. S. Ribeiro, and S. Pádua, *Transfer of angular spectrum and image formation in spontaneous parametric down-conversion*, Phys. Rev. A **57**, 3123 (1998).

[70] A. E. Siegman, *Lasers* (University Science Books, Sausalito, 1986).

[71] D. N. Klyshko, *Combined EPR and two-slit experiments: interference of advanced waves*, Phys. Lett. A **132**, 299 (1988).

[72] P. G. Kwiat, K. Mattle, H. Weinfurter, A. Zeilinger, A. V. Sergienko, and Y. Shih, *New High-intensity source of polarization entangled photon pairs*, Phys. Rev. Lett. **75**, 4337 (1995).

[73] N. Gisin, G. Ribordy, W. Tittel, and H. Zbinden, *Quantum cryptography*, Rev. Mod. Phys. **74**, 145 (2002).

[74] S. P. Walborn, A. N. de Oliveira, S. Pádua, and C. H. Monken, *Multimode Hong-Ou-Mandel Interference*, Phys. Rev. Lett. **90**, 143601 (2003).

[75] D. P. Caetano and P. H. Souto Ribeiro, *Generation of spatial antibunching with free-propagating twin beams*, Phys. Rev. A **68**, 043806 (2003).

[76] W. A. T. Nogueira, S. P. Walborn, S. Pádua, and C. H. Monken, *Generation of a Two-Photon Singlet Beam*, Phys. Rev. Lett. **92**, 043602 (2004).

[77] N. K. Langford, R. B. Dalton, M. D. Harvey, J. L. O'Brien, G. J. Pryde, A. Gilchrist, S. D. Bartlett, and A. G. White, , Phys. Rev. Lett. **93**, 053601 (2004).

[78] B. E. A. Saleh, A. F. Abouraddy, A. V. Sergienko, and M. C. Teich, *Duality between partial coherence and partial entanglement*, Phys. Rev. A **62**, 043816 (2000).

[79] P. S. K. Lee and M. P. van Exter, *Spatial labeling in a two-photon interferometer*, Phys. Rev. A **73**, 063827 (2006).

[80] M. P. van Exter, A. Aiello, S. S. R. Oemrawsingh, G. Nienhuis, and J. P. Woerdman, *Effect of spatial filtering on Schmidt decomposition of entangled photons*, Phys. Rev. A **74**, 012309 (2006).

[81] J. P. Torres, A. Alexandrescu, and L. Torner, *Quantum spiral bandwidth of entangled two-photon states*, Phys. Rev. A **68**, 050301 (2003).

[82] R. Grobe, K. Rzazewski, and J. H. Eberly, *Measure of electron-electron correlation in atomic physics*, J. Phys. B **27**, L503 (1994).

[83] A. Ekert and P. L. Knight, *Entangled quantum-systems and the Schmidt decomposition*, Am. J. Phys. **63**, 415 (1995).

[84] S. Franke-Arnold, S. M. Barnett, M. J. Padgett, and L. Allen, *Two-photon entanglement of orbital angular momentum states*, Phys. Rev. A **65**, 033823 (2002).

[85] L. Torner, J. P. Torres, and S. Carrasco, *Digital spiral imaging*, Opt. Express **13**, 873 (2005).

[86] M. Segev, R. Solomon, and A. Yariv, *Manifestation of Berry's phase in image-bearing optical beams*, Phys. Rev. Lett. **69**, 590 (1992).

[87] M. W. Beijersbergen, R. P. C. Coerwinkel, M. Kristensen, and J. P. Woerdman, *Helical-wavefront laser beams produced with a spiral phaseplate*, Opt. Comm. **112**, 321 (1994).

[88] S. S. R. Oemrawsingh, J. A. W. van Houwelingen, E. R. Eliel, J. P. Woerdman, E. J. K. Verstegen, J. G. Kloosterboer, and G. W. 't Hooft, *Production and characterization of spiral phase plates for optical wavelengths*, Appl. Opt. **43**, 688 (2004).

[89] M. M. Fejer, G. A. Magel, D. H. Jundt, and R. L. Byer, *Quasi-phase-matched second harmonic generation: tuning and tolerances*, IEEE J. Quantum Electron. **28**, 2631 (1992).

[90] M. Houé and P. D. Townsend, *An introduction to methods of periodic poling for second-harmonic generation*, J. Phys. D: Appl. Phys. **28**, 1747 (1995).

[91] C. Canalias, V. Pasiskevicius, and F. Laurell, *Periodic Poling of $KTiOPO_4$: From Micrometer to Sub-Micrometer Domain Gratings*, Ferroelectrics **340**, 27 (2006).

[92] F. Laurell, M. G. Roelofs, W. Bindloss, H. Hsiung, A. Suna, and J. D. Bierlein, *Detection of ferroelectric domain reversal in $KTiOPO_4$ waveguides*, J. Appl. Phys. **71**, 15 (1992).

[93] H. Bluhm, A. Wadas, R. Wiesendanger, A. Roshko, J. A. Aust, and D. Nam, *Imaging of domain-inverted gratings in $LiNbO_3$ by electrostatic force microscopy.*, Appl. Phys. Lett. **71**, 146 (1997).

[94] G. Rosenman, A. Skliar, I. Lareah, N. Angert, M. Tseitlin, and M. Roth, *Observation of ferroelectric domain structures by secondary-electron microscopy in as-grown $KTiOPO_4$*, Phys. Rev. B **54**, 6222 (1996).

[95] C. Canalias, V. Pasiskevicius, A. Fragemann, and F. Laurell, *High-resolution domain imaging on the nonpolar y-face of periodically poled $KTiOPO_4$ by means of atomic force microscopy.*, Appl. Phys. Lett. **83**, 734 (2003).

[96] S. K. Johansen and P. Baldi, *Characterization of quasi-phase-matching gratings in quadratic media through double-pass second-harmonic power measurements*, J. Opt. Soc. Am. B **21**, 1137 (2004).

[97] I. Cristiani, C. Liberale, V. Degiorgio, G. Tartarini, and P. Bassi, *Nonlinear characterization and modeling of periodically poled lithium niobate waveguides for 1.5-μm-band cascaded wavelength conversion*, Opt. Commun. **187**, 263 (2001).

[98] S. J. Holmgren, V. Pasiskevicius, S. Wang, and F. Laurell, *Three-dimensional characterization of the effective second-order nonlinearity in periodically poled crystals*, Opt. Lett. **28**, 1555 (2003).

[99] G. K. H. Kitaeva, V. V. Tishkova, I. I. Naumova, A. N. Penin, C. H. Kang, and S. H. Tang, *Mapping of periodically poled crystals via spontaneous parametric down conversion*, Appl. Phys. B **81**, 645 (2005).

[100] P. D. Maker, R. W. Terhune, M. Nisenoff, and C. M. Savage, *Effects of dispersion and focussing on the production of optical harmonics*, Phys. Rev. Lett. **8**, 21 (1962).

[101] S. Emanueli and A. Arie, *Temperature-dependent dispersion equations for $KTiOPO_4$ and $KTiOAsO_4$*, Appl. Opt. **42**, 6661 (2003).

[102] F. Pignatiello, M. D. Rosa, P. Ferraro, S. Grilli, P. D. Natale, A. Arie, and S. D. Nicola, *Measurement of the thermal expansion coefficients of ferroelectric crystals by a moiré interferometer*, Opt. Commun. **227**, 14 (2007).

[103] T. Y. Fan, C. E. Huang, B. Q. Hu, R. C. Eckardt, Y. X. Fan, R. L. Byer, and R. S. Feigelson, *Second harmonic generation and accurate index of refraction measurements in flux-grown $KTiOPO_4$*, Appl. Opt. **26**, 2390 (1987).

[104] V. A. Dyakov, V. V. Krasnikov, V. I. Pryalkin, M. S. Pshenichnikov, T. B. Razumikhina, V. S. Solomatin, and A. I. Kholodnykh, *Sellmeier equation and tuning characteristics of PPKTP crystal frequency converters in the 0.4-4.0 μm range*, Sov. J. Quant. Electron. **18**, 1059 (1988).

[105] D. W. Anthon and C. D. Crowder, *Wavelength dependent phase matching in KTP*, Appl. Opt. **27**, 2650 (1988).

[106] K. Fradkin, A. Arie, A. Skliar, and G. Rosenman, *Tunable midinfrared source by difference frequency generation in bulk periodically poled $KTiOPO_4$*, Appl. Phys. Lett. **74**, 914 (1999).

[107] K. Kato and E. Takaoka, *Sellmeier and thermo-optic dispersion formulas for KTP*, Appl. Opt. **41**, 5040 (2002).

[108] W. Wiechmann and S. Kubota, *Refractive-index temperature derivatives of potassium titanyl phosphate*, Opt. Lett. **18**, 1208 (1993).

[109] G. Rosenman, A. Skliar, D. Enger, M. Oron, and M. Katz, *Low temperature periodic electrical poling of flux-grown $KTiOPO_4$ and isomorphic crystals*, Appl. Phys. Lett. **73**, 3650 (1998).

[110] R. C. Eckardt, H. Masuda, Y. X. Fan, and R. L. Byer, *Absolute and relative nonlinear optical coefficients of KDP, KD-STAR-P, BaB_2O_3, $LiIO_3$,*

MgO-LiNbO$_3$, and KTP measured by phase-matched 2nd harmonic generation, IEEE J. Quantum Electron. **26**, 922 (1990).

[111] M. V. Pack, D. J. Armstrong, and A. V. Smith, *Measurement of the $\chi^{(2)}$ tensors of KTiOPO$_4$, KTiOAsO$_4$, RbTiOPO$_4$, and RbTiOAsO$_4$ crystals*, Appl. Opt. **43**, 3319 (2004).

[112] M. Yamada, N. Nada, M. Saitoh, and K. Watanabe, *First-order quasi-phase matched LiNbO$_3$ waveguide periodically poled by applying an external field for efficient blue second-harmonic generation*, Appl. Phys. Lett. **62**, 435 (1993).

[113] G. Rosenman, K. Garb, A. Skliar, M. Oron, D. Eger, and M. Katz, *Domain broadening in quasi-phase-matched nonlinear optical devices*, Appl. Phys. Lett. **73**, 865 (1998).

[114] D. V. Strekalov, A. V. Sergienko, D. N. Klyshko, and Y. H. Shih, *Observation of Two-Photon 'Ghost' Interference and Diffraction*, Phys. Rev. Lett. **74**, 3600 (1995).

[115] A. Gatti, E. Brambilla, and L. A. Lugiato, *Entangled Imaging and Wave-Particle Duality; From the Microscopic to the Macroscopic Realm*, Phys. Rev. Lett. **90**, 133603 (2003).

[116] A. N. Boto, P. Kok, D. S. Abrams, S. L. Braunstein, C. P. Williams, and J. P. Dowling, *Quantum interferometric optical lithography: exploiting entanglement to beat the diffraction limit*, Phys. Rev. Lett. **85**, 2733 (2000).

[117] W. H. Peeters, E. J. K. Verstegen, and M. P. van Exter, *Orbital angular momentum analysis of high-dimensional entanglement*, Phys. Rev. A **76**, 042302 (2007).

[118] M. D'Angelo, Y.-H. Kim, S. P. Kulik, and Y. Shih, *Identifying entanglement using quantum ghost interference and imaging*, Phys. Rev. Lett. **92**, 233601 (2004).

[119] R. S. Bennink, S. J. Bentley, R. W. Boyd, and J. C. Howell, *Quantum and classical coincidence imaging*, Phys. Rev. Lett. **92**, 033601 (2004).

[120] A. F. Abouraddy, T. Yarnall, B. E. A. Saleh, and M. C. Teich, *Violation of Bell's inequality with continuous spatial variables*, Phys. Rev. A **75**, 052114 (2007).

[121] T. Yarnall, A. F. Abouraddy, B. E. A. Saleh, and M. C. Teich, *Experimental Violation of Bell's Inequality in Spatial-Parity Space*, Phys. Rev. Lett. **99**, 170408 (2007).

[122] L. Neves, S. Pádua, and C. Saavedra, *Controlled generation of maximally entangled qudits using twin photons*, Phys. Rev. A **69**, 042305 (2004).

[123] L. Neves, G. Lima, J. G. Aguirre Gómez, C. H. Monken, C. Saavedra, and S. Pádua, *Generation of entangled states of qudits using twin photons*, Phys. Rev. Lett. **94**, 100501 (2005).

[124] G. Lima, L. Neves, I. F. Santos, J. G. Aguirre Gómez, C. Saavedra, and S. Pádua, *Propagation of spatially entangled qudits through free space*, Phys. Rev. A **73**, 032340 (2006).

[125] R. Shimizu, K. Edamatsu, and T. Itoh, *Quantum diffraction and interference of spatially correlated photon pairs and its Fourier-optical analysis*, Phys. Rev. A **74**, 013801 (2006).

[126] K. W. Chan, J. P. Torres, and J. H. Eberly, *Transverse entanglement migration in Hilbert space*, Phys. Rev. A **75**, 050101(R) (2007).

[127] S. Hill and W. K. Wootters, *Entanglement of a pair of quantum bits*, Phys. Rev. Lett. **78**, 5022 (1997).

[128] A. F. Abouraddy, B. E. A. Saleh, A. V. Sergienko, and M. C. Teich, *Degree of entanglement for two qubits*, Phys. Rev. A **64**, 050101(R) (2001).

[129] A. E. Siegman, *Lasers*, 1 ed. (University Science Books, 20 Edgehill Road, Mill Valley, California 94941, 1986), chapter 20, equation (14).

[130] J. C. Howell, R. S. Bennink, S. J. Bentley, and R. W. Boyd, *Realization of the Einstein-Podolsky-Rosen Paradox Using Momentum- and Position-Entangled Photons from Spontaneous Parametric Down Conversion*, Phys. Rev. Lett. **92**, 210403 (2004).

[131] G. Jaeger, M. A. Horne, and A. Shimony, *Complementarity of one-particle and two-particle interference*, Phys. Rev. A **48**, 1023 (1993).

[132] G. Jaeger, A. Shimony, and L. Vaidman, *Two interferometric complementarities*, Phys. Rev. A **51**, 54 (1995).

[133] D. F. Walls, *A simple field theoretic description of photon interference*, Am. J. Phys. **45**, 952 (1977).

[134] W. H. Peeters and M. P. van Exter, *Optical characterization of periodically poled $KTiOPO_4$*, Opt. Express **16**, 7344 (2008).

[135] P. Lodahl, A. P. Mosk, and A. Lagendijk, *Spatial Quantum Correlations in Multiple Scattered Light*, Phys. Rev. Lett. **95**, 173901 (2005).

[136] S. E. Skipetrov, *Quantum theory of dynamic multiple light scattering in fluctuating disordered media*, Phys. Rev. A **75**, 053808 (2007).

[137] S. Smolka, A. Huck, U. L. Andersen, A. Lagendijk, and P. Lodahl, *Observation of Spatial Quantum Correlations Induced by Multiple Scattering of Nonclassical Light*, Phys. Rev. Lett. **102**, 193901 (2009).

[138] A. Gatti, E. Brambilla, M. Bache, and L. A. Lugiato, *Ghost Imaging With Thermal Light: Comparing Entanglement and Classical Correlation*, Phys. Rev. Lett. **93**, 093602 (2004).

[139] B. E. A. Saleh, M. C. Teich, and A. V. Sergienko, *Wolf equations for two-photon light*, Phys. Rev. Lett. **94**, 223601 (2005).

[140] G. Scarcelli, V. Berardi, and Y. Shih, *Phase-conjugate mirror via two-photon thermal light imaging*, Appl. Phys. Lett. **88**, 061106 (2006).

[141] A. K. Jha and R. W. Boyd, *Spatial two-photon coherence of the entangled field produced by down-conversion using a partially spatially coherent pump beam*, Phys. Rev. A **81**, 013828 (2010).

[142] W. H. Peeters, J. J. Renema, and M. P. van Exter, *Engineering of two-photon spatial quantum correlations behind a double slit*, Phys. Rev. A **79**, 043817 (2009).

[143] H. Di Lorenzo Pires and M. P. van Exter, *Near-field correlations in the two-photon field*, Phys. Rev. A **80**, 053820 (2009).

[144] A. Valencia, G. Scarcelli, M. D'Angelo, and Y. Shih, *Two-photon imaging with thermal light*, Phys. Rev. Lett. **94**, 063601 (2005).

[145] W. H. Carter and E. Wolf, *Coherence and radiometry with quasihomogeneous planar sources*, J. Opt. Soc. Am. **67**, 785 (1977).

[146] C. W. J. Beenakker, *Applications of random matrix theory to condensed matter and optical physics*, arXiv:0904.1432v2 .

[147] S. Samuel, *U(N) Integrals, 1/N, and De Wit-'t Hooft anomalies*, J. Math. Phys. **21**, 2695 (1980).

[148] S. Aubert and C. Lam, *Invariant integration over the unitary group*, J. Math. Phys. **44**, 6112 (2003).

[149] F. Wilczek, *Quantum Mechanics of Fractional-Spin Particles*, Phys. Rev. Lett. **49**, 957 (1982).

[150] D. J. Griffiths, *Introduction to quantum mechanics* (Prentics Hall, Upper Saddle River, New Jersey 07458, 1995).

[151] H. Di Lorenzo Pires and M. P. van Exter, *Observation of near-field correlations in spontaneous parametric down-conversion*, Phys. Rev. A **79**, 041801(R) (2009).

[152] W. H. Peeters, J. J. D. Moerman, and M. P. van Exter, *Observation of Two-Photon Speckle Patterns*, Phys. Rev. Lett. **104**, 173601 (2010).

[153] L. Marrucci, C. Manzo, and D. Paparo, *Optical Spin-to-Orbital Angular Momentum Conversion in Inhomogeneous Anisotropic Media*, Phys. Rev. Lett. **96**, 163905 (2006).

[154] E. Nagali, F. Sciarrino, F. De Martini, B. Piccirillo, E. Karimi, L. Marrucci, and E. Santamato, *Polarization control of single photon quantum orbital angular momentum states*, Opt. Express **17**, 18745 (2009).

[155] Y. H. Shih and A. V. Sergienko, *Observation of quantum beating in a simple beam-splitting experiment: Two-particle entanglement in spin and space-time*, Phys. Rev. A **50**, 2564 (1994).

[156] P. G. Kwiat, K. Mattle, H. Weinfurter, A. Zeilinger, A. V. Sergienko, and Y. Shih, *Hyper-entangled states*, J. Mod. Opt. **44**, 2173 (1997).

[157] J. T. Barreiro, N. K. Langford, N. A. Peters, and P. G. Kwiat, *Generation of Hyperentangled Photon Pairs*, Phys. Rev. Lett. **95**, 260501 (2005).

[158] C. M. Aegerter, M. Störzer, S. Fiebig, W. Bührer, and G. Maret, *Observation of Anderson localization of light in three dimensions*, J. Opt. Soc. A **24**, A23 (2007).

List of publications

- **W. H. Peeters**, J. J. D. Moerman, and M. P. van Exter, *Observation of Two-Photon Speckle Patterns*, Physical Review Letters **104**, 173601 (2010).

- **W. H. Peeters**, J. J. Renema, and M. P. van Exter, *Engineering of two-photon spatial quantum correlations behind a double slit*, Physical Review A **79**, 043817 (2009).

  (Selected for the Virtual Journal of Quantum Information, May 2009)

- **W. H. Peeters** and M. P. van Exter, *Optical characterization of periodically poled $KTiOPO_4$*, Optics Express **16**, 7344 (2008).

- **W. H. Peeters**, I. M. Vellekoop, A. P. Mosk, and A. Lagendijk, *Wavelength dependence of light diffusion in strongly scattering macroporous gallium phosphide*, Physical Review A **77**, 035803 (2008).

  (Selected for the Virtual Journal of Ultrafast Science, April 2008)

- **W. H. Peeters**, E. J. K. Verstegen, and M. P. van Exter, *Orbital angular momentum analysis of high-dimensional entanglement*, Physical Review A **76**, 042302 (2007).

  (Selected for the Virtual Journal of Quantum Information, October 2007)

Nederlandse samenvatting

Interferentie van fotonparen

Ruimtelijke aspecten van verstrengeling, diffractie en verstrooiing

Het doel van het onderzoek in dit proefschrift is het beter begrijpen van de ruimtelijke aspecten van kwantuminterferentie binnen een paar van verstrengelde fotonen. Deze vorm van interferentie wordt in het vervolg van deze samenvatting tweefotoninterferentie genoemd. Het werk in dit proefschrift is gericht op de resultaten van natuurkundige experimenten. De beschreven theoretische modellen vormen echter een belangrijk onderdeel omdat zij essentieel zijn voor een fundamenteel begrip van de experimentele resultaten.

Kwantumoptica en tweefotoninterferentie

In de klassieke optica wordt licht beschreven als een elektromagnetische golf. Deze beschrijving verklaart alledaagse eigenschappen van licht: kleur, richting, polarisatie, snelheid, diffractie en interferentie. Hoe de toestand van het elektromagnetische veld propageert wordt beschreven door natuurwetten in een klassiekmechanische vorm. In de hedendaagse natuurkunde kent een mechanische beschrijving van de natuur naast de klassieke vorm ook nog de kwantummechanische vorm. Wanneer men het elektromagnetische veld op een kwantummechanische manier gaat beschrijven betreedt men het domein van de kwantumoptica. Het verschijnsel tweefotoninterferentie behoort uitsluitend tot de kwantumoptica.

De kwantummechanische beschrijving van het elektromagnetische veld maakt gebruik van een reeks onderscheidbare toestanden waaruit de elektromagnetische golf is opgebouwd. Deze basistoestanden worden gekarakteriseerd door hun fotonaantal. De kwantummechanische toestand van licht bestaat dus uit een stukje grondtoestand (nul fotonen), een stukje eenfotontoestand (één foton), een stukje tweefotontoestand (twee fotonen), enzovoorts. De verhoudingen tussen deze basistoestanden alsmede de ruimtelijke structuur (golfprofiel) per basistoestand zijn de vrije parameters die de kwantumtoestand en al zijn meetbare eigenschappen vastleggen.

Vanuit experimenteel oogpunt is het foton de kleinste hoeveelheid licht die een lichtdetector kan absorberen. Wanneer men dus meerdere detectoren gelijkmatig zou beschijnen met licht dat enkel uit de eenfotontoestand bestaat kan slechts één detector een respons geven. Welke detector dit is kan niet voorspeld worden. De kans waarmee iedere detector een respons geeft kan echter wél voorspeld worden en wordt gegeven door het golfprofiel van het foton. Het feit dat het slechts voor één detector is toegestaan om een respons te geven kan niet worden verklaard vanuit de klassieke optica.

Het hoofdonderwerp in dit proefschrift, tweefotoninterferentie, vindt plaats in de tweefotonbasistoestand. De ruimtelijke structuur van de tweefotonbasistoestand laat zich beschrijven door een golf als functie van twee coördinaten. Deze tweefotongolf moet geïnterpreteerd worden als de complexe kansamplitude die correspondeert met de kansverdeling waar men de twee fotonen tegelijk kan detecteren met twee detectoren. Het interessante geval is wanneer de twee fotonen ruimtelijk verstrengeld zijn. In dat geval beïnvloedt de plaats waar één van de fotonen geabsorbeerd is instantaan de kansverdeling van de plaats waar men het tweede foton kan detecteren. Hoe de ruimtelijke structuur van deze kwantumcorrelatie eruitziet na propagatie, wordt bepaald door hoe de onderliggende complexe tweefotongolf propageert. Tweefotoninterferentie speelt hierbij een belangrijke rol.

Verstrengelde fotonparen in het laboratorium

Tweefotoninterferentie in verstrengelde fotonparen werd voor het eerst waargenomen in 1987 door Ghosh, Hong, Ou en Mandel [S1]. Zij maakten de verstrengelde paren van fotonen in een niet-lineair optisch proces genaamd spontane parametrische omlaagconversie (SPDC). In dit tweedeorde proces vervalt een hoog energetisch foton spontaan in twee fotonen met een ieder een lagere energie. De zijwaartse plaats en richting van ieder foton kan niet voorspeld worden. Men zegt dan dat ieder foton op zichzelf gezien incoherent is. Echter, het fotonpaar als geheel is wel coherent omdat de fotonen op dezelfde plaats gemaakt zijn en propageren met een tegengestelde zijwaartse impuls. Wanneer men het golfprofiel van één van de fotonen zou meten wordt het golfprofiel van het andere foton instantaan vastgelegd.

Wanneer deeltjes met een golfkarakter gecorreleerd zijn spreekt men van verstrengeling. Verstrengeling komt alleen in kwantummechanische systemen voor omdat daar ieder object ook een golfkarakter heeft. Het niet-lokale karakter van verstrengeling heeft mensen altijd gefascineerd. Hoe kan het zijn dat een meting aan één van de deeltjes instantaan het golfprofiel van het andere deeltje vastlegt? Over deze vraag is al veel geschreven sinds Einstein, Podolsky en Rosen deze curiositeit aan het licht brachten middels hun EPR-paradox [S2]. Later toonde John Bell op wiskundige gronden aan dat het onmogelijk is om de voorspellingen van de kwantummechanica na te bootsen met een theorie die verstrengelde systemen als volledig onafhankelijk beschouwt [S3]. Verstrengeling is niet enkel een natuurkundige curiositeit; verstrengeling speelt ook een centrale rol in de kwantuminformatiekunde waarin men revolutionaire toepassingen in de informatietechnologie beoogt [S4].

Laten we terugkeren naar de SPDC-lichtbron van verstrengelde fotonen. Hoe de kwantumcorrelaties eruitzien op een willekeurige afstand van de lichtbron hangt af van hoe de tweefotongolf als geheel propageert. Hierbij spelen diffractie en interferentie een belangrijke rol. Sinds de eerste waarneming van tweefotoninterferentie in 1987 is er wereldwijd veel onderzoek gedaan naar deze fenomenen. Er zijn echter veel optische systemen waarvoor het nog onduidelijk is hoe zij de ruimtelijke kwantumcorrelaties beïnvloeden. Verder kan ons inzicht in verschillende aspecten van ruimtelijke verstrengeling scherper en algemener gemaakt worden.

Het onderzoek in dit proefschrift

In dit proefschrift wordt op zowel experimentele als theoretische wijze bestudeerd hoe de ruimtelijke kwantumcorrelatie tussen de verstrengelde fotonen eruitziet na propagatie door verschillende optische systemen. Het onderzoek kan worden onderverdeeld in drie onderzoeksthema's.

Verstrengeling van de baanimpuls

De ruimtelijke verstrengeling tussen de fotonen betekent dat een meting van het golfprofiel van één van de fotonen instantaan het golfprofiel van het andere foton vastlegt. De set van golfprofielen waarop men het eerste foton projecteert wordt de meetbasis genoemd. Een van de best bestudeerde meetbases is die van de baanimpuls. Als het eerste foton gedetecteerd wordt met baanimpuls $+l\hbar$, dan kan het tweede foton enkel gedetecteerd worden met baanimpuls $-l\hbar$. Dit gebeurt zo omdat het hoogenergetische moederfoton een baanimpuls gelijk aan nul heeft en omdat de totale baanimpuls behouden dient te zijn in het conversieproces.

De kansverdeling van de baanimpuls per foton kan in principe gemeten worden door slechts één van de fotonen te observeren. Zo'n experiment geeft echter geen uitsluitsel over of de fotonen daadwerkelijk verstrengeld zijn. Het kan net zo goed zijn dat ieder foton volledig onafhankelijk is. In de wetenschappelijke literatuur werd er beargumenteerd dat de baanimpulsverdeling ook gemeten zou kunnen worden door middel van een tweefotoninterferentie-effect [S5]. De experimentele techniek hiervoor maakt gebruik van een tweefotoninterferometer (van het Hong-Ou-Mandel-type) met een beelddraaier in één van de armen en een oneven aantal spiegels in beide armen samen. De kansverdeling van de baanimpuls kan men nu afleiden uit het contrast (of de zichtbaarheid) van het Hong-Ou-Mandel-dal als functie van de hoeveelheid beeldverdraaiing.

In dit proefschrift wordt deze uitdagende techniek gebruikt om de kansverdeling van de baanimpulsverstrengeling te bepalen. Verder worden er enkele speciale gevallen behandeld en wordt er een gedetailleerde theoretische onderbouwing gegeven. Dit werk is gepubliceerd in Ref. [S6] en wordt beschreven in Hoofdstuk 2 van dit proefschrift.

Tweefotoninterferentie achter een apertuur met twee spleten

In de historie van de natuurkunde speelt het apertuur met twee spleten een zeer belangrijke rol. Dit apertuur, ook wel een dubbelspleet genoemd, werd rond 1801 gebruikt door de Britse fysicus Thomas Young om te demonstreren dat licht zich gedraagt als een golf. Wanneer men een dubbelspleet belicht met monochromatisch coherent licht zal men ver achter het apertuur een lijnenpatroon waarnemen in plaats van de schaduwen van de twee spleten. Dit lijnenpatroon kan men verklaren als een interferentiepatroon dat men verwacht voor een golf.

Het ligt dus voor de hand om ook tweefotoninterferentie te bestuderen achter een dubbelspleet. Het fotonpaar als geheel gedraagt zich immers ook als een soort golf, namelijk als een golf als functie van twee coördinaten. Er zijn dan ook vele publicaties te vinden die tweefotoninterferentie achter een dubbelspleet bestuderen. Maar ondanks al dit onderzoek is de rijke verscheidenheid aan mogelijke tweefotoninterferentiepatronen nog onvoldoende bestudeerd. Het merendeel van de tweefotoninterferentiepatronen achter een dubbelspleet is nog nooit gemaakt en gemeten. Verder is er weinig inzicht in hoe men alle mogelijke vormen van tweefotoninterferentiepatronen op een gecontroleerde manier kan verwezenlijken.

In dit proefschrift wordt een samenhangende en inzichtelijke beschrijving gegeven van hoe de grote verscheidenheid aan mogelijke tweefotoninterferentiepatronen achter een dubbelspleet gemaakt kan worden. Hiermee heeft het werk een grote unificerende waarde in de wetenschappelijke literatuur. Uiteraard worden deze technieken experimenteel gedemonstreerd. De experimentele data zijn van ongeëvenaarde kwaliteit en zijn zeer illustratief voor de rijke diversiteit die het fenomeen tweefotoninterferentie in zich heeft. Dit werk is gepubliceerd in Ref. [S7] en wordt beschreven in Hoofdstuk 4 van dit proefschrift.

Verder wordt er in dit proefschrift betoogd dat de fase van het tweefotongolfprofiel uitermate belangrijk is voor het type kwantumcorrelaties en het tweefotoninterferentiepatroon. De fasekromming van het tweefotongolffront werd in het verleden meestal genegeerd. Om volledige controle te hebben over het te maken tweefotoninterferentiepatroon is een goed begrip van de faseaansluiting in het niet-lineaire kristal van belang. Een gedetailleerde analyse van de faseaansluiting wordt behandeld in Hoofdstuk 3 van dit proefschrift en is gepubliceerd in Ref. [S8].

Verstrooiing van fotonparen aan wanordelijke materialen

Dit thema is het meest vooruitstrevend. De propagatie van verstrengelde fotonparen door wanordelijke materialen was nog niet experimenteel onderzocht. Zeer recentelijk zijn er enkele theoretische artikelen verschenen over dit onderwerp [S9]. Waarom is dit een interessant onderwerp? De reden is dat klassieke interferentie-effecten in wanordelijke materialen ten grondslag liggen aan enkele zeer interessante fenomenen zoals optische spikkel, bovenmatige terugverstrooiing en Anderson lokalisatie. Nu doet zich de vraag voor of er ook interessante tweefotoninterferentie-effecten kunnen worden ontdekt in wanordelijke materialen.

In Hoodstuk 5 van dit proefschrift wordt de eerste waarneming van tweefotonspikkel beschreven [S10]. Deze spikkelpatronen zijn ontstaan ten gevolge van verstrooiing van ruimtelijk verstrengelde fotonparen aan wanordelijke structuren. Het werk wordt ondersteund door een theoretische beschrijving van de ruimtelijke structuur in de kwantumcorrelaties in het verstrooide fotonpaar. De metingen laten zien dat tweefotonspikkel van een volumineuze verstrooier en een platte verstrooier volledig verschillend zijn. Dit is verrassend omdat klassieke spikkel er hetzelfde uitziet voor deze verstrooiers.

Ten slotte beschrijft dit proefschrift het eerste experiment waarin een tweefotoninterferentie-effect een middeling over meerdere realisaties van het wanordelijke medium overleeft. Dit wordt gerealiseerd door de fotonen onderscheidbaar te maken door de fotonen een verschillende polarisatie te geven. Het blijkt dat de fotonen de neiging hebben samen te klonteren of elkaar juist te ontwijken waarbij dit gedrag afhangt van de ruimtelijke symmetrie tussen de fotonen. Deze symmetrieën zijn volledig analoog met symmetrieën die we kennen in echte bosonische, fermionische en anyonische kwantumvelden.

[S1] R. Ghosh and L. Mandel, Phys. Rev. Lett. **59**, 1903 (1987).
C. K. Hong, Z. Y. Ou, and L. Mandel, Phys. Rev. Lett. **59**, 2044 (1987).

[S2] A. Einstein, B. Podolsky, and N. Rosen, Phys. Rev. **47**, 777 (1935).

[S3] J. S. Bell, Physics (NY) **1**, 195 (1964).
J. S. Bell, Rev. Mod. Phys. **38**, 447 (1966).

[S4] Nielsen and Chuang, *Quantum Computation and Quantum Information*, Cambridge University Press (2000).

[S5] M. P. van Exter *et al.*, Opt. Expr. **15**, 6431 (2007).

[S6] W. H. Peeters *et al.*, Phys. Rev. A **76**, 042302 (2007).

[S7] W. H. Peeters *et al.*, Phys. Rev. A **79**, 043817 (2009).

[S8] W. H. Peeters and M. P. van Exter, Opt. Expr. **16**, 7344 (2008).

[S9] C. W. J. Beenakker *et al.*, Phys. Rev. Lett. **102**, 193601 (2009).
J. R. Ott *et al.*, Phys. Rev. Lett. **105**, 090501 (2010).
Y. Lahini *et al.*, Phys. Rev. Lett. **105**, 163905 (2010).

[S10] W. H. Peeters *et al.*, Phys. Rev. Lett. **104**, 173601 (2010).

Nawoord

De afgelopen viereneenhalf jaar heb ik met veel mensen samengewerkt. Zonder deze samenwerking was dit proefschrift er waarschijnlijk niet geweest. Daarom wil ik hier enkele mensen bedanken.

In het bijzonder wil ik mijn dagelijkse begeleider Martin van Exter bedanken. Je gepassioneerde betrokkenheid bij het bedenken van experimenten en het begrijpen van de meetdata heeft sterk bijgedragen aan de inhoud van dit proefschrift. Mijn promotor Han Woerdman, ik dank je voor je goede inhoudelijke adviezen evenals het zorgvuldig volgen en bespreken van het verloop van mijn promotietraject.

De experimenten in dit proefschrift waren niet mogelijk geweest zonder de altijd parate ondersteuning van de Elektronische Dienst en de Fijn Mechanische Dienst. Ik dank Arno van Amersfoort, René Overgauw, Koos Benning, Gijsbert Verdoes, Christiaan Pen, Harmen van der Meer, Fred Schenkel en Ewie de Kuyper voor de technische ondersteuning en de plezierige samenwerking. Ik dank Gert 't Hooft, Emile Verstegen en Paul Junger voor de ondersteuning vanuit Philips en de LIS.

Ik dank studenten Steven Verstoep, Jelmer Renema, Abderrahim Hadda, Hans Moerman en Thierry Kauffmann voor hun inzet en de leerzame samenwerking. Jelmer en Hans, jullie grote verantwoordelijkheid en creativiteit gaven mij extra energie. Dank ook voor jullie inbreng in hoofdstukken 4 en 5.

Specifically for chapter 2, I would like to thank Paul Ruijgrok and Steven Verstoep for assistance with the experiment. Thanks to Alex Skliar for providing information about the nonlinear crystals in chapter 3. I thank Dirk Bouwmeester and Eduard Driessen for stimulating discussions about the two-photon double slit in chapter 4. Thanks to Thierry Kauffmann and Henrique Di Lorenzo Pires for useful discussions regarding chapter 5. Also many thanks to Joav Lahini, Rami Pugatch, Robin Kaiser, and Johan Ott, your questions and remarks regarding the two-photon speckle experiments have been very beneficial for the readability of chapter 5. For chapter 6, I thank Gerard Nienhuis for valuable discussions and Richard Gill and Stefan Zohren for pointing out references on invariant unitary integrals.

Tijdens het laatste jaar van mijn promotietraject ondervond ik nogal wat hinder van rug- en armpijn. Ik ben zeer dankbaar voor de doeltreffende hulp die ik heb ontvangen van Mieke Mus en Uta Koch. Verder ben ik Joost Weber en Anneke Edelenbosch dankbaar voor het advies vanuit de personeelsdiensten. En Thijs Klaassen, bedankt voor onze gesprekken.

Het doen van wetenschap is een creatief proces waarin discussie, inspiratie, noeste arbeid, bezinning en bezinking allemaal belangrijk zijn. Zowel binnen als buiten kantooruren heb ik vele mensen hiermee belast en vele mensen hebben mij gesteund. Collega's in de kwantumopticagroep, vrienden en familie, allemaal bedankt voor de interesse en de steun! Hieronder wil ik in dit verband enkele mensen op persoonlijke wijze noemen.

Mijn vrolijke Braziliaanse kamergenoot Henrique, bedankt voor jouw lessen dont-bother-be-happy. Bart-Jan, bedankt voor de yogatip! Steven en Gerard, mijn persoonlijke consultants theoretische natuurkunde, dank voor de interessante discussies en jullie geduld. Bedankt Frerik, jij blies nieuw leven in onze groepsvergaderingen. Ljubiša en Joris, het was goed om jullie als collega's te hebben. Bedankt Eric voor de ondersteuning. Michiel en Wolfgang, bedankt voor de grote stimulerende wetenschappelijke interesse. Philip, bedankt voor je taalkundige tips. Mensen van de Really Big Band, ik heb heel erg genoten van onze repetities en optredens. Martijn, puike omslag! Vrienden tijdens de vele gezellige thuisdinertjes en spellenavonden, bedankt voor jullie hardnekkige interesse in fotonen. Obbe en Ralph, ik ben blij dat jullie mijn paranimfen zijn. Mijn familie en schoonfamilie, jullie grote interesse en steun in mijn promotietijd heeft veel voor mij betekend. Veel dank daarvoor. Mijn ouders, Ton en Wilma, jullie hebben mij altijd gestimuleerd mijn eigen interesses te volgen. Dat is een heel belangrijk ingrediënt van dit boekje. En Janneke, mijn lieve vriendin, bedankt voor al je zorg en liefde in deze soms veelvragende tijd!

Leiden, 8 november 2010

Curriculum vitae

Wouter Herman Peeters

1980	Born in Berg en Terblijt, The Netherlands.
1992-1998	Secondary school, Stella Maris College, Meerssen.
1998-2006	M.Sc. Applied Physics (*cum laude*), University of Twente. Graduation at the Complex Photonic Systems group. Advisors: dr. ir. I. M. Vellekoop, dr. A. P. Mosk, and prof. dr. A. Lagendijk.
2006-2010	Ph.D. research at Leiden University. Employed by the Dutch Foundation for Fundamental Research on Matter (FOM). The research is carried out at the Quantum Optics and Quantum Information group under the supervision of dr. M. P. van Exter and prof. dr. J. P. Woerdman.